Politecnico di Milano
Department of Electronics, Information and Bioengineering
Doctoral Program in Bioengineering

A combined experimental and numerical approach towards a comprehensive drug delivery model

Doctoral Dissertation of:
Marco Vidotto
10376927

Supervisors:
Prof. Elena De Momi, Prof. Daniele Dini
Tutor:
Prof. Chiara Guazzoni
The Chair of the Doctoral Program:
Prof. Andrea Aliverti

2020 - XXXII Cycle

"There, peeping among the cloud-wrack above a dark tor high up in the mountains, Sam saw a white star twinkle for a while. The beauty of it smote his heart, as he looked up out of the forsaken land, and hope returned to him. For like a shaft, clear and cold, the thought pierced him that in the end the Shadow was only a small and passing thing: there was light and high beauty for ever beyond its reach."

[J.R.R. Tolkien - *The Return of the King*]

Politecnico di Milano
Department of Electronics, Information and Bioengineering
Doctoral Program in Bioengineering

Abstract

A combined experimental and numerical approach towards a comprehensive drug delivery model

by Marco VIDOTTO

Convection-Enhanced Delivery (CED) has been recently introduced as a promising surgical technique to bypass the blood-brain barrier and inject a chemotherapeutic agent directly in the brain tissue. CED can be used for treating different kind of diseases, from brain tumor to Parkinson and epilepsy. Although this technique was expected to be effective, especially against recurrent tumors, the clinical trials did not achieve the desired results in terms of life expectancy for the patients. A major impairment to progress is given by the fact that the cancerous areas are usually not reached by a sufficiently high concentration of drug. Indeed, since the brain is an anisotropic and heterogeneous porous medium, for the clinicians it is very difficult to set the infusion in the best way possible and often the drug misses the target area.

To tackle this issue, researchers have worked on predictive numerical models that can offer the surgeons a simulation environment to test different infusion settings. Despite these models are extremely valuable, their predictive capability is still not sufficiently accurate thus preventing their use in standard clinical practice. For this reason, many researchers pointed out the paramount importance of having refined mathematical models on the spatial drug distribution within the brain and underlined the pivotal role of the brain microstructure. This aspect, in particular, has been explored by limited researches and the relation between tissue microstructure and important fluid dynamics parameters is still controversial.

In the present contribution, we develop an extensive study that starts from a detailed analysis of the brain microstructure, with particular emphasis on

the white matter (WM) permeability, and finishes with the integration of the acquired information in a CED predictive model at the macroscale. In addition to the Introduction Chapter and the Conclusion Chapter, the dissertation is divided in four main research tracks.

In the first (Chapter 2), we build a geometrical model of the WM considering its main geometrical characteristics, namely axon diameter distribution, extracellular space (ECS) volume fraction and ECS width. From this model, we extract two important information: the hydraulic permeability in three WM areas and the size of the representative volume element (RVE) to analyse to obtain reliable results. A three-dimensional version of the same geometrical model is also exploited, with a different methodological approach, to study the WM tortuosity, a very important parameter for drug diffusion.

In the second (Chapter 3), we move towards a more realistic estimate of the permeability by analysing two WM areas (corpus callosum and fornix) starting from the acquisition of electron microscopy images of their microstructure. In this track, we demonstrate and quantified the anisotropic and heterogeneous behaviour of the WM which is a very important results because it helps shading light on this fundamental but still controversial parameter.

These results are validated in the third track (Chapter 4) by means of an experimental campaign on ovine WM samples performed in collaboration with Imperial College London.

Finally, in the last track (Chapter 5), we integrate the information about the WM permeability, acquired in the previous Chapters with a relatively new imaging technique, namely the Neurite Orientation Dispersion and Density Imaging, to incorporate a more advanced and comprehensive description of the brain microstructure into a predictive computational model. We demonstrate the relevance of the work by showing the impact on the predicted drug distribution, which differs significantly from the state-of-the-art model in terms of distribution shape, concentration profile and infusion linear penetration length.

Contents

List of Figures

List of Tables

To Petra, the love of my life,

Chapter 1

Introduction

1.1 Clinical problem (brain tumor)

Despite the importance of the brain for patient life expectancy and life quality, it is still our least understood organ (Medical Research Council, 2009). This is due to its impressive complexity, not only in terms of physiological and pathological mechanisms but also from a structural and anatomical point of view (Lei et al., 2015). Moreover, according to the European Brain Council (EBC), brain-related diseases affect 179 millions of Europeans. Indeed, we have assisted to the increase of diseases typical of an elderly population such as nervous disorders, tumours and strokes (Olesen et al., 2012). This is due to the ageing of population whose life expectancy has sharply increased in the last 70 years (World Population Prospects 2019).

Dealing with brain disorders is not only a clinical problem but it also has a considerable bearing on the economic sustainability. In 2012, Olesen et al., 2012, estimated the cost of brain disorders in Europe relative to the 2010; according to their report, the total amount is around €798 billion with an average cost per inhabitant equal to €5,550. Finally, the authors concluded that an increased focus on research strategies, prevention and care is necessary to reduce the future cost of brain disorders.

In this dissertation, we focus our attention on a very important disease, the brain tumour, which affects 14.8 per 100,000 person/years with a cost in Europe around €5.2 billion (Buckner et al., 2007; Olesen et al., 2012). In particular, gliomas account for 78% of malignant tumors (Buckner et al., 2007). Within this group, the most common and most malignant brain tumors is Glioblastoma Multiforme (GBM) (Ohgaki and Kleihues, 2013). GBM shows regions of necrosis in the central region and increased vascularity on the borders that can be identified by T1-weighted MRI scans (Fig. 1.1) as well as in fixed tissue (Fig. 1.2) (Buckner et al., 2007). Its incidence rate per 100,000 person/year was reported by Ohgaki et al. (Ohgaki et al., 2004) to be around 3.3 in males and 2.3 in females, between 1980 and 1994. However, a more recent study by Philips et al. (Philips et al., 2018) has shown that the incidence rate has more than doubled its value in only 20 years (Fig. 1.3). Moreover, despite the treatments cost billions, the median overall survival for GBM is limited to 14.6 months with only a 6.9 months interval in which there is no progression of the tumour (Mehta et al., 2015; Thakkar et al., 2014).

1.2 GBM treatments and limitations

1.2.1 GBM conventional treatments

The current standard of care for newly-diagnosed GBM is maximum safe cytoreductive surgery followed by concurrent temozolomide (TMZ) and fractional external beam radiotherapy (Davis, 2016; Mehta et al., 2015). Moreover, in the last years, the use of functional MRI and Diffusion Tensor Imaging (DTI) in preoperative planning, as well as ultrasound and MRI with direct stimulation during surgery, has allowed for multimodal neuronavigation and the integration of patient-specific anatomical data (Davis, 2016).

Despite the introduction of these technologies, the survival rate is still very poor because differentiating between normal brain and residual tumor continues to be a major challenge (Davis, 2016). This is due to the highly invasive character of GBM cells that tends to infiltrate in the tumor surrounding areas. Since GBM often occurs in important part of the brain e.g. control speech, motor function and senses, a radical resection of the primary tumor mass is not curative because some cells always remain (Williams et al., 2014). Moreover, even if treated with postoperative radiation therapy with concomitant TMZ chemotherapy, around 70% of the patients still experience disease recurrence

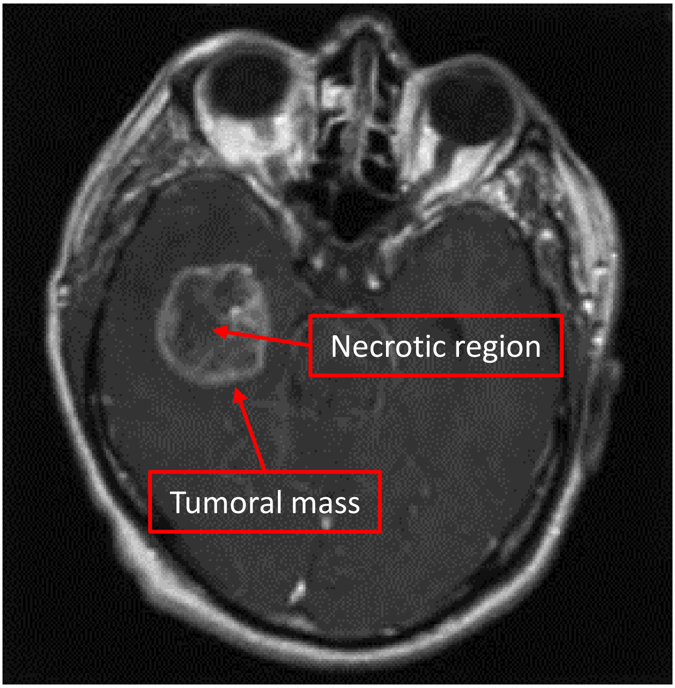

FIGURE 1.1: Gadolinium-enhanced T1-weighted magnetic resonance image showing the typical appearance of GBM. Adapted from (Buckner et al., 2007).

or progression in the following year (Stupp et al., 2009) with less than 5% of them surviving five years after diagnosis (Ostrom et al., 2014).

Obviously, there are a number of factors which influence the clinical outcomes for patient affected by GBM and, for this reason, researchers are still looking for novel approaches (Jahangiri et al., 2016). Nevertheless, a key issue for chemotherapy efficacy, which has been highlighted by many researchers (Bobo et al., 1994; Crawford, Rosch, and Putnam, 2016; Jahangiri et al., 2016; Davis, 2016), is represented by the blood-brain barrier (BBB). The latter is a natural protective barrier which prevents the entrance of toxic molecules and agents into the central nervous system (CNS). The flux of polar molecules and big compounds (molecular weight higher than 400 Da) from the blood

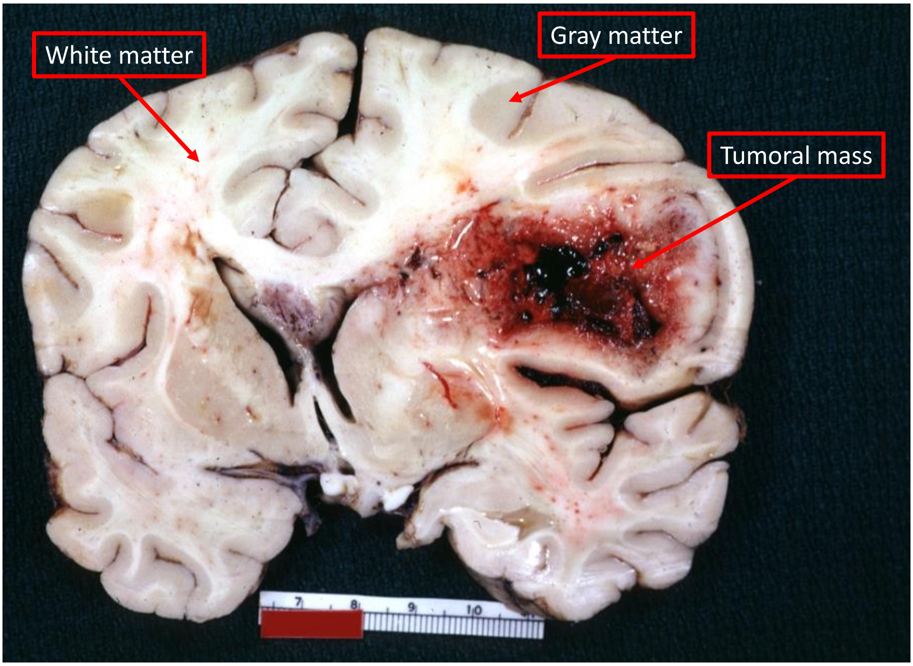

FIGURE 1.2: Slice of a fixed brain affected by glioblastoma multiforme (GBM). It is easy to notice the necrotic part in the center of the tumor mass and the hemorrhage at the borders. Adapted from: Pathology Education Informational Resource (PEIR) Digital Library (http://peir.path.uab.edu/ library/).

to the CNS is strictly restricted by tight junction between the capillary endothelial cells. Moreover, even if lipophilic molecules may pass through the BBB through diffusion mechanism, there are special proteins on the endothelial cells that transport them back into the blood stream (Crawford, Rosch, and Putnam, 2016; Ballabh, Braun, and Nedergaard, 2004). For the reasons explained above, it is evident the need for drug delivery systems capable of beating the formidable challenge represented by the BBB.

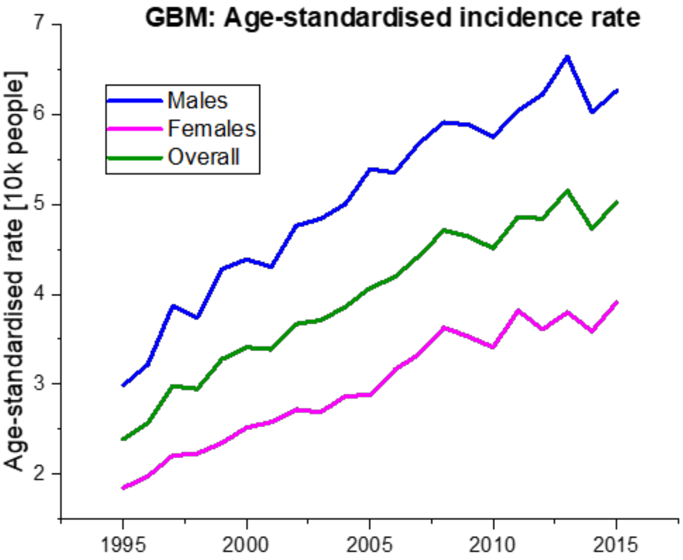

FIGURE 1.3: Glioblastoma multiforme age-standardized incidence rate based on sex; dark blue, violet and green curves represent male, female and overall values, respectively. Figure adapted from data present in (Philips et al., 2018).

1.2.2 GBM innovative treatments

Since the BBB is the main obstacle to conventional chemotherapy, a way to overcome the problem could be to manipulate or bypass the BBB. Several approaches have been investigated in the literature:

- Temporary disruption of tight junctions in the BBB via osmotic mechanism: this method relies on the administration of an hypertonic solution that causes a shrinkage of the endothelial cells thus leading to the physical disruption of the tight junctions. In this way, BBB permeability increase 10 times and even big molecular compounds would be able to pass through the BBB (KrolI, Neuwelt, and Neuwelt, 1998; Rapoport, 2001). However, the usability of this procedure has been limited due to toxicity risks and complexity of the method.

- Trans-cranial delivery of low frequency ultrasound waves: this is another disruptive method where the ultrasound waves are used to create openings between endothelial cells. Preclinical studies suggest that this technique can safely facilitate the focal delivery of drugs in the brain. However, more studies are needed to move this technique to clinical practice (Todd et al., 2019; Hynynen et al., 2006; Etame et al., 2012).

- Intranasal administration: it is a relatively new approach that allows circumventing the BBB by providing a direct route to the brain. Indeed, after the administration, the drugs are absorbed through the nasal mucosa and can enter the brain through either the olfactory or trigeminal pathways. This approach promotes a very high drug accumulation within the first few hours that can be useful for some pathologies (Meredith, Salameh, and Banks, 2015; Crawford, Rosch, and Putnam, 2016).

- Chemotherapeutic wafers: after surgery, wafers containing the chemotherapeutic agent are implanted in the region surrounding the tumor resection cavity with the goal of destroying local remaining tumor cells. Indeed, the drug is released from the degrading wafers and diffuses in the brain due to the concentration gradient (Crawford, Rosch, and Putnam, 2016). Despite this approach has shown clinically useful results (Westphal et al., 2006), there are still some limitations. In particular, to eliminate the tumoral cells, a high concentration of drug is required but the concentration tends to be very high in proximity of the wafers and to steeply decrease as the distance from the wafer increases (Weiser and Saltzman, 2014; Crawford, Rosch, and Putnam, 2016).

- Convection-Enhanced Delivery (CED): this technique was introduced by Bobo et al., 1994 to deal with the problem of poor drug penetration. The main idea was to use convection to augment the local concentration of drug molecules by infusing directly in the brain tissue (Crawford, Rosch, and Putnam, 2016). Since CED is one of the most promising technique, this dissertation will focus on this approach that will be treated in full in the next section.

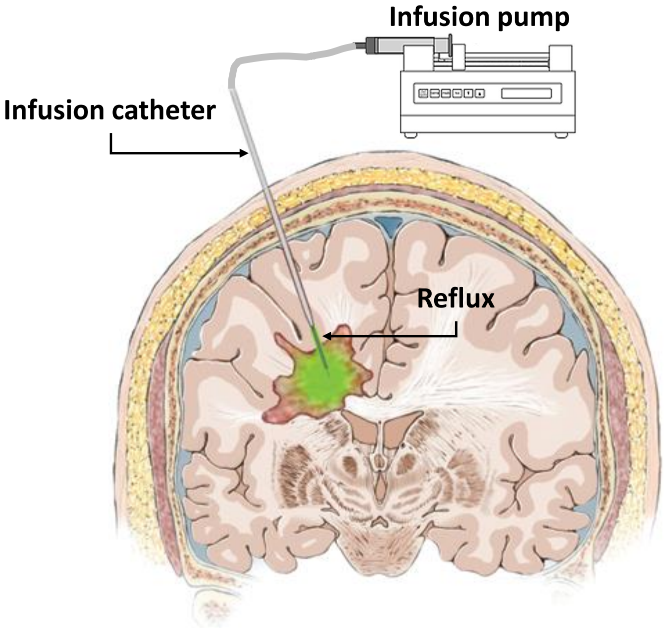

FIGURE 1.4: Artist's illustrations showing the improvement in distribution with CED relative to diffusion occurring with non-convected injection. The figure shows the theoretical distribution with minimal associated reflux (green in cannula) with CED. Adapted from (Jahangiri et al., 2016).

1.3 Convection-Enhanced Delivery (CED)

As stated above, Bobo et al., 1994 introduced CED, an innovative procedure where the infusion is driven by an applied positive pressure thanks to a pump that drives the flow into the tissue through one or more catheters thus circumventing the BBB (Fig. 1.4). The catheters are positioned through direct stereotactic intracerebral placement and attached to a pump that can provide a constant microfluidic flow rate which is usually in the order of $\mu l/min$ for hours to days (Jahangiri et al., 2016; Barua et al., 2013; Barua et al., 2014). Such a small flow rate is necessary to avoid a phenomenon called backflow or reflux. When backflow occurs, the chemotherapeutic solution flows in the interstitial space between the brain and the catheter that leads out of the brain instead of into the parenchyma (Mehta et al., 2015).

As stated by Crawford, Rosch, and Putnam, 2016, CED may not be suitable for diseases that affect a considerable part of the brain because there are limits to the volume of distribution of the infused material. On the other hand, more localized diseases, in which the target area is contained in a certain region, are more convenient for the use of CED (Crawford, Rosch, and Putnam, 2016; Vogelbaum and Aghi, 2015; Lam, Thomas, and Lind, 2011). Indeed, if CED is applied after resection of a brain tumor, the microinfusion catheters aim at the peritumoral region thus enhancing the distribution of small or large therapeutic compounds in the brain (Mehta et al., 2015). It is important to underline that, with CED it is possible to obtain an almost constant concentration of drug spanning a predictable distance from the infusion site before the drop-off (Ding et al., 2010; Mehta et al., 2015).

Concluding, CED offers several advantages with respect to other mechanisms that rely only on diffusion such as chemotherapeutic wafers (Jahangiri et al., 2016). First, with CED, it is possible to achieve a much higher intratumoral spatial distribution because the pressure gradient allows drugs to be infused over a larger volume. Moreover, the distribution is more even and with higher concentration (Raghavan et al., 2006; Syková and Nicholson, 2008; Vargová et al., 2003). Second, since CED overcomes the problem of having a steep concentration gradient associated with diffusion-mediated delivery, it is possible to use less strong dose of chemotherapeutic agent (Kroll et al., 1996). Third, the drug transport is mainly due to bulk flow thus favouring the distribution also of agents with a high molecular weight (Jahangiri et al., 2016).

Although CED has shown promising results in the field of neurological drug delivery, clinical trials have not succeeded in demonstrating its benefit in terms of life expectancy for the patients (Jahangiri et al., 2016; Kunwar et al., 2010; Crawford, Rosch, and Putnam, 2016). This is due to the fact that several challenges still need to be faced as reported by brilliant reviews (Jahangiri et al., 2016; Crawford, Rosch, and Putnam, 2016; Debinski and Tatter, 2009):

- Agent to be delivered: choosing the best agent to be delivered is crucial to determine CED outcomes. Indeed, since it is necessary to target the tumor cells infiltrated between the white matter (WM) cells, the drug must have a wide therapeutic index.

- Catheter design: currently there are many different type of catheters, e.g. with rounded tip, with multiple openings, flexible for longer-term CED etc. Each of them as pros and cons but a gold standard has not been identified yet.

- Catheter placement: retrospective analysis on the PRECISE trial (Kunwar et al., 2010) showed that the catheters were misplaced in more than 50% of the patients thus leading to not optimal results. Therefore, CED would benefit from a more precise and automatic positioning of the catheter thus reducing risks of leakage of drug into the intraventricular spaces or subarachnoid space.

- Intratumoral penetration: since tumors are strongly heterogeneous, it is difficult to reach an homogeneous delivery of therapeutic agent. Computational modelling based on the physical characteristics of the tumor may improve the penetration by allowing accurate and reliable prediction of the chemotherapeutic concentration.

- Protocol: CED overall protocol, from infusion parameters to optimal endpoint is still unclear. Currently, long-term implantable ports are being studied to allow patients to receive multiple rounds of CED.

From this brief overview on CED, two important considerations emerge: CED efficacy depends on the ability to reach enough concentration of drug in the desired region but, unfortunately, drug distribution is influenced by many factors and infusion parameters. Therefore, clinicians would benefit from the use of reliable predictive numerical models that can predict the drug distribution and concentration in the preoperative phase (Crawford, Rosch, and Putnam, 2016; Jahangiri et al., 2016). Indeed, a predictive model allows the surgeon to test different catheter setups and clinical settings in order to decide the best way to proceed with the patient.

Nevertheless, as underlined also by Vendel, Rottschäfer, and Lange, 2019, there is still an important need for refined mathematical models on spatial drug distribution within the brain. In the next session, we present the state of the art about this topic.

1.4 CED predictive numerical models

The brain is one of the most complex organs of the human body, not only from the physiological/pathological functioning point of view but also considering its structural and anatomical organization. The brain is composed of excitable nerve cells, called neurons, and their long processes, known as axons or nerve fibres. It is protected by a system of membranes, called meninges, and suspended in the cerebrospinal fluid (CSF). It is organised into region mainly consisting of nerve cell bodies, the grey matter (GM), and into regions mainly composed of axons, the WM. Moreover, it is crossed by a particular vascular system known as BBB (Peate, 2017).

From a modeling perspective, the cerebral tissue is an heterogeneous and anisotropic porous medium (Vendel, Rottschäfer, and Lange, 2019). The heterogeneity is given by the presence of different phases (cells, CSF and blood) whereas the anisotropy is due to the presence of long parallel myelinated nerve fibres which characterise the WM regions (Ehlers and Wagner, 2015).

In Table 1.1, it is possible to appreciate a brief history of the main contributions to CED modelling that started back in 1994 and are still ongoing. We grouped them in terms of cell phase constitutive model, imaging modality and validation procedure.

1.4.1 Cellular phase constitutive model

During CED, a chemotherapeutic agent is injected directly in the brain tissue and it flows through the interstitial spaces between neural cells where the extracellular space (ECS) volume fraction can vary between 0.15 and 0.4 (Syková and Nicholson, 2008; Duval, Stikov, and Cohen-Adad, 2016). The cells represents the solid part of the brain and choosing the most appropriate constitutive model is not trivial. Indeed, if the solid part is modelled as rigid, the brain constitutive parameters do not change in time. On the other hand, if the cells are subjected to deformation caused by the fluid pressure, the constitutive parameters can change. From Table 1.1, it is clear that both approaches have been followed by researchers in modelling CED.

TABLE 1.1: The main contributions found in the literature concerning CED modeling are listed in chronological order. Moreover, we reported how the authors modelled the cellular phase of the brain (R = Rigid; D = Deformable), the imaging modality and the validation strategy (if present).

Refs	Rigid	Imaging	Validation
Morrison et al., 1994	R	NA	No
McGuire, Zaharoff, and Yuan, 2006	D	NA	Rat tumour
Sarntinoranont et al., 2006	R	DTI	Rat
Chen and Sarntinoranont, 2007	D	NA	Analytical
Sampson et al., 2007	R	DTI	Human
Linninger et al., 2008b	R	DTI	Agarose gel
Linninger et al., 2008a	R	DTI	No
Smith and García, 2009	D	NA	No
Smith and Jaime García, 2010	D	NA	No
Kim, Mareci, and Sarntinoranont, 2010	R	DTI	Rat
Raghavan and Brady, 2011	D	DTI	Pig
Rosenbluth et al., 2011	D	DTI	Primates
Smith, Starkweather, and García, 2011	D	NA	No
Støverud et al., 2011	D	DTI	No
Kim et al., 2012	R	DTI	Rat
Ehlers and Wagner, 2015	D	DTI	No
García, Molano, and Smith, 2013	D	NA	Agarose gel
Lueshen et al., 2014	R	DTI	Rat
Dai et al., 2016	R	DTI	Rat
Zhan et al., 2017	R	DTI	No
Messaritaki et al., 2018	R	NG-DTI	No
Zhan, Alamer, and Xu, 2018	R	DTI	No
Zhan and Wang, 2018	R	DTI	No
Zhan, Baena, and Dini, 2019	R	DTI	No
Vidotto et al., N.D.	R	DTI-NODDI	No

- Rigid: modelling the brain as a not deformable porous media is an approach that has been followed by many authors (Table 1.1). Morrison et al., 1994 developed a simplified theory of the transport of substances in brain tissue associated with direct infusion. The goal was to describe the transport mechanism in the simplest way possible. Indeed, it was based on several simplifying assumptions, between the most important we can find that: the brain was considered an homogeneous porous medium and both the ECS volume fraction and the hydraulic permeability were constant. On the other hand, other hypotheses proved themselves to be very appropriate and were then used by all the subsequent models. For example the fact that the bulk flow driven by the pressure gradient and produced by the pump can be described with Darcy's law (Darcy, 1994) and that the infused molecule is not significantly retarded by the interstitial matrix. Accordingly, subsequent rigid models build on the work explained above trying to tackle its main limitations (homogeneous brain tissue and constant fluid dynamics parameters).

  Sarntinoranont et al., 2006 developed a methodology to process DTI data and segment GM and WM assigning different tissue transport properties. DTI is a diffusion-weighted magnetic resonance imaging method (DW-MRI), that can be used to map and characterise the three dimensional diffusion of water in the brain as a function of spatial location (Alexander et al., 2007). Indeed from DTI, it is possible to derive the fiber tract orientation that were used to assign directional dependence of hydraulic permeability and diffusivity.

  Linninger et al., 2008a added another piece to CED modelling by extracting from the DTI tensor not only the eigenvectors but also the eigenvalues. The latter were used to scale a fixed value of hydraulic permeability and diffusivity along the three principal directions as a function of the DTI eigenvalues. This paradigm was then exploited also in other models with minor changes according to the specific application. On the contrary, other authors (Kim, Mareci, and Sarntinoranont, 2010; Kim et al., 2012; Dai et al., 2016) continued to use fixed values of permeability but introduced an innovative approach where the numerical model was extracted directly from the imaging dataset with a univocal correspondence between image voxels and model elements.

- Deformable: one of the first computational study proposed in the literature with a deformable brain model was developed by McGuire, Zaharoff, and Yuan, 2006. The authors aimed at studying the effect of infusion pressure and infusion induced tissue deformation on infusion rate. They modeled the cerebral tissue as a poro-elastic medium and compared their results with three mouse tumor models. Hydraulic permeability depended on tissue deformation according to a modified version of the Lai and Mow, 1980 equation that took into account tissue anisotropy. However, since the authors had no way to inspect the brain microstructure, their model is based on several debatable assumptions.

  A similar approach in terms of geometrical model, with an extremely simplified spherical symmetry, was implemented by Smith and García, 2009 and Smith and Jaime García, 2010. Their biphasic nonlinear mathematical model aimed at demonstrating the importance of geometric and material nonlinearities. A decisive step forward can be found in the works of Raghavan and Brady, 2011; Støverud et al., 2011; Ehlers and Wagner, 2015 where DTI comes into play.

  In (Raghavan and Brady, 2011), the main idea was to use the fractional anisotropy (FA), a dimensionless index derived from DTI that measures the fraction of each voxel that can be assigned to anisotropic diffusion (Basser and Pierpaoli, 1996), to predict the WM ECS volume fraction and thus the effect on permeability. Moreover, they tried to predict how tissue deformation affects the backflow. Støverud et al., 2011 used the FA to distinguish between GM and WM and the same calibration approach described in (Linninger et al., 2008b; Linninger et al., 2008a) to derive an initial value of permeability. However, since Støverud et al., 2011 used a poro-elastic model, permeability changed according to local deformation. Finally, Ehlers and Wagner, 2015 developed the more complete brain model considering the brain as a multi-component porous medium composed of cells, interstitial fluid and vascular system. Even in this case DTI was used to infer brain tissue parameters following (Linninger et al., 2008a) approach.

In this brief overview, we have shown how different authors have faced the problem of defining a constitutive model for the solid part of the brain tissue. Of course, both approaches have pros and cons and choosing the best strategy is very dependent on the application or the specific issue to be addressed.

As a general comment, we can say that the deformable model are more correct because the brain is far from being a rigid medium, its Young's modulus is about 5,000 Pa and in open skull surgery, it can be clearly seen pulsating with the heartbeat (Støverud et al., 2011; Raghavan and Brady, 2011). Moreover, considering all the different phases as it was done by Ehlers and Wagner, 2015, it is surely a valuable attempt to have a comprehensive model.

Despite that, this type of model has a fundamental problem which is hard to tackle: the more a model is complicated and the more it will depend on the choice of the constitutive parameters to be used in the numerical equations. However, most of these parameters and their relation with tissue deformation, time after infusion and drug-cells interaction are far from being understood. For example, Ehlers and Wagner, 2015 affirmed that: "*A major drawback in computational biomechanics is still the almost impossible task of a proper (in vivo) determination of patient-specific material parameters*" and Støverud et al., 2011 said that: "*Even though permeability values for brain tissue can be found in the literature, there is still a large uncertainty in this parameter*".

On the other hand, rigid models offer simpler equations and therefore less parameters that depend on other physical quantity that are almost impossible to be determined *in vivo*. For this reason, most of the newer studies have adopted this type of strategy for modeling CED. The main assumption is that for a very low volumetric flow rate, for CED it is in the order of $\mu L/min$, the local deformation can be considered negligible. Moreover, using a simpler model means having a lower computational cost which is desirable also from a clinical perspective since hospital computational resources are usually limited.

1.4.2 Imaging

As it is clearly visible from Table 1.1, the introduction of DTI represented a step change in CED modelling. Indeed, it is very sensitive to changes at the cellular and microstructural level and it can describe the magnitude, the degree of anisotropy and the orientation of diffusion anisotropy (Alexander et al., 2007).

DTI was used to understand the diffusion principal directions in each voxel and consequently the permeability main directions (McGuire, Zaharoff, and Yuan, 2006). Moreover, DTI eigenvalues have been used to scale a baseline value of permeability and diffusivity as described in (Linninger et al., 2008a).

Only recently, Messaritaki et al., 2018 highlighted that, even though DTI is a powerful tool, it only encompass Gaussian diffusion for the water molecules thus leaving out non-Gaussian diffusion (NG-DTI). Accordingly, they advanced the hypothesis that numerical model prediction could be improved by considering also the non-Gaussian character of diffusion. Their results prove that there is actually a relevant difference between DTI based model and NG-DTI based model and encourage more research in this direction. However, their results still need to be validated.

Concluding, it is necessary to underline a common limitation that affects all DTI or NG-DTI based models. These types of imaging have a resolution which is in the order of mm^3 to be clinically feasible with conventional MRI machine and with usual time that a patient can spend in the MRI. However, the actual distance between neural cells in the ECS is in the order of nm (Syková and Nicholson, 2008; Nicholson and Hrabětová, 2017). Therefore, there is a very important difference between the *in vivo* imaging and the characteristic length where convection and diffusion take place.

1.4.3 Model validation

The validation process is a fundamental step to verify the goodness of a numerical model and to check its ability to predict how a drug diffuses in the brain tissue. However, validating CED model is extremely challenging and not all the numerical models here presented are combined with a proper validation process. This is due to a number of reasons, here we list the most important ones:

1. Difficult access to brain tissue to perform experiments: extracting the brain from a dead animal is a long and burdensome process that requires the presence of an expert veterinary with proper equipment.
2. Most of the last studies use MRI and DTI to reconstruct the brain geometry and infer model parameters. To have a reliable validation, there should be a perfect registration between preoperative images, postoperative images, the model geometry and the pose of the catheter. However, this is not trivial as suggest also by Kunwar et al., 2010 that highlights the fact that most of the catheter insertions performed on 296 patients were misplaced.
3. Brain tissue tends to lose its physical and mechanical properties in less than 24 hours after death. Therefore, to have reliable data, researchers should perform their analyses *in vivo* which is much more complex and expensive than conducting experiments *ex vivo*.
4. The heterogeneity and anisotropy of the brain tissue make it very difficult to mimic its mechanic behaviour with artificial materials such as hydrogels. However, some attempts in this direction have been made (Forte et al., 2014; Forte et al., 2016).

1.5 Thesis motivation

Even though researchers have started to tackle the problem of enhancing the level of accuracy in modelling CED in multiple ways, an unneglectable gap is still preventing clinicians to easily and fully take advantage of numerical models. Analysing the state of the art, we have identified three main limitations that affect all the proposed models.

Firstly, there is an urgent need for a reliable estimate of the brain constitutive parameters. The latter are, independently from the model used, the foundation on which a model is build. Obviously, as we use more and more complicated models, the number of parameters to be determined increases. However, as highlighted in (Ehlers and Wagner, 2015; Støverud et al., 2011; Vidotto et al., 2019a; Vidotto, Dini, and De Momi, 2018; Vendel, Rottschäfer, and

Lange, 2019), there is still a huge uncertainty in most of them. In particular, we pinpoint the fact that permeability and tortuosity, that are key parameters for the convective and diffusive part of the flux, can vary up to three orders of magnitude (Vidotto et al., 2019a; Vidotto, Dini, and De Momi, 2018).

Secondly, we have shown that most models use DTI as a way to extract *in-vivo* information on the brain microstructure and only recently Messaritaki et al., 2018 have raised a doubt on this paradigm. However, even DTI or NG-DTI are themselves models which are based on simplifying assumptions on the WM and GM structure. Indeed, there is a wide branch of researchers working on the development and validation of DTI models. Moreover, the clinical standard in terms of imaging time per patient limits the DTI to a resolution which is very far from the nanometric scale where convection and diffusion occurs. For this reason, from DTI it is possible to infer if a voxel belongs to isotropic GM or anisotropic WM but it is not possible to obtain any detailed information about the microstructure. Therefore, it is our opinion that more efforts should be addressed towards understanding the role of the microstructure geometry in influencing convection and diffusion parameters.

The third limitation is a consequence of the first two. As stated also by Holter et al., 2017, analysing the brain microstructure is pivotal to shed light on controversial parameters and to bridge the gap between the microscale and clinically feasible imaging techniques. To this end, it would be desirable to have access to reconstructed volumes of GM and WM areas. However, acquiring high-quality microscopy images is very expensive both in terms of resources and time and there are relatively few robust automatic methods for segmenting the cellular structures (Vidotto et al., 2019b).

1.5.1 Aim of the thesis

CED is the most encouraging approach to inject chemotherapeutic agents directly into the brain, but a high variability in the results still do not allow a clinical use. Therefore, the overall goal of this dissertation is to implement an effective model of the drug distribution in the brain when using CED thus narrowing the gap between prediction and real outcomes. Through the analysis presented, the central role of the brain microstructure and its relation with convection and diffusion parameters is studied. The study aims at obtaining insights that would help in developing more comprehensive and reliable predictive models.

To do so, the analysis first focuses on the study of a fundamental parameter for the convective transport of drug molecules inside the brain, namely the hydraulic permeability. As already mentioned, this parameter is controversial and can vary up to three orders of magnitude (Vidotto et al., 2019a; Holter et al., 2017). To shed light on this aspect, we started by developing a geometrical model resembling the WM microstructure. The model encompasses the main characteristics of the WM available in the literature such as Axon Diameter Distribution (ADD) (Liewald et al., 2014), ECS volume fraction and ECS width (Syková and Nicholson, 2008). From this model, we gained two important information. First, we estimated the size of the representative volume element (RVE), namely the minimum size of a volume of WM to be analysed to have reliable and repeatable results. Secondly, we computed the hydraulic permeability in three WM structures (corpus callosum, superior fascicle and inferior fascicle) (Vidotto et al., 2019a)[1].

Using the same model in terms of geometry but with a Monte Carlo based simulation approach, we calculated the WM tortuosity, another controversial parameter which is important for the diffusive part of the mass transport equation (Vidotto, Dini, and De Momi, 2018)[2].

Despite the works explained above gave important insights on the effects of the WM microstructure on transport parameters, they are still based on a geometrical model that is different from the real WM anatomy. To tackle the issue, we developed a Fully Convolutional Neural Network (FCNN) to segment the cellular phase from Electron Microscopy (EM) images of WM samples. We tested the algorithm on a publicly available dataset obtaining good results (Vidotto et al., 2019b)[3].

---

[1] Vidotto, Marco et al. (2019a). "A computational fluid dynamics approach to determine white matter permeability". In: *Biomechanics and modeling in mechanobiology*, pp. 1–12.

[2] Vidotto, Marco et al. (2018). "Effective diffusion and tortuosity in brain white matter". In: *2018 40th Annual International Conference of the IEEE Engineering in Medicine and Biology Society (EMBC)*. IEEE, pp. 4901–4904.

[3] Vidotto, Marco et al. (2019b). "FCNN-based axon segmentation for convection-enhanced delivery optimization". In: *International journal of computer assisted radiology and surgery*. 14.3, pp. 493–499.

Then, in collaboration with Imperial College of London and Università Statale of Milan, we acquired scanning EM images of a couple of WM areas from a sheep brain. Note that it was not possible to segment the cellular phase (solid phase of the porous medium) with the algorithm previously developed because the images were quite noisy and blurred. Therefore, we preferred a manual segmentation that allowed us to separate the solid and fluid phases with higher precision. Twenty slices for every volume were manually segmented and imported in the finite element solver ANSYS FLUENT. In each slice, we computed the velocity and pressure fields necessary to obtain an average value of permeability. Since the WM is a porous material with a strongly anisotropic structure, we focused our attention on this aspect. The results confirm our hypothesis leading to significantly different values of permeability in case of flux parallel or perpendicular to the WM fibres (Vidotto, De Momi, and Dini, N.D.)[4]. Moreover, these values are in good agreement with the model developed in Vidotto et al., 2019a and the relevant literature.

To validate our computational results, we designed an experimental campaign in collaboration with Imperial College London. We modified an already existent benchmark for measurement of outflow facility of eye (*iPerfusion*) (Reina-Torres et al., 2016) to experimentally measure the hydraulic permeability in WM areas from ovine brains. The benchmark is controlled applying a constant pressure and measuring the flow rate. In this work, we confirm the findings highlighted in the previous chapter namely the anisotropic behaviour of the WM (Jamal et al., N.D.)[5].

Finally, in collaboration with Imperial College London and San Raffaele Hospital, we worked on a comprehensive predictive model for CED interventions that could take into account the contribution of the WM microstructure analysed in our previous studies. To do so, we integrated the Neurite Orientation Dispersion and Density Imaging (NODDI) (Zhang et al., 2012), a multi shell DTI imaging modality that includes microstructural information

---

[4] Vidotto, Marco et al. (N.D.). "White matter microstructure role for hydraulic permeability: a new electron microscopy images based approach". To be submitted to *Proceedings of the National Academy of Sciences*.

[5] Jamal, Asad et al. (N.D.). "Infusion mechanisms in brain white matter and its dependence of microstructure: an experimental study of hydraulic permeability". Under review in *IEEE Transaction of Biomedical Engineering*.

(Vidotto et al., N.D.)[6].

The main objectives of the PhD research are summarized in the following topics:

- **O1** Understanding the RVE size of a WM sample to analyse to have reliable and repeatable results and compute reference values of hydraulic permeability **O1.1** (Chapter 2) and tortuosity **O1.2** (Chapter 2)
- **O2** Conduct an in depth study on the hydraulic permeability from EM images thus considering the real WM microstructure and eventually develop an automatic method to distinguish between solid and fluid phase in WM samples **O2.1** (Chapter 3).
- **O3** Validate the numerical results with an ad hoc experimental analysis (Chapter 4).
- **O4** Integrate the information in a comprehensive CED predictive model showing the difference with previous studies (Chapter 5).

1.6 Outline

This dissertation is organized in six chapters:

- Chapter 1 - *Motivation and Background:* in the first chapter the research context, motivations and thesis aim are outlined. An overview of CED modelling is presented.
- Chapter 2 - *Permeability and tortuosity from a geometrical model:* in the first part of this chapter, a computational fluid dynamics approach to determine WM permeability is presented. A WM geometrical model is developed starting from the main characteristics of the WM available in the literature. Then, solving the velocity and pressure fields across the porous medium, we estimate the size of the RVE and we compute a reference value of hydraulic permeability in three WM structures.

---

[6] Vidotto, Marco et al. (N.D.). "Advanced imaging methods to improve the predictive capabilities of CED models". Under second review in *Annals of Biomedical Engineering*.

In the second part of the chapter, we exploit a three-dimensional evolution of the geometric model previously developed to measure tortuosity in brain WM. A Monte Carlo based simulation environment is presented and used to evaluate the hindrance to diffusion caused by the tortuous pathways between the axons. Tortuosity in the direction parallel to the axons is used to prove the soundness of the method matching the results expected theoretically. On the other hand, tortuosity perpendicular to the axons appears to increase as the ECS volume fraction and ECS width decrease.

- Chapter 3 - *White matter permeability from electron microscopy imaging:* in this chapter, an electron microscopy imaging based study to address WM permeability is presented. In the first part of the chapter, a FCNN is implemented to segment the axons thus separating the solid and liquid phases. The second part of the chapter focuses, in particular, on the role of the WM microstructure. Starting from EM images, we demonstrate that the hydraulic permeability in the direction parallel to the axons is significantly higher than the one perpendicular to the axons. Moreover, we show that two brain areas, despite both belonging to the WM, exhibit a significant difference in WM permeability.

- Chapter 4 - *Experimental study of hydraulic permeability:* in the fourth chapter, an experimental study of hydraulic permeability is presented. An infusion mechanism is used to study the brain WM and its dependence on microstructure. This work represents the experimental validation of the results achieved in Chapter 2 and Chapter 3. Besides demonstrating the reliability of the numerical results, this chapter also deepens the role of the pressure applied and the time post-mortem.

- Chapter 5 - *CED predictive numerical model:* in this chapter, advanced imaging methods to improve the predictive capabilities of CED models are used. An innovative predictive model based on the integration of DTI and NODDI analyses is compared with a state of the art model by simulating a CED intervention on a healthy subject. The results clearly reveal a significant difference between the two models in terms of drug distribution volume, concentration profile and linear penetration length. We believe that our model introduces a more comprehensive way to describe the permeability tensor which relies on the integration of our previous analyses with a clinically feasible imaging technique.

- Chapter 7 - *Conclusions:* in the last chapter the dissertation's conclusion are drawn, highlighting scientific contributions, future perspectives and limits.

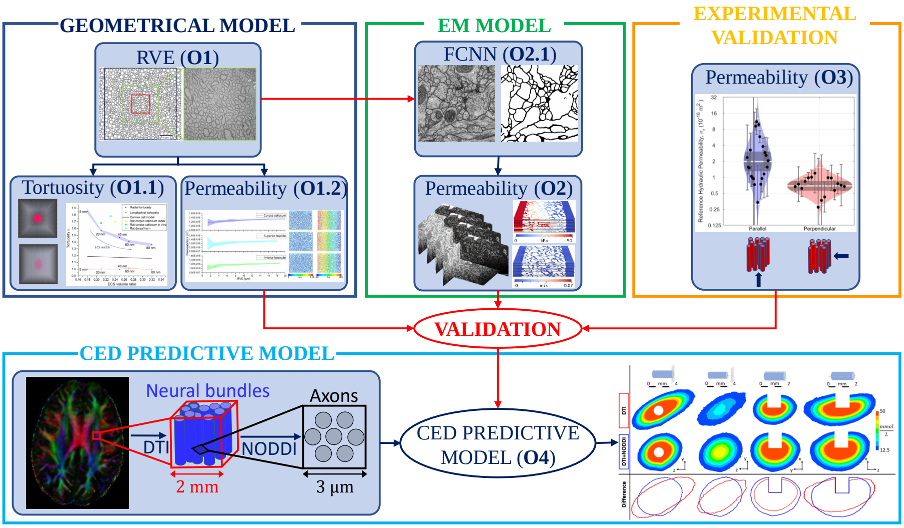

FIGURE 1.5: Schematic illustration of the proposed research. The brain WM is studied following three approaches: the first is based on a WM geometrical model and it is used to evaluate permeability and tortuosity (blue box, Chapter 2). The second, which starts from EM images represents a step forward towards a more realistic description of the real WM microstructure (green box, Chapter 3). The third is an experimental campaign that is used to validate the previous approaches (yellow box, Chapter 4). Finally, the relation between permeability and WM microstructure is integrated in a comprehensive CED predictive model and tested using the imaging dataset from a healthy subject (light blue box, Chapter 5).

Chapter 2

Permeability and tortuosity evaluated starting from a geometrical model of the white matter

The first part of this chapter* proposes a method to compute a fundamental parameter for convection-enhanced delivery modelling outcomes, the hydraulic permeability, in three brain structures. Therefore, a two-dimensional brain-like structure is built out of the main geometrical features of the white matter: axon diameter distribution extrapolated from electron microscopy images, extracellular space volume fraction and extracellular space width. The axons are randomly allocated inside a defined border, and the extracellular space volume fraction as well as the extracellular space width maintained in a physiological range. To achieve this result, an outward packing method coupled with a disc shrinking technique is implemented. The fluid flow through the axons is computed by solving Navier–Stokes equations within the computational fluid dynamics solver ANSYS. From the fluid and pressure fields, an homogenisation technique allows establishing the optimal representative volume element size. The hydraulic permeability computed on the representative volume element is found in good agreement with experimental data from the literature.

In the second part of this chapter**, a new method to compute tortuosity, a key parameter for drug diffusion in fibrous tissue, is presented. Tortuosity is a measure of the hindrance to diffusion caused by the intricate paths between the axons. We develop a three-dimensional version of the previously defined geometrical model with the axons simulated as straight parallel cylinders. Then, using a Monte Carlo based simulation, we show that tortuosity is different in the direction parallel or perpendicular with respect to the axons. In the first case, it is always equal to 1, as predicted theoretically, thus proving the reliability of the model. In the second case, tortuosity increases from 1.35 to 1.85 as the extracellular space width and the extracellular space volume fraction decrease. The results are in good agreement with the experimental data reported in the literature.

*This work has been published as: Vidotto, M., Botnariuc, D., De Momi, E. & Dini, D. (2019). “A computational fluid dynamics approach to determine white matter permeability”, *Biomechanics and Modeling in Mechanobiology*, 18:1111–1122.

**This work has been published as: Vidotto, M., Dini, D., & De Momi, E. (2018). "Effective diffusion and tortuosity in brain white matter", *International Conference of the IEEE Engineering in Medicine and Biology Society*, 2018:4901-4904.

2.1 Introduction

The most common brain malignant tumour, glioblastoma multiforme, leaves patients a median overall survival rate ranging from 12 to 18 months, as reported in Mehta et al., 2015. Moreover, despite affecting only 6 in 100,000 people, the treatment cost in Europe in 2010 was about 5.2 billion Euro (Olesen et al., 2012). Conventional treatment options such as surgery, chemotherapy and radiation have not proved themselves as decisive, despite being highly aggressive for the patients (Crawford, Rosch, and Putnam, 2016). Therefore, Bobo et al., 1994 introduced a new technique, namely Convection-Enhanced Delivery (CED), which has shown encouraging results with recurrent glioblastoma in the last twenty years (Crawford, Rosch, and Putnam, 2016). Indeed, it allows overcoming the main obstacle to pharmaceutical treatment of tumour, the blood-brain barrier, by injecting a therapeutic agent under positive pressure directly into the parenchyma.

A key aspect to reach good results is the ability to predict, in the preoperative phase, the distribution of the drug inside the tumour (Raghavan et al., 2006; Raghavan, Brady, and Sampson, 2016). This would allow planning the infusion point and the flow rate to optimise the treatment. Several studies have been conducted in the last fifteen years proposing numerical models which were based on different assumptions (Ehlers and Wagner, 2015; Støverud et al., 2011; Linninger et al., 2008a; Kim et al., 2012; Sarntinoranont et al., 2006; Chen and Sarntinoranont, 2007; Morrison et al., 1999; Raghavan et al., 2006; Raghavan and Brady, 2011; Smith and García, 2009). Nonetheless, the cerebral tissue complex structure has represented a formidable challenge to modelling and more studies should be conducted to reach a satisfying level of accuracy. As suggested by Ehlers and Wagner, 2015 and Støverud et al., 2011, this could be due the fact that the constitutive parameters which are used in the models vary significantly across the scientific literature (up to three orders of magnitude). Therefore, in this paper, we aimed to shed light on the hydraulic permeability which is one of the key parameters affecting CED outcomes. Indeed, it drives the convective flux through the brain thus determining the pharmaceutical agent ability to spread within the cancerous tissue.

The brain could be divided in three main components characterised by different properties: cerebrospinal fluid (CSF), grey matter and white matter (WM). The CSF can be found in all the empty spaces within the skull thus comprising the gap between the brain and the skull, the ventricles and the extracellular space (ECS). The grey matter consists of neuron cell bodies which are highly packed making the tissue very dense. In contrast, the WM can be found in the inner part of the brain and presents a more regular structure made of elongated parallel axons with a quasi-circular cross section (Støverud et al., 2011). In addition, the blood vessel system runs through the parenchyma to supply oxygen and nutrients. This simplified description of the brain is not meant to be exhaustive but highlights that the brain is a multi-phasic material (Ehlers and Wagner, 2015). Nevertheless, as pointed out by Tavner et al., 2016, the correct mathematical framework to model the brain parenchyma is still a controversial subject which depends on the specific phenomenon studied.

In this work, since the blood vessels occupy less than 3% of the total volume (Duval, Stikov, and Cohen-Adad, 2016), we describe the WM as a biphasic continuum in which the axons represent the solid phase which is immersed in the ECS which constitutes the fluid phase. Under the hypotheses of incompressible fluid and very low Reynolds number, the convective flux through the axons can be described by means of Darcy's law, which relates the pressure loss across a porous medium with its average velocity according to the hydraulic permeability (Dullien, 2012; Kim et al., 2012; Støverud et al., 2011; Ehlers and Wagner, 2015). The latter depends only on the porous media geometry and the fluid properties (Yazdchi, Srivastava, and Luding, 2011), and it can be computed in three different way:

(i) Experimentally: numerous experimental techniques have been developed and described in the geotechnical literature (Türkkan and Korkmaz, 2015) but, to the best of our knowledge, only a limited number of studies can be found concerning human tissues (Swabb, Wei, and Gullino, 1974; Netti et al., 2000; McGuire, Zaharoff, and Yuan, 2006; Franceschini et al., 2006).

In particular, Swabb, Wei, and Gullino, 1974 conducted the first *in vitro*

experimental campaign which aimed to infer the hydraulic permeability of hepatocarcinoma, the most common liver cancer. Netti et al., 2000 performed confined compression test on slices of freshly excised tissue belonging to four tumour lines. Then, they estimated the permeability fitting the experimental data with a poroviscoelastic model. McGuire, Zaharoff, and Yuan, 2006 followed a similar approach implanting three tumour lines in mice. Then, after the injection of a controlled flow of Evans blue-labeled albumin in the centre of the cancerous tissue, the latter was excised and sliced. Finally, the albumin distribution was fitted by means of Darcy's law for unidirectional flow in an infinite region around a spherical fluid cavity. Franceschini et al., 2006 conducted an extensive and comprehensive work in which they performed several types of mechanical tests on human brain samples within 12 hours of death. Without entering into details, we will just focus on the permeability extraction. They performed an oedometric test on 12 cylindrical specimens harvested in the parietal lobe. The average ratio between initial and final specimen's shortening under a loading step, namely consolidation ratio, was depicted as a function of time. These data were fitted according to Terzaghi theory thus allowing to infer the permeability.
Despite the works cited above being extremely valuable, they are affected by two important limitations. First, the permeability in not measured directly but it is inferred from a model which is based on certain assumptions and, second, the hydraulic permeability decreases with time post-mortem and its estimation is therefore affected by the exact time measurements have taken place (Tavner et al., 2016).

(ii) An alternative methodology with respect to the experimental one is using the Kozeny-Carman equation which relates permeability to other geometrical parameters such as porosity and specific surface; for details the reader can refer to Xu and Yu, 2008 and citation therein. However, the major drawback of the analytical approach is that it is only suitable for simple and regular geometries but cannot be applied to complicated structures such as the WM.

(iii) Finally, in the numerical approach, Navier-Stokes equations are solved to obtain the permeability under some hypotheses. It has been proven to be a powerful tool to analyse random arrangements of fibres as shown in (Hitti, Feghali, and Bernacki, 2016; Nedanov and Advani, 2002; Takano et al., 2002) or other porous media (Pinela et al., 2005; Kolyukhin and Espedal, 2010; Dias et al., 2012; Zeng et al., 2015; Eshghinejadfard et al., 2016). For example, Hitti, Feghali, and Bernacki, 2016 computed the permeability of a unidirectional disordered fibres array with constant diameter by first assessing the velocity and the pressure fields of the convective flow through them. Then, by means of an homogenisation method they obtained the permeability of the whole domain.

In this paper, we develop an approach that for the first time applies numerical techniques to the study of the brain microstructure. The brain geometry and spatial organisation are considered to describe the inter-axons convective flux.

We present an outward packing method to create a bi-dimensional random geometry based on the Axon Diameter Distribution (ADD) provided by (Liewald et al., 2014) that ensures an extracellular space (ECS) volume fraction and an ECS width in the physiological range (Syková and Nicholson, 2008). Moreover, a spatial analysis, by means of Ripley's k-function (Hansson, Jafari-Mamaghani, and Krieger, 2013; Marcon, Traissac, and Lang, 2013), is conducted to guarantee that the overall geometrical organisation is consistent with the one of the experimental data. Then, a computational fluid dynamics (CFD) model is implemented within the commercial software ANSYS (ANSYS, Lebanon, NH) to compute the WM hydraulic permeability which will be compared with other data available from the relevant literature.

2.2 Methods

2.2.1 Dataset

In the study conducted by Liewald et al., 2014, the authors measured the inner diameter of myelinated axons in three anatomical structure namely corpus callosum (CC), superior longitudinal fascicle (SF) and uncinate/inferior occipitofrontal fascicle (IF). Their analysis was performed on three human brains and a monkey brain. Since the first ones underwent a late fixation that could lead to degradation of cellular material and a reduction of hydraulic permeability as pointed out by Tavner et al., 2016, we used the ADD of the monkey which guaranteed an higher fixation quality. Moreover, since we are interested in the external diameter, we added the average myelin sheath width, measured by Liewald et al., 2014, to the ADD.

2.2.2 Brain-like geometry

The first objective was to design a geometry which could mimic the WM structure and spatial organisation. Therefore, we created a two-dimensional random disordered fibres packing with a circular cross section which met four important geometrical requirements that drive the convective flux in the extra cellular space: axon diameter distribution, ECS volume ratio, ECS width and spatial organisation.

The generation algorithm was based on the closed form advancing front approach presented by Feng, Han, and Owen, 2003, but with a main difference. This work introduces an optimisation phase which pushes the ECS volume fraction at a lower level with respect to the previous method in order to meet the physiological requirements. All the algorithm here presented was developed in the environment provided by MATLAB:

1. The user specifies the total number of fibres, which are represented by discs of varying diameters in our two-dimensional representation, and the desired ADD and ECS volume ratio. Then, he indicates the shape of the domain inside which he wants to insert the discs, e.g a square or a rectangle with a certain ratio between adjacent edges. The initial domain area and its boundaries are computed from the sum of each disc area using simple geometrical arguments and calculations. This initial area is not big enough to host all the discs because it does not consider the empty spaces. Therefore, the area increases iteratively until all the discs have found space.

2. The algorithm is based on the following geometrical consideration: given a couple of discs, it is always possible to add a third one which is

tangent to both of them if the distance between the first two is less than the diameter of the third; this is schematically depicted in Figure 2.1 (a). Figure 2.1 (b) shows the polygon formed by the disc centres which constitutes the front along which the generation algorithm propagates. Each new disc is accepted if it is contained inside the domain boundaries and if no overlapping with the other discs occurs.

3. Once all the discs are placed in the domain, the ECS volume ratio is computed as the ratio between the void spaces between the discs and the total area. The outcome of this first part of the algorithm is a highly packed structure with an ECS volume ratio of about 0.22.

4. However, as stated by Syková and Nicholson, 2008, the ECS volume ratio can reach a minimum of 0.15 in the brain; for this reason we implemented an optimisation algorithm which fills the empty spaces in the structure. It could be summarised in four additional steps:
    - (i) The original geometry is converted in a black and white image to allow morphological analyses, which are a collection of non-linear operations related to the shape or morphology of features in an image (Patil and Bhalchandra, 2012).
    - (ii) The subsequent step is the skeletonization that, starting from a black and white image, uses the iterative thinning algorithm to reduces all the objects to lines, without changing the essential structure of the image (Haralick and Shapiro, 1992). The branch points of the skeleton represent the location where the distance between close discs is maximised. In other words, they are the best locations where it is possible to add new discs as can be appreciated in Figure 2.1 (c).
    - (iii) Even in this case the new disc is accepted if its diameter is comprised in the range of the ADD previously defined.
    - (iv) The process continues iteratively until reaching the minimum physiological ECS volume ratio.

5. Finally, the desired porosity is achieved by means of a shrinking technique as described in Hitti, Feghali, and Bernacki, 2016. It is easy to understand that the discs shrinking affects the desired ADD. However, for the physiological porosity range, which does not exceed 0.3, the shrinking produces a decrease in the axons diameter of only 2.5% which could be considered negligible.

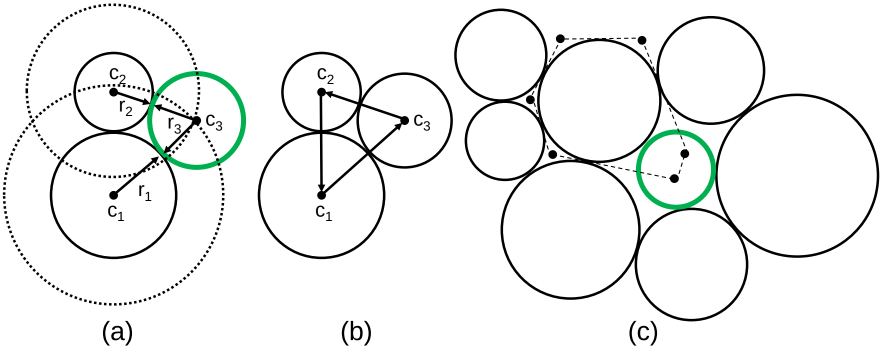

FIGURE 2.1: Discs generation algorithm: (a) given two discs with radius r_1 and r_2 and centred at c_1 and c_2 respectively, the centre c_3 of the new disc (green) with radius r_3 is given by one of the two intersections of the dotted discs with radius $r_1 + r_3$ and $r_2 + r_3$ centred at c_1 and c_2 respectively; (b) the first three discs form the initial propagation front, a new disc is added on the right side of each arrow; (c) in the second part of the algorithm, new discs are added at the skeleton branch points (black dot) if their diameter is comprised in the ADD.

It must be noticed that the second part of the algorithm, where the empty spaces are filled with discs, changes the ADD. Indeed, since the void spaces are small, they are more likely occupied by the discs with a smaller diameter. Nevertheless, this limitation could be considered negligible as discussed in Appendix A.

2.2.3 Spatial distribution analysis

To compare the permeability evaluated both within the same ADD and between different ADDs as a function of ECS volume ratio, it was necessary to ensure that the spatial organisation of every geometry was consistent. Therefore, the ability of the algorithm described in subsection 2.2.2 to create random arrangements of axons was quantified by means of Ripley's function (Ripley, 1976). The axon centres represent a spatial point process, see the contribution by Diggle, 2003 for details, and Ripley's function was used to differentiate between: (i) aggregation, where the points tend to stay close to other points, (ii) inhibition where the points form a regular pattern and (iii) complete spatial randomness (CSR) where the points do not follow any specific rule (Jafari-Mamaghani, 2010; Lang and Marcon, 2010; Marcon, Traissac, and Lang, 2013).

Moreover, we compared the model spatial organisation with the experimental one analysing the transmission electron microscopy (TEM) images provided by Liewald et al., 2014. Therefore, as a preliminary step, we manually segmented the microscopy images and computed the centroids for each anatomical structure (Gopi, 2007).

Ripley's function is defined as:

$$R(t) = p^{-1}E \tag{2.1}$$

where p is the number of points per unit area, namely the intensity, and E is the number of extra points within a distance t, which is the distance scale considered, of an arbitrary point (Ripley, 1976). For a homogeneous Poisson process that characterises the CSR:

$$R(t) = \pi t^2 \tag{2.2}$$

given the location of all points within a domain, the equation below describes how to compute R:

$$R(t) = p^{-1} \sum \sum w(l_i, l_j)^{-1} \frac{I(d_{ij} < t)}{N} \tag{2.3}$$

where d_{ij} is the distance between the i^{th} and j^{th} points, N is the total number of points and $I(x)$ is a function whose value is 1 if the distance between the i^{th} and j^{th} points is less than t and otherwise is zero. Finally, $w(l_i, l_j)$ provides the edge correction to minimise the effects that arise because points outside the boundary are not counted (Dixon, 2002). Usually, it is convenient to linearise the R-function as:

$$L(t) = \sqrt{\frac{R(t)}{\pi}} \tag{2.4}$$

because the $L - function$ plot for a CSR distribution is a simple line with an angular coefficient equal to 1 and passing from the origin. On the contrary, for clustering and inhibition the angular coefficient is higher and lower than 1 respectively. Thus, it is easier to show the deviation from CSR and the length scale at which it occurs (Dixon, 2002; Hitti, Feghali, and Bernacki, 2016; Chen and Sarntinoranont, 2007).

2.2.4 Brain convection model

In the brain the axons represent the solid phase of the WM which is immersed in the ECS. As well as the other cells, they could be modelled as a soft tissue but a unique answer on which constitutive model is more appropriate is still missing. For example, for Støverud et al., 2011 the solid phase behaves as an isotropic linear elastic material whereas Ehlers and Wagner, 2015 used a hyperelastic model. On the other hand, other authors stated that, if the flow rate is very low the deformation provoked by the fluid-structure interaction can be considered negligible and therefore, it is possible to safely model the axons as a rigid material (Kim et al., 2012; Kim, Mareci, and Sarntinoranont, 2010; Raghavan and Brady, 2011). Since the interest of this study is to infer the permeability in a quasi-static condition (creeping flow), we follow the latter approach and we model the solid phase as a rigid porous media, whose continuity equation is:

$$\nabla \cdot \mathbf{v} = 0 \tag{2.5}$$

where $\mathbf{v}$ is the fluid superficial velocity.

The well-known Darcy's law is a macroscopic relation between the pressure loss ∇p and $\tilde{\mathbf{v}}$ which is the velocity through the pores averaged on the fluid volume V_f (equation 2.6 and 2.7 respectively)

$$\tilde{\mathbf{v}} = \frac{\mathbf{k}}{\mu} \nabla p \tag{2.6}$$

$$\tilde{\mathbf{v}} = \frac{1}{V} \int_{V_f} \mathbf{v} dV \tag{2.7}$$

where $\mathbf{k}$ is the permeability of the porous media, μ is the viscosity of the fluid ($10^{-3}\ Pa \cdot s$) (Jin, Smith, and Verkman, 2016), V and V_f are the total and fluid volume respectively (Yang, Lu, and Kim, 2014; Hitti, Feghali, and Bernacki, 2016). The superficial velocity though the pores was computed solving the Navies-Stokes equations by means of the Finite Element Method (FEM) software ANSYS (ANSYS, Lebanon, NH) with Semi-Implicit Methods for Pressure Linked Equations (SIMPLE) (ANSYS, 2017). A no slip condition was set on each wall and the conduct length was designed to have a fully developed flow before the porous zone. The boundary condition at the inlet (velocity inlet 0.0024 m/s) was chosen to have a very low Reynolds number $Re \approx 10^{-3}$ to respect Darcy's law hypothesis and to have a velocity close to the one that is usually used in CED intervention (Barua et al., 2013; Barua et al., 2014). A zero pressure was applied at the outlet to reproduce the conventional experimental conditions for measuring hydraulic permeability (Yazdchi, Srivastava, and Luding, 2011; Truscello et al., 2012; Hitti, Feghali, and Bernacki, 2016).

2.2.5 Representative Volume Element (RVE) size determination

According to Drugan and Willis, 1996 an RVE is: *"the smallest material volume element of the composite for which the usual spatially constant (overall modulus) macroscopic constitutive representation is a sufficiently accurate model to represent the mean constitutive response"*. However, as stated by Du and Ostoja-Starzewski, 2006, a lot of studies are based on the existence of a so-called RVE but only a few of them have quantitatively determined its size with respect to the micro–heterogeneity. As previously described in subsection 2.2.2, the ECS volume ratio can range between 0.18 and 0.3, however, we decided to limit our study to geometries with the highest value for the following reason. Since the space between each axon is proportional to the ECS volume ratio, choosing a value equal to 0.3 leads to a geometry with a larger ECS width. This characteristic is strongly desirable from a computational point of view, indeed the smaller the inter-axons space is, the more the meshing process becomes challenging and the simulation dramatically more time-consuming.

In this work, we created 6 (n) random structures for each ADD (CC, SF and IF). The mean permeability $\bar{k}$ and the standard deviation σ were computed for each brain zone as a function of the RVE size.

$$\bar{k} = \frac{1}{n}\sum_{i=1}^{n} k_i \tag{2.8}$$

$$\sigma = \sqrt{\frac{1}{n-1}\sum_{i=1}^{n}(k_i - \bar{k})} \tag{2.9}$$

The RVEs size was determined dividing the height of each model geometry by 20 as shown in Figure 2.2 which also depicts a comparison between the model geometry and a TEM image belonging to the SF. However, only the first 16 RVEs were considered for the calculation as a consequence of the *channelling effect* described in Nield and Bejan, 2013 which rises at the walls. A detailed explanation can be found in Appendix B.

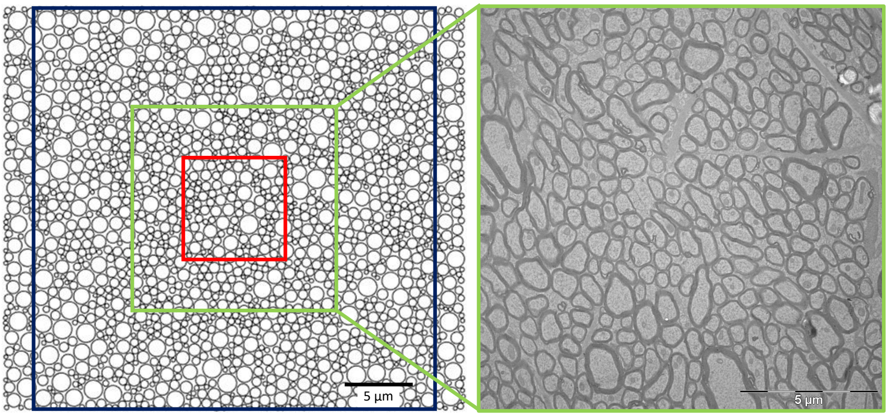

FIGURE 2.2: On the left: each model geometry was divided in 20 square RVEs whose edge length is a fraction of the porous media height. The picture shows 5/20 (red), 10/20 (green) and 20/20 (blue); On each RVE the permeability was computed by means of Darcy's law. On the right: TEM image of the SF, with courtesy of Prof. Dr. Almut Schüz (Liewald et al., 2014).

2.3 Results

2.3.1 Geometry

Figure 2.3 shows the relationship between two geometrical parameters that are fundamental in determining the fluid dynamics within a porous media, namely, the ECS volume ratio α and the ECS width d. The latter has been identified by Syková and Nicholson, 2008 as an "atmosphere" surrounding every axon which can be quantified by the following equation:

$$d = \frac{V_{axon}}{S_{axon}} \frac{\alpha}{1-\alpha} \tag{2.10}$$

where V_{axon} and S_{axon} are the average axon volume and surface area for an ideal thin slab of length equal to 1 μm. As depicted in Figure 2.3 the ECS width in our model increases in a quasi-linear fashion with the ECS volume ratio from a minimum of 16 nm to a maximum of 35 nm which is comparable with the range identified by Syková and Nicholson, 2008. The minimum ECS volume ratio that we were able to reach with our method was equal to 0.18, which is very close to the experimental minimum value of 0.15 (Syková and Nicholson, 2008).

Figure 2.4, depicts the results of Ripley's function analysis applied to the TEM images and to the geometry generated through the algorithm described in subsection 2.2.2. Moreover, it is possible to compare them with the ideal case of CSR. We can observe that in all the anatomical structures the spatial organisation of both real and model axons is almost coincident to the CSR as we approach the final part of the curve. It should be noted that there is an initial discrepancy between the experimental and the model trend. However, this could be easily explained since the number of axons for each image was significantly lower than the one in the model. Therefore, the presence of big axons in the TEM images strongly affects the analysis whereas their effect is mitigated in the model geometries. Nonetheless, for t equal to 1 which is a normalised value corresponding to the 25% of the image length as suggested in Jafari-Mamaghani, 2010, both experimental and model data converge to CSR.

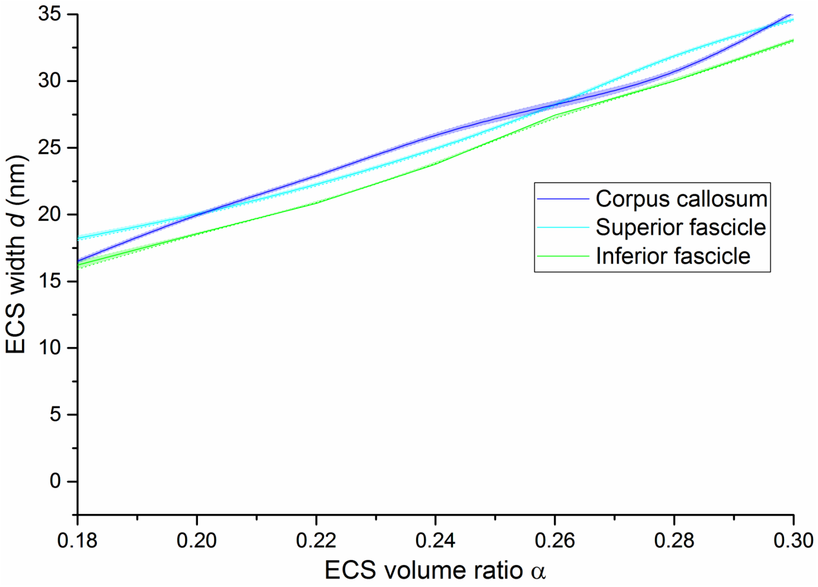

FIGURE 2.3: The ECS width is represented as a function of the ECS volume fraction for CC, SF and IF. The ECS width increases in quasi-linear way from a minimum of 16 to a maximum of 35 nm.

2.3.2 Grid sensitivity analysis

The first important step is to perform a grid-sensitivity analysis to find the correct trade-off between the discretisation error reduction and the cost of the simulation in terms of computational time (Montazeri and Blocken, 2013). The grid resolution depends on different parameters; we varied separately the maximum face size allowed for each cell and the edges' discretisation in the porous zone (ANSYS, 2017). We compared 6 grids with an increasing number of nodes, from a coarse one, characterised by 14862 nodes and an average element size of $0.16 \cdot 10^{-2}$ μm^2, to a finer one corresponding to 153496 nodes and $0.015 \cdot 10^{-2}$ μm^2 average element size. In Figure 2.5, it is possible to appreciate the geometry used for the grid-sensitivity analysis and the lines along which the velocity has been computed, the results of the analysis are shown on the right. The independence of the average velocity from the grid resolution is

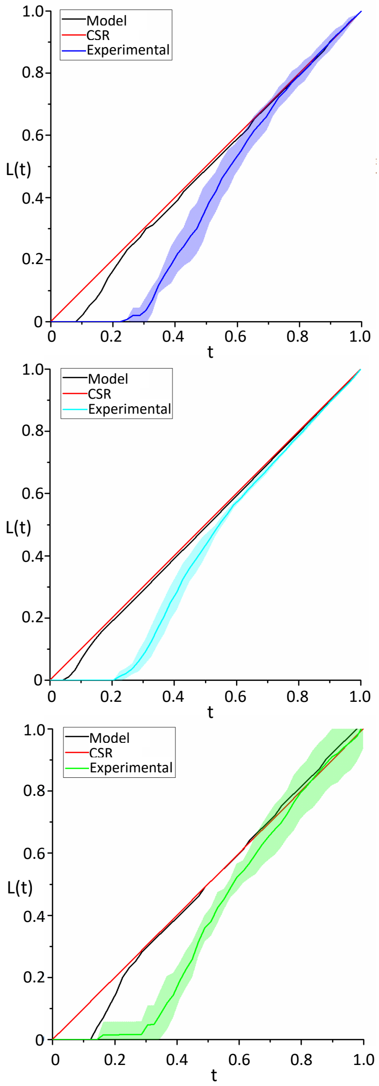

FIGURE 2.4: In each graph is possible to appreciate the comparison between the $L-function$ under ideal CSR hypothesis (red line), the $L-function$ obtained with model described in section 2.2.2 and the $L-function$ computed on the TEM images of CC (blue), SF (light blue) and IF (green).

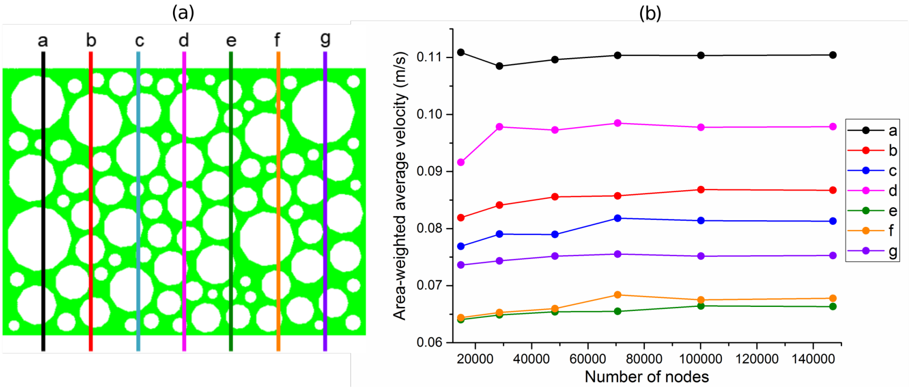

FIGURE 2.5: (a) Geometry used to perform the mesh sensitivity analysis, also showing the lines along which the velocity has been averaged. (b) Effect of the grid resolution on the area-weighted average velocity is shown. Note that convergence is reached after about 100000 nodes.

achieved for a number of nodes close to 10^5. Indeed, the percentage error between the grids with 100155 and 147016 nodes ranges between 0.08 and 0.4%, which can be considered negligible (Montazeri and Blocken, 2013). Therefore, further analysis were performed following the discretization features of the 100155 nodes grid which has been proven to assure high accuracy and adequate computational cost. The simulations took 3 hours on a workstation with a i7-6800K 6 cores 3.60 GHz CPU and 16 GB of memory.

2.3.3 RVE size

Figure 2.6 represents $\bar{k}$ as a function of the RVE size for CC, SF and IF. The standard deviation is very high at the beginning when the RVE size is less than 8 μm; then, as the RVE size increases, the standard deviation decreases progressively until it becomes two orders of magnitude less than the mean permeability. This is due to the fact that, the bigger the area considered for the homogenisation is and the more it is representative of the porous media behaviour. On the other hand, a large area can increase dramatically the computational cost of the simulations. The best trade-off between accuracy and simulation time is identified by the optimal RVE size. In each anatomical area, we found the RVE critical value as the point that satisfies two requirements:

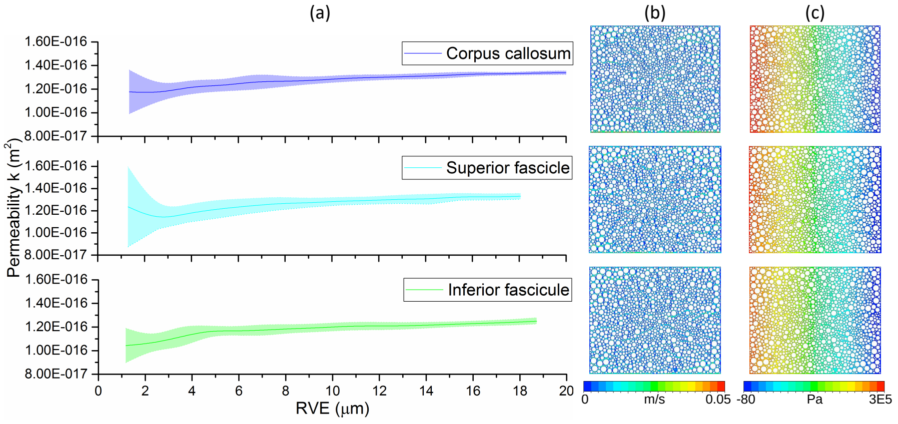

FIGURE 2.6: The hydraulic permeability (a) in the CC, SF and IF is represented as a function of the RVE size along with the respective velocity (b) and pressure contours (c).

TABLE 2.1: RVE size and average hydraulic permeability in CC, SF and IF.

	CC	SF	IF
RVE (μm)	17.5	16.8	15.2
$\bar{k}$ (m^2)	$1.33 \cdot 10^{-16}$	$1.32 \cdot 10^{-16}$	$1.22 \cdot 10^{-16}$

the average permeability is constant and the standard deviation becomes a small fraction of the average value. It is worth noticing that the minimum standard deviation is about 2% of the permeability, thus confirming that 6 geometries for each ADD provide a sufficient level of accuracy. The results are summarised in Table 2.1.

Furthermore, Figure 2.6 shows examples of velocity and pressure contours for each ADD. In each geometry the flow paths as well as the maximum velocity are very similar since the average ECS width, which drives the convective flux in CC, SF and IF, is comparable. Moreover, the pressure field decrease linearly along the porous media with an overall pressure drop of about 30000 Pa.

2.3.4 Comparison with previous studies

In the literature there exist a few studies concerning hydraulic permeability in human tissues, which report a wide range of values. Table 2.2 lists three of the major experimental papers where the authors used different types of tissue (Netti et al., 2000; Swabb, Wei, and Gullino, 1974; Franceschini et al., 2006). The obtained results vary significantly and cover a range of three orders of magnitude. This suggests a strong correlation between permeability and histological features. Our results are well within the experimental range.

TABLE 2.2: Experimental studies on hydraulic permeability with several types of tissues.

Tissue Type	Permeability (m^2)	Researchers
Hepatic neoplastic tissue *in vitro*	$3.1 \cdot 10^{-17}$	Swabb, Wei, and Gullino, 1974
Hepatic neoplastic tissue *in vivo*	$(2.9 - 8.4) \cdot 10^{-18}$	Swabb, Wei, and Gullino, 1974
MCaIV murine mammary carcinoma	$1.86 \cdot 10^{-15}$	Netti et al., 2000
LS174T human colon adenocarcinoma	$3.37 \cdot 10^{-16}$	Netti et al., 2000
U87 human glioblastoma	$4.87 \cdot 10^{-16}$	Netti et al., 2000
HSTS 26T human soft tissue sarcoma	$6.9 \cdot 10^{-17}$	Netti et al., 2000
Human brain tissue	$2.47 \cdot 10^{-17}$	Franceschini et al., 2006

2.4 Discussion

The relevant literature concerning fibrous porous media has seen many attempts to describe the hydraulic permeability of unidirectional fibres; the models can be roughly divided in ordered and disordered where the analytical or numerical approach has been followed respectively. In the former category, an analytical relationship between hydraulic permeability and porosity can be established according to the fibres packing (triangular, square, hexagonal) as described by Gebart, 1992 and Tamayol and Bahrami, 2009. On the contrary, in the second category, computational methods have been used to understand how permeability is influenced by other geometrical factors such as the mean nearest inter-fibres distance and the degree of disorder (Chen and Papathanasiou, 2007; Chen and Papathanasiou, 2008; Hitti, Feghali, and Bernacki, 2016). Although the contributions of the researches cited above are valuable and underline the importance of the geometry on the overall behaviour of the porous media, they use a population of fibres with the same diameter which is not the case of the WM as explained in subsection 2.2.1. Therefore, the presence of a geometry which is able to mimic the main geometrical characteristics of the WM is fundamental to model effectively the flow through the axons. In subsection 2.3.1, we demonstrated how we achieved this task implementing a model geometry in which the main histological features of the WM are considered. Indeed, the ECS volume fraction covers 87% of the physiological range. Moreover, the ECS width is in very good agreement with the experimental data presented in the literature, also considering the inter-species variability, since they analysed murine brain, and the differences between grey and WM (Nicholson, Kamali-Zare, and Tao, 2011; Ohno et al., 2007; Nicholson and Hrabětová, 2017; Syková and Nicholson, 2008).

Furthermore, we exploited Ripley's function to inquire the spatial organisation as depicted in Figure 2.4. Although a comprehensive analyses that covers the entire parameter space is out of the scope of this work, the randomness analysis performed on either the experimental images and our model shows a behaviour which is ascribable to CSR. Moreover, assessing the spatial organisation of a porous media and ensuring that it is homogeneous along all the length scale considered is fundamental in all the studies that aim to estimate the correct size of an RVE (Hitti, Feghali, and Bernacki, 2016).

The sensitivity analysis conducted on the grid resolution allowed us to obtain accurate results as well as a feasible computational times for a challenging geometry.

The permeability of each ADD was computed on RVEs of increasing size. The results illustrated in Figure 2.6 and Table 2.1 show outcomes concerning both the RVE critical size and the permeability values which were similar in the cases examined. This is probably due to the fact that, even if we are considering three different anatomical structures, their ADD as well as the ECS width are very similar, thus producing a comparable effect on the fluid flow as suggested also by Chen and Papathanasiou, 2008 in their discussion on the mean nearest inter-fibres distance. On the other hand, comparing our results with data presented in literature has proven to be a more difficult task since a very small amount of experiments have been conducted. The work which is closest to our study is that performed by Franceschini et al., 2006, who computed a permeability value which is slightly lower than ours. However, it must be noticed that there are four important differences to take into account. Firstly, there is an inter-species variability, as suggested by Abbott, 2004, since we are analysing a monkey brain instead of a human one. A second factor to consider is that the permeability is not a direct measure but it is inferred from a model which is based on simplifying hypotheses and, for example, does not consider non-circular axons and deviation from collinear bundles, which would both contribute to lower the permeability of the tissue. Third, the results obtained by Franceschini et al., 2006 are an average between brain samples excised in both grey and WM whereas we limit our study to WM. Finally, the average ECS volume ratio in the brain is about 0.2 (Syková and Nicholson, 2008), whereas we used the maximum value of 0.3 for the reasons explained in subsection 2.2.5. Since the ECS volume fraction is directly related to permeability, this contributes to the lower value obtained by Franceschini et al., 2006.

Nevertheless, our results are in good agreement with the experimental data if compared to the range of values presented in the literature and represent the first attempt to estimate the permeability with a numerical approach which starts from the WM microstructure. The method presented in the present contribution opens the possibility to further extend the study incorporating more images belonging to normal or pathological subjects, thus allowing to create a specific database for the permeability of brain tissue matter.

2.5 Conclusion

We presented a novel method to assess hydraulic permeability, starting from the ADD of three WM anatomical structures. Moreover, we paid particular attention to estimate the RVE size to ensure the reliability of the results obtained. The approach consisted of the following three steps: (i) Generation of a random geometry in which the cross-sectional area of the neurons is considered circular. The algorithm created a fibres assembly according to the experimental ADD of CC, SF and IF, offering also the possibility to vary the ECS volume fraction covering almost all the physiological range. (ii) Implementation of a CFD model by means of the finite element solver ANSYS to compute the velocity and pressure fields experienced by our model WM. Furthermore, we conducted a grid-sensitivity analysis to ensure high accuracy. (iii) Finally, we used this data to compute the hydraulic permeability on different RVEs in order to determine its size.

We found that the RVE size and the hydraulic permeability are slightly different for each anatomical structure suggesting that an RVE characterised by a length scale of about $17\mu m$ can be representative of the overall behaviour. Moreover, the permeability values that we found are consistent with the results provided by experimental data available in the literature. Albeit based on simplifying assumptions, we believe that this work is the first important step towards a combined experimental and computational approach which aims to shed light on fundamental constitutive parameters to model brain matter. Extensions to three-dimensional domains, consideration of irregular axonal geometries and osmotic pressure, contribution of glial cells and a parametric study on the effect of the ECS volume ratio will constitute the subject of further studies.

Acknowledgments

We kindly thank Prof. Dr. Almut Schüz (Max Planck Institute for Biological Cybernetics - Tübingen) for providing the TEM images dataset.
Daniele Dini would like to acknowledge the support received from the EPSRC under the Established Career Fellowship Grant No. EP/N025954/1.

Appendix A

In subsection 2.2.2, we explained that the the algorithm to create a brain-like geometry is mainly comprised of two phases. In the first phase, the fibres are randomly arranged respecting a prescribed ADD, the minimum ECS volume ratio reachable in this phase is about 0.22. In the second phase, whose objective is to minimise the ECS volume ratio, the empty spaces are filled with other fibres whose diameter is comprised in the range of the ADD. Since the axons with a small diameter are more likely to find room between the others, the ADD is more skewed towards them with respect to the original one. That results in a median diameter which goes from the 0.34 μm of the original ADD to the 0.3 μm of the skewed ADD. To quantify the effect of this limitation on the permeability calculation, we created a geometry respecting the ADD of the CC. Then, applying the shrinking method described in subsection 2.2.2, we reached the desired ECS volume ratio equal to 0.3.

We computed the permeability on an RVE of 17.5 μm as suggested by the results reported in subsection 2.3.3 obtaining a final value equal to $1.4 \cdot 10^{-16}$ m^2 which is 5% higher than the one presented in Table 2.1. In conclusion, our generation algorithm, on the one hand introduces a very small error, on the other hand allows analysing almost all the physiological range of ECS volume fraction. We believe that the increased flexibility obtained by the proposed algorithm and its fidelity in reproducing realistic ECS volume fractions greatly overcomes the potential error introduced in the computation of permeability and therefore, we considered this limitation acceptable.

Appendix B

In the attempt of filling a volume or an area with solid particles, a common issue usually rises in the proximity of the walls. Indeed, here, the particles find it harder to pack together, with respect of the inner zones of the porous media, because of the presence of the walls. Therefore, the free space volume fraction increases; for an analytical description of this phenomenon the reader can refer to the work by Nield and Bejan, 2013.

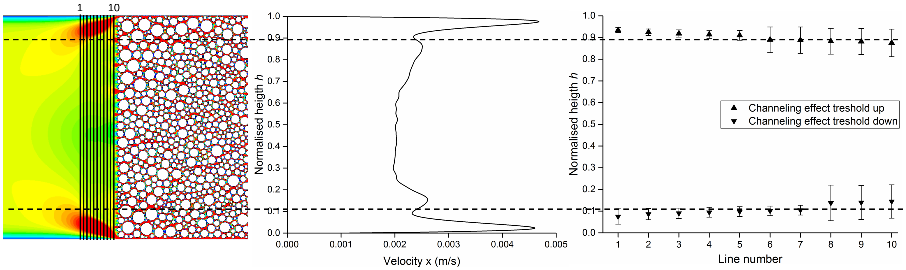

(a) (b) (c)

FIGURE 2.7: (a) Velocity contour before the porous media, the *channelling effect* is clearly visible near the walls. The black lines indicate the direction along which the velocity profiles have been extracted; (b) Average velocity profile for the CC, even in this case the sudden increase in the velocity profile points out the beginning of the *channelling effect* zone; (c) Its exact starting points have been determined averaging the position of the first and last local minima between the 6 random geometries of the CC.

As it is easy to imagine, the volume fraction increase brings, as a consequence, the augmentation of the volume of fluid flowing near the walls as well as the average velocity, and this is evident in Figure 2.7a. Since this phenomenon, which is known as *channelling effect* (Nield and Bejan, 2013), affects the permeability computation, we designed a method to infer and exclude the areas involved.

In each geometry, we extracted the velocity profile along 10 lines in the proximity of the porous zone as indicated in Figure 2.7a. The threshold of the *channelling effect* zone can be identified by the anomalous and sudden increase in the velocity profile highlighted in Figure 2.7b. Mathematically, this operation means finding the position of the first and last local minima along the normalised height of the channel h. Finally, Figure 2.7c depicts the position of the upper and lower threshold averaged between the 6 geometries created for the CC. Equivalent results (not shown in this paper) emerged for the other anatomical structures.

Accordingly, the porous media areas corresponding to 10% of the channel height at both ends (top and bottom in Figure 2.7a of the computational domain) were excluded from the hydraulic permeability computation.

2.6 Introduction

Patients affected by glioblastoma, which is the most common malignant tumor, suffer from a poor prognosis. Despite surgery, chemotherapy and radiation are aggressive techniques, the median survival time does not exceed 2 years (Crawford, Rosch, and Putnam, 2016; Mehta et al., 2015). In this clinical scenario, convection enhanced delivery (CED) has shown encouraging results because it allows to overcome the blood-brain barrier (BBB) which is a major obstacle in reaching the parenchyma with therapeutics (Debinski and Tatter, 2009; Jahangiri et al., 2016). Indeed, in CED, a pharmaceutical agent is injected directly into the brain by means of a catheter which is linked to an external pump that provides a defined flow rate. The ability to predict, in the operative phase, the distribution of the drug inside the tumor is one of the most important factors affecting CED efficacy as suggested in (Raghavan et al., 2006; Raghavan, Brady, and Sampson, 2016). Therefore, several numerical models aiming to predict the efficacy of this treatment and the penetration of the drug have been developed in the last twenty years (Ehlers and Wagner, 2015; Kim et al., 2012; Linninger et al., 2008a). However, they are still affected by unsatisfactory predictive capabilities. One of the reasons for the lack of success in producing definitive answers and simulation tools for this problem is that most of the constitutive parameters involved vary significantly from one study to another. Indeed, the brain has proved to be a challenging medium to be studied because of the extreme difficulty to conduct either experimental campaigns or numerical studies (Nicholson and Hrabětová, 2017). One of the most important parameters affecting CED outcomes is tortuosity which mainly depends on the extracellular space (ECS) geometry (Nicholson and Hrabětová, 2017; Tao, Tao, and Nicholson, 2005; Syková and Nicholson, 2008; Hrabe, Hrabětová, and Segeth, 2004). Although the ECS plays a fundamental role in determining the CED performance, its characteristics are still largely unknown, especially since its width is quantified in the tens of nanometers. Several studies (Syková and Nicholson, 2008; Hrabe, Hrabětová, and Segeth, 2004; Tao and Nicholson, 2004; Hrabětová and Nicholson, 2004) have determined that the ECS occupies about 20% of the brain volume; the ECS is composed by narrow spaces between the cells of the central nervous system, which form an interconnected system of channels demarcated by cellular membranes. The gap between each membrane is filled with a fluid, whose characteristics resemble the cerebrospinal fluid, and the extracellular matrix consisting of proteoglycans, hyaluronan and other proteins (Nicholson and Hrabětová, 2017; Tao, Tao, and Nicholson, 2005; Syková and Nicholson, 2008; Hrabe, Hrabětová, and Segeth, 2004; Tao and Nicholson, 2004; Hrabětová and Nicholson, 2004). Although different important steps forward have been made in this area, linking the microscopic properties of the ECS to macroscopic parameters remains challenging (Hrabe, Hrabětová, and Segeth, 2004). Tortuosity, which expresses the geometrical complexity of the ECS, is defined as

$$\lambda = \sqrt{\frac{D}{D^*}} \tag{2.11}$$

where D is the free diffusion coefficient determined in water or a very dilute gel and D^* is the effective diffusion coefficient due to the hindrance of the ECS. Two different approaches have been developed to determine the tortuosity. The experimental approach, that may be conducted ex vivo or in vivo, exploits molecules with a hydrodynamic diameter much smaller than the gap between cells, which are used as a probe to infer the ECS characteristics. Tortuosity values range from 1.44 to 3.50 depending on the animal used, the probe molecules and the physio-pathological conditions, as evidenced by the detailed studies reported in (Nicholson and Hrabětová, 2017; Syková and Nicholson, 2008; Nicholson, Kamali-Zare, and Tao, 2011). A value of about $\lambda = 1.6$ has been assigned to normal brain in physiological condition. The second approach consists in the creation of geometrical models which undergo Monte Carlo simulations (Hrabe, Hrabětová, and Segeth, 2004; Tao and Nicholson, 2004; Hrabětová and Nicholson, 2004). The first set of simulations reported in (Hrabe, Hrabětová, and Segeth, 2004; Tao and Nicholson, 2004) have shown that a maximum value of $\lambda = 1.225$ can be attained by modelling the system as an assembly of regularly spaced convex cells (cubes and other objects); this value is remarkably lower than the values extracted from experiments. To fill the gap between experiments and simulations, Tao, Tao, and Nicholson, 2005; Hrabětová and Nicholson, 2004 have hypothesized the presence of dead-space microdomains that hinder the molecules diffusion.

This approach produced results that are much closer to the experiments, but its geometry is based on cubes with cavities of different shapes and the authors could only speculate on the morphological basis for these assumptions. Therefore, this paper aims to shed light on tortuosity focusing, on the relationship with the ECS geometry. To do that, we propose a new geometry model for white matter with realistic features and that is able to match experimental data. Moreover, to the best of our knowledge, this is the first attempt to differentiate between gray and white matter.

2.7 Materials and methods

2.7.1 Dataset

In this work, we used the axon diameter distribution (ADD) of the corpus callosum of a monkey which was provided by (Liewald et al., 2014). The authors used the measured inner diameter of myelinated axons and the average width of the myelin sheath to construct a realistic model.

2.7.2 Geometry creation

The geometry was created using an ad-hoc algorithm within the Matlab program (Mathworks, Nantick, MA). The main idea was to create a geometry that could resemble closely the white matter microstructure. Therefore, we modeled the axons as straight cylinders parallel to each other with a circular cross section according to the ADD and the myelin sheath width (Abolfathi et al., 2009). Moreover, ECS volume ratio and ECS width were made to vary within physiological values (Syková and Nicholson, 2008). The algorithm to generate the geometry was based on the advancing front approach described in (Feng, Han, and Owen, 2003) but, instead of having tangential circles, we imposed the minimum distance between each of them to be the ECS width, as shown Fig. 2.8 (a). Moreover, to keep the ECS volume fraction in the physiological range, we implemented a complementary algorithm which, respecting the ADD and ECS width constraints, adds a new circle in each void space which is suitable, as depicted in Fig. 2.8 (b). This second part exploited the skeletonization algorithm described in (Haralick and Shapiro, 1992); indeed the skeleton branch points represent the location where the distance between close circles is maximized. Finally, the circles were extruded to form 3D cylinders whose length was designed according to the specification suggested in (Tao and Nicholson, 2004); the result of the generation of the three-dimensional domain used for the numerical models reported in the next sub-section is shown in Fig. 2.8 (c). We created five 3D geometries whose geometrical features are summarized in Table 2.3.

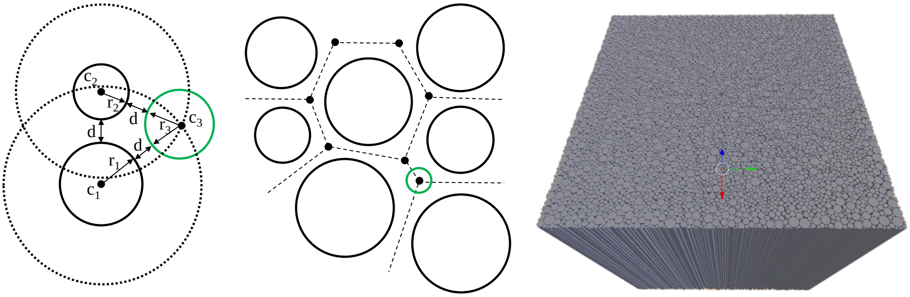

(a) (b) (c)

FIGURE 2.8: Circles generation algorithm: (a) given two circles with radius r_1 and r_2 and centered at c_1 and c_2 respectively, the center c_3 of the new circle (green) with radius r_3 is given by one of the two intersections of the dotted circles with radius $r_1 + r_3 + d$ and $r_1 + r_3 + d$ centered at c_1 and c_2 respectively; (b) in the second part of the algorithm, new circles are added at the skeleton branchpoints (black dot) if they respect the ADD and the ECS width; (c) each circle is extruded in a straight cylinder to produce the final three-dimensional geometry.

2.7.3 Numerical modeling

The numerical simulation were conducted using the software MCell (Stiles and Bartol, 2001; Stiles et al., 1996; Kerr et al., 2008) which allows measuring the effective diffusion coefficient and tortuosity reproducing the experimental point-source paradigm (Nicholson and Hrabětová, 2017). In each simulation, 5000 molecules were released in the center of the volume and let free to diffuse. We did not include any chemical reaction between molecules and axons membrane since we were only interested in the effect that geometry has on

TABLE 2.3: Main features of the brain geometries created.

ECS width (nm)	ECS Volume ratio	Number of axons	Dimension (μm)
5	0.18	7490	60.6 x 60.6 x 62.6
20	0.21	7204	60.5 x 60.5 x 62.5
40	0.25	6934	62.1 x 62.1 x 64.1
60	0.27	6754	63.4 x 63.4 x 65.4
80	0.32	6868	65.7 x 65.7 x 67.7

tortuosity. Therefore, each collision was modelled as perfectly elastic (Hrabe, Hrabětová, and Segeth, 2004). We set a free diffusion coefficient $D = 10^{-7}$ cm^2/s with a time step $\Delta t = 1$ μs for a total simulation time of 10 seconds. These parameters resulted in a mean linear step length:

$$L_{mean} = 2\sqrt{\frac{D\Delta t}{\pi}} \tag{2.12}$$

which is about six times smaller than the minimum space between axons. In this way, each molecule executed several Monte Carlo steps between consecutive interactions with axon surfaces (Tao, Tao, and Nicholson, 2005). The sampling box approach originally developed by Tao and Nicholson, 2004, was used in the generalized version provided by Hrabe, Hrabětová, and Segeth, 2004 to take into account the anisotropic shape of our geometry. In this second method, each concentric box is defined by three dimensions a_x, a_y and a_z along each principal axis; however, since we want to compute the effective diffusion along each axis separately, we let two out of three dimensions become much larger so that the domain can be considered to be infinitely large along those axes. This allows us to examine the behavior of the system in the third remaining direction (e.g. to compute the effective diffusion along the x axis, with both a_y and $a_z \to \infty$). In this way, we set 8 sampling boxes along each principal direction. Being transparent at the molecules passage, their only function is to count the number of molecules inside them as a function of time. The number of molecules n in each box is described by the following equation:

$$n(t) = n_0 erf(\frac{a_x}{4\sqrt{D_x^*}} erf(\frac{a_y}{4\sqrt{D_y^*}} erf(\frac{a_z}{4\sqrt{D_z^*}}) \quad (2.13)$$

where n_0 is the initial number of molecules, t is the time and D_x^*, D_y^*, D_z^* are the effective diffusion coefficients along the principal directions. Equation 2.13 was used to fit the simulation data by means of a Matlab based nonlinear fitting algorithm thus estimating D^* for each box. The final value of D_x^*, D_y^*, D_z^* and so λ_x, λ_y, λ_z was obtained averaging the results of each box along the principal axes.

2.8 Results

The geometry was designed to be axisymmetric with respect to two principal directions: the first runs parallel to the axons and the second is perpendicular to them. We verified this statement comparing the results obtained along the x and the y axis which showed negligible differences. Fig. 2.9 gives a graphical idea of the axisymmetric behavior of the system: in Fig. 2.9 (a) the molecules spread radially in a uniform way whereas in Fig. 2.9 (b), the molecules move preferentially in the z direction. Therefore, only the results obtained along the x and z axes, namely the radial and longitudinal directions, will be shown. In Fig. 2.10, it is possible to notice that λ_z (longitudinal tortuosity) is constant and equal to 1. This behavior was expected because the axons are parallel to each other and so they do not offer any obstacles to the diffusion of molecules along this direction. In other words, the longitudinal component of the random displacement performed during the simulation is never affected. In contrast, λ_x (radial tortuosity) is always higher than 1 because the axons geometry hinders the molecules movement. Furthermore, Fig. 2.10 shows that λ_x is inversely proportional to both ECS volume ratio and ECS width, meaning that the effective diffusion varies from 29 to 54% of the free diffusion. Finally, Fig. 2.10 compares λ_x with the convex cell model presented in (Tao and Nicholson, 2004) and experimental data of similar brain structures reported in (Syková and Nicholson, 2008).

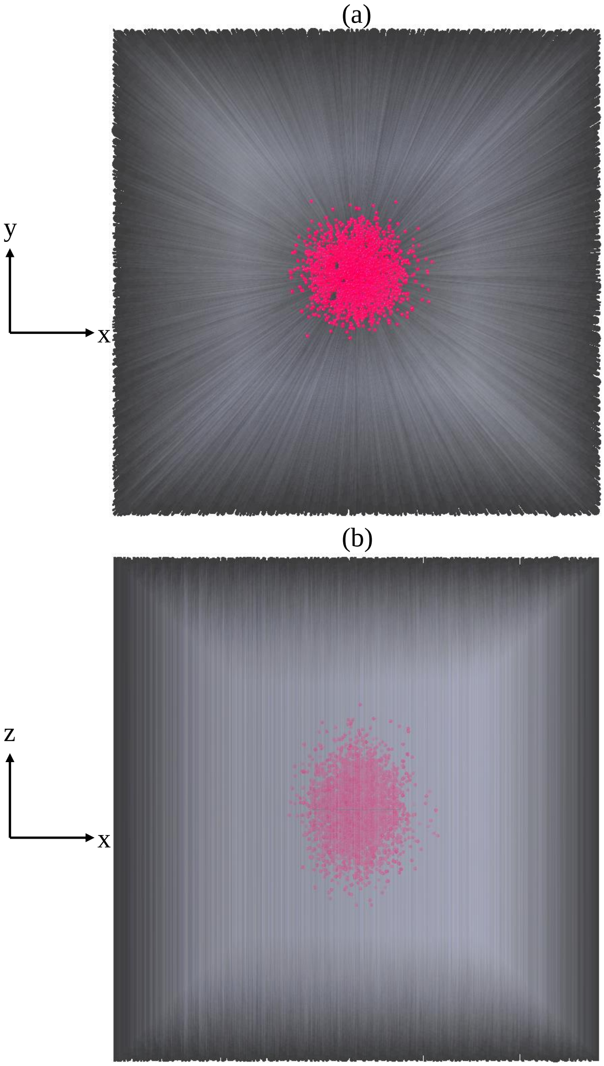

FIGURE 2.9: (a) Top view and (b) frontal view of one of the five volumes studied in our simulations, showing the diffusing molecules after 1.8 seconds. The anisotropic behavior of the system is highlighted by the ellipsoidal shape of the molecules cloud in (b).

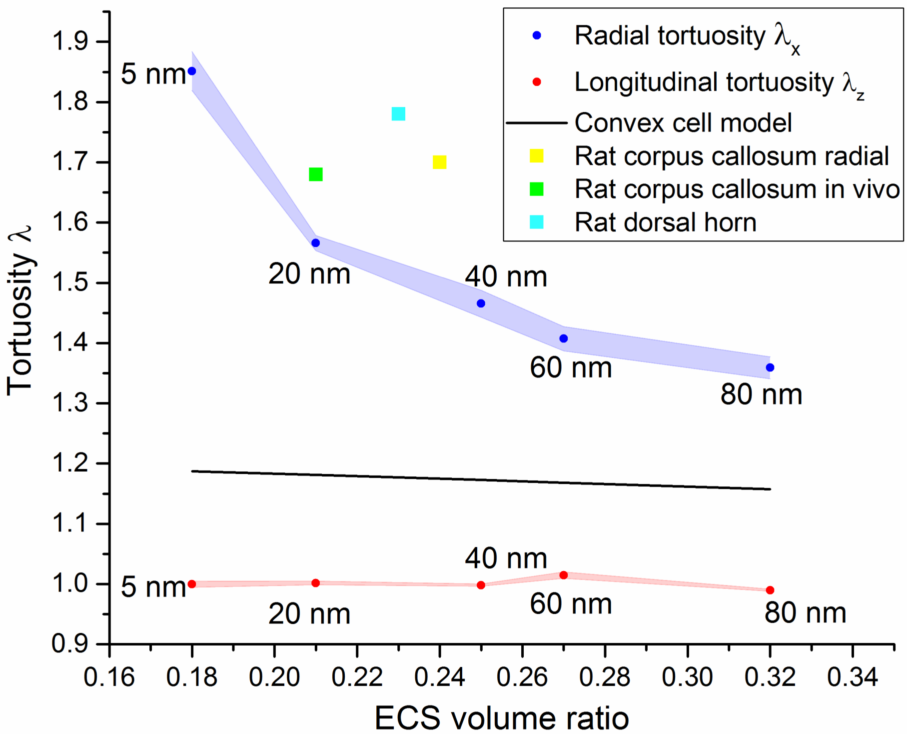

FIGURE 2.10: Radial tortuosity (blue) and longitudinal tortuosity (red) obtained with our simulations. The radial tortuosity decreases as both the ECS volume fraction and the ECS width increase. In contrast, the longitudinal tortuosity is constant and equal to 1. The radial tortuosity is compared with the convex cell model (black) (Syková and Nicholson, 2008), and experimental data obtained on different rat white matter fibre tracts (Hrabětová and Nicholson, 2004).

2.9 Discussion

The simulation of physiological models can follow two main approaches: finite element method (FEM) or Monte Carlo (Schutter, 2009). Both methods have advantages and drawbacks, but whereas in the first the accuracy is guaranteed by the solution convergence, in the second, this passage is not straightforward. Therefore, in Monte Carlo simulation, it is fundamental to assess the accuracy comparing numerical and theoretical results. In our model, the soundness of the method is proved by λ_z which is equal to 1 in all the simulations with a negligible standard deviation (Fig. 2.10). This result is in complete agreement with what was expected theoretically since the geometry was designed to offer no resistance in the longitudinal direction. Moreover, the results depicted in Fig. 2.9 show that the geometrical anisotropy has a fundamental role in determining the molecules diffusion path. Since it has been demonstrated that the white matter is highly anisotropic (Syková and Nicholson, 2008), this factor should be taken into account to shed light on the diffusion process mechanism. Existing models (Tao, Tao, and Nicholson, 2005; Hrabětová and Nicholson, 2004) have attempted to find a specific correlation between a certain geometrical feature, namely ECS volume fraction and dead-space microdomains, and the outcomes in term of tortuosity. However, it has been hard to find a morphological justification for the existence of the dead-space microdomains. In contrast with this, the geometrical model proposed in this paper matches most of the main histological white matter characteristics in terms of ADD, ECS volume ratio and width. The latter could have a prevalent responsibility as suggested by the results showed in Fig. 2.10. Indeed, the circular axonal cross sections facilitates the formation of bottlenecks followed by large cavities. While the bottlenecks provide a very small passage for the molecules to freely move across the matter, the cavities may be described as pockets (Tao, Tao, and Nicholson, 2005) or lakes (Chen and Nicholson, 2000) where the molecules remain trapped. Finally, in Fig. 2.10, it is possible to note that the model produces a trend of λ_x that correlates well with the experimental values extrapolated from results obtained from similar brain regions either in vivo or ex vivo. This suggests that our geometry has succeeded in including the main parameters responsible for this behavior. It should be noted that there is not a perfect agreement between the simulation and the experimental data. This could be easily explained by the fact that we aimed to understand the role of the geometry whereas the experimental tortuosity is a composite parameter, which depends on other factors such as extracellular matrix and hydrodynamic diameter of the diffusing molecules (Nicholson and Hrabětová, 2017). Nevertheless, understanding the relationship between geometry and tortuosity is fundamental to integrate this parameter with imaging techniques such as diffusion tensor imaging, used in CED interventions, which provides statistical information on the microstructure.

2.10 Conclusion

We presented a new model that incorporates the main geometrical features of the white matter. The model cannot be considered exhaustive since some assumptions had to be made to simplify the geometry along the z axis. Therefore, future improvements will incorporate characteristics concerning the longitudinal axonal development, such as curvature and cross-sectional area variation. Nevertheless, our model outcomes are in good agreement with the experimental data and represent a significant improvement with respect to previous works, whose failure to accurately predict tortuosity is probably due to their attempt to describe the whole brain. This suggests that a zone-wise approach which differentiates at least between white and gray matter could be more reliable in inferring the diffusion properties which are essential to determine the evolution of many biological and drug delivery process.

Acknowledgments

We kindly thank Dr. Almut Schüz (Max Planck Institute for Biological Cybernetics) for providing the images dataset.

This project has received funding from the European Union's EU Research and Innovation programme Horizon 2020 under grant agreement No 688279.

Chapter 3

White matter permeability: an electron microscopy imaging based study

In this chapter, we present an ideal workflow that starts with the processing of electron microscopy images and finishes with the white matter permeability computation by means of numerical simulations.

In the first part of the chapter*, we present an automatic, accurate and fast method for axon segmentation in electron microscopy images based on fully convolutional neural network. The method allows the computation of important geometrical parameters such as the axon diameter distribution, through axon architecture analysis. The segmentation is performed using a residual fully convolutional neural network inspired by UNet and Resnet. The fully convolutional neural network training is performed exploiting mini-batch gradient descent and the Adam optimizer. The Dice coefficient is chosen as loss function. The proposed segmentation method achieves results comparable with already existing methods for axon segmentation in terms of Information Theoretic Scoring (98%) with a faster training (5 hours on the deployed GPU) and without requiring heavy post-processing (testing time is 0.2 seconds with a non-optimized code). Moreover, the axon diameter distributions computed from the segmented and ground-truth images are statistically equivalent.

In the second part of the chapter**, we move towards a more realistic estimate of the white matter permeability by analysing two areas (corpus callosum and fornix) whose three-dimensional microstructure is reconstructed starting from the acquisition of electron microscopy images. As expected, the white matter structure is mainly composed of elongated and parallel axons. Using a principal component analysis, we define two principal directions, parallel and perpendicular with respect to the axons main direction and we compute the permeability along them. The results demonstrate a statistically significant difference between parallel and perpendicular permeability thus proving the anisotropic behaviour of the white matter. Moreover, we show that the permeability in corpus callosum and fornix is statistically different which suggests that the white matter is also an heterogeneous porous medium.

Note that, as stated in the Introduction Chapter, the algorithm developed in the first part is not used for the axons segmentation. This is due to the presence of some errors that, despite being negligible for extracting the axon diameter distribution, have a great impact on the permeability computation. Therefore, to avoid any unwanted effect, we prefer performing a manual segmentation.

*This work has been published as: Vidotto, M., De Momi, E., Gazzara, M., Mattos, LS., Ferrigno, G., & Moccia, S. (2019). "FCNN-based axon segmentation for convection-enhanced delivery optimization", *International Journal for Computer Assisted Radiology and Surgery*, 14(3):493-499.

**This work will be submitted as: Vidotto, M., De Momi, E., & Dini, D. (2020). "White matter microstructure role for hydraulic permeability: a new electron microscopy images based approach", *Proceedings of the National Academy of Sciences*.

Note for the reader: the sections of the second part of the chapter are ordered in an unconventional fashion as demanded by the journal where this article will be submitted.

3.1 Introduction

Gliomas are the most common brain tumors ($\approx 40\%$ of brain tumors (Buckner et al., 2007)) and glioblastoma multiforme (GBM) is the most common and malignant one, accounting for 51% of gliomas (Kanu et al., 2009).

Nowadays, GBM treatment is one of the most challenging tasks in clinical oncology. Despite the variety of modern therapies, GBM is still a deadly disease with extremely poor prognosis and median survival of 15 months from diagnosis (Thakkar et al., 2014). The three main therapeutic approaches are surgical resection, radiation therapy and chemotherapy Hanif et al., 2017. A high grade of GBM infiltration does not allow complete surgical resection and thus relapses occur (Iacob and Dinca, 2009). Several risk factors and restrictions are associated with radiation therapy, including radiation necrosis, permanent radiation-induced neuronal damage and radio-resistance (Hanif et al., 2017). The biggest limitation in chemotherapeutic treatment is related to the blood-brain-barrier (BBB), which limits the spreading of the most common chemotherapeutic agents (Jovčevska, Kočevar, and Komel, 2013).

An alternative treatment procedure, called convection enhanced delivery (CED), has shown encouraging results in the last years (Raghavan et al., 2006). In CED, a pharmacological agent is injected directly into the brain tissue by means of a catheter positioned in the target cancerous region, through a hole in the scalp. Drug spreading is driven by both a positive pressure and a diffusion gradient, allowing CED to overcome the main problems related to BBB (Bobo et al., 1994; Debinski and Tatter, 2009; Jahangiri et al., 2016).

Despite the encouraging results, it is widely accepted in the clinical literature that CED outcome is still suboptimal due to two main problems. The first is related to the choice of the optimal catheter design and the infusate backflow (White et al., 2011; Barua et al., 2016). The second deals with leakages within the substrate at the point of delivery and limited drug distribution (Barua et al., 2013; Raghavan, Brady, and Sampson, 2016). This paper specifically focuses on the second problem.

Drug distribution is controlled by drug infusion parameters, such as flow rate and infusion duration (Varenika et al., 2008; Raghavan et al., 2006). A way to optimize the infusion parameters for CED planning is to implement, in the pre-operative phase, numerical models able to predict the drug distribution within the brain (Raghavan and Brady, 2011; Ehlers and Wagner, 2015). However, despite the fact that several studies have been conducted in the field, a satisfying level of planning has not been achieved yet. Ehlers and Wagner, 2015 suggested that this could be due to a lack of consensus on model-parameter values (in particular for hydraulic permeability and effective diffusivity).

Since the drug flows through interstitial pathways between neurons, taking into account the brain micro-structure is essential to infer the physical properties that drive both the convective and diffusive flux (Goriely et al., 2015). Brain micro-structure can be retrieved exploiting electron microscopy (EM), which guarantees high resolution at neuron scale (Knott and Genoud, 2013; Titze and Genoud, 2016). For example, in (Vidotto et al., 2018) and (Vidotto, Dini, and De Momi, 2018), two different methodologies, inspired by consolidated work in the literature (Nicholson and Hrabětová, 2017; Dias et al., 2012), are proposed to compute the brain hydraulic permeability and the effective diffusivity starting from the axon diameter distribution (ADD) (Liewald et al., 2014) computed from axon manual segmentation in EM images.

In this scenario, the goal of this work was to develop an automatic and accurate method for axon segmentation in EM images with the goal to automatically retrieving reliable ADDs. Following recent advancements in the literature, the proposed segmentation algorithm was based on deep fully-convolutional neural networks (FCNNs) and, in particular, on deep-residual learning networks (Resnets) (He et al., 2016). The evaluation was performed in terms of:

- Axon-segmentation performance on the ISBI2012 challenge dataset defined in (Arganda-Carreras et al., 2015)
- Comparison of the ADD obtained from the FCNN-based and the ground-truth axon segmentation.

The paper is organized as follows: Sec. 3.3 surveys axon segmentation strategies, with a focus on deep learning. Sec. 3.4 explains the proposed approach to axon segmentation in EM images and ADD computation from the segmented images. Sec. 3.5 deals with the experimental protocol used to test the proposed methodology. Results are presented in Sec. 3.6 and discussed in Sec. 3.7. Finally, strength and limitations of this work are reported in Sec. 3.8.

3.2 Materials and methods

3.3 State of the art

In the last decades, axon segmentation in EM images was mainly based on image filtering and thresholding (Mishchenko, 2009), and mathematical morphology (More et al., 2011).

More recently, with the spreading of high-computational-power computers and publicly-available large and labeled datasets[1], machine learning methods became the most common approach to axon segmentation. One of the first attempts at using machine learning for axon segmentation was proposed in Andres et al., 2008. A hierarchical segmentation procedure based on random forest (RF) and watershed segmentation was proposed for 3D segmentation of neural tissues in scanning EM volume data from rat retina. Similarly, RF was exploited in (Kaynig, Fuchs, and Buhmann, 2010) and its probabilistic output was used in combination with axon geometrical properties to define a regular cost function that enforced gap completion via perceptual grouping constraints. A similar approach was used in (Laptev et al., 2012), where dense correspondence across sections was exploited to resolve ambiguities in neuronal segmentation.

During the last years, deep learning, a subfield of machine learning based on deep neural networks (DNN), drew the attention of researchers in the field (Litjens et al., 2017). First examples include (Jurrus et al., 2010) and (Liu et al., 2012), where deep artificial neural networks were used. For example, in (Turaga et al., 2010) graph-theory was adopted and a convolutional neural network (CNN) was used to infer graph weights. In (Ciresan et al., 2012) a CNN was used to directly obtain axon segmentation. The network had four convolutional layers, each one followed by a max pooling layer. A similar

---

[1] (`http://brainiac2.mit.edu/isbi_challenge/home`)

approach was exploited also in (Fakhry, Peng, and Ji, 2016) and in (Tschopp et al., 2016). All the three approaches performed segmentation via pixel classification, using two fully connected layers at the end of the convolutional path.

A further innovation was introduced with the use of FCNNs. In a FCNN, the fully connected layers are replaced by up-convolutional layers, allowing a faster and more precise axon localization with respect to approaches based on fully-connected-layer classification (Moccia et al., 2018; Litjens et al., 2017). In (Ronneberger, Fischer, and Brox, 2015) a FCNN, which is known as U-Net due to its u-shaped architecture, was proposed outperforming all the previous approaches.

Starting from the U-Net implementation, architectural improvements often dealt with multilevel analysis (to encode image information at multiple scale) and introduction of residual blocks (to tackle the vanishing gradient problem) (Quan, Hildebrand, and Jeong, 2016; Xiao et al., 2018). In most of these approaches, remarkable performances were achieved at the cost of heavy time-consuming post-processing (e.g. based on superpixel and watershed segmentation for global refinement).

For our task, while post-processing may heavily prolong the overall computational time (i.e. the time for axon segmentation, ADD computation, and computation of the optimal CED infusion parameters with numerical models), methodologies based on residual blocks may be suitable for achieving a reasonable segmentation performance for computing ADDs from EM images.

3.4 Methods

3.4.1 Architecture description

As introduced in Sec. 3.1, the proposed FCNN architecture was inspired by U-Net (Ronneberger, Fischer, and Brox, 2015) and Resnet (He et al., 2016). As (Ronneberger, Fischer, and Brox, 2015), the proposed FCNN consisted of a convolutional and an up-convolutional path. A schematic figure of the exploited FCNN architecture is shown in Fig. 3.1.

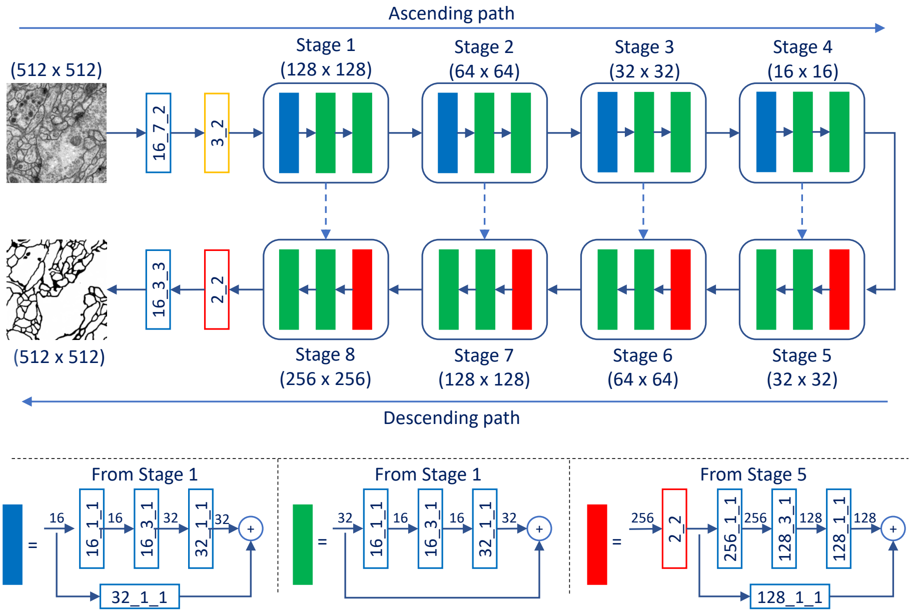

FIGURE 3.1: Top: Scheme of the fully-convolutional neural network exploited in this work. There are four stages forming the descending path and four stages forming the ascending path. Each stage of the descending path is made of a convolutional block (full blue boxes) and two identity blocks (full green boxes), whereas in the ascending path the convolutional block is substituted by an upconvolutional block (full red boxes). We used the annotation introduced in Xiao et al., 2018, the empty blue boxes indicate convolutional layers (C_N_S) with channels C, kernel size $N \times N$ and stride S; the empty yellow box (N_S) indicates a maxpooling over $N \times N$ patches with stride S; the empty red boxes denote upsampling operation (K_K) with size K. Each convolutional operation is followed by batch normalization and a $ReLU$ activation function. The dotted arrows refer to the concatenation of the feature map from the descending to the ascending path. Bottom: The convolutional and identity blocks of Stage 1, and the upconvolutional block of Stage 5 are shown. On the top of arrows, the number of feature maps is reported.

The proposed FCNN started with convolutions performed with 16 (7×7) filters followed by batch normalization, activation with the rectified linear unit and 2×2 pooling.

After this initial processing, in the convolutional path a first convolutional block was present with three convolutional kernels in cascade and a shortcut connection with 1×1 convolution for dimensional matching. The convolutional block was followed by two identity blocks made of three convolutional kernels and an identity skip connection. This structure (one convolutional block and two identity blocks) was repeated four times, doubling the number of convolutional kernels per layer. The up-convolutional path was symmetric to the convolutional one, but with up-convolutional blocks instead (thus halving the number of kernels per layer). All convolutions and up-convolutions were performed with 3×3 kernels. Batch normalization and activation with the rectified linear unit were applied after each convolution.

The proposed FCNN ended with a bare full convolution with two 3×3 kernels activated with a sigmoid function.

3.4.2 Training

Adam optimizer (Kingma and Ba, 2014) was used to train the proposed FCNN. Adam exploited the first moment estimate ($\hat{m_t}$) and the second moment estimate ($\hat{v_t}$) of the loss-function gradient to update the network parameters:

$$\theta_{t+1,i} = \theta_{t,i} - \frac{\eta}{\sqrt{\hat{v_t}(g_{t,i})} + \epsilon} \cdot \hat{m_t}(g_{t,i}) \tag{3.1}$$

where $\theta_{t+1,i}$ denotes the i-th parameter after $t+1$ mini-batches, $g_{t,i}$ is the gradient with respect to the parameter θ_i after t mini-batches and ϵ is a small number. The cost function we adopted was the Dice similarity coefficient.

3.5 Experimental protocol

The dataset used to test the segmentation performance was released for the ISBI2012 challenge[2]. The training dataset is composed by 30 sections from

---

[2] (`http://brainiac2.mit.edu/isbi_challenge/home`)

the ventral nerve cord of a first-instar Drosophila larva acquired using serial section transmission EM. The 30 sections are 512×512 grayscale images. The ground-truth segmentation is composed by 512×512 binary images, where the axons membranes are labeled in black and the background is labeled in white. The ISBI2012 challenge organizers provided also another set of 30 (512 x 512) grayscale images (for which the ground truth was not publicly available) for testing purposes.

As suggested in (Ronneberger, Fischer, and Brox, 2015) and in (Fakhry, Peng, and Ji, 2016), data augmentation was performed. Seven linear transformations (rotations of $0°$, $30°$, $45°$, $60°$ and $90°$, vertical and horizontal mirroring) and eleven non-linear transformations (barrel transform, sinusoidal transform and shearing) were applied. The augmented dataset consisted of $8 \times 11 \times 30 = 2310$ training images.

The training and testing images were padded (symmetric padding) to compensate the pixel loss due to the convolution operations. This was the only manipulation we performed on the images during segmentation.

Adam optimizer parameters were set as suggested in (Kingma and Ba, 2014). We train the proposed FCNN with a batch size of 16 on 100 training epochs and initial learning rate of 10^{-3}. The 40% of the training images was used as validation set.

We performed all our experiments on Google Colaboratory[3].

To evaluate the segmentation performance of the proposed FCNN, we used the metrics suggested by the challenge organizer[4]

- **Foreground-restricted Rand Scoring (V^{Rand}):**

$$V^{Rand} = \frac{\sum_{ij} p_{ij}^2}{\alpha \sum_k s_k^2 + (1-\alpha) \sum_k t_k^2} \tag{3.2}$$

  where p_{ij} is the probability that a randomly chosen pixel belongs to a segment i (defined as a set of connected pixels) in the predicted segmentation S and segment j in the ground-truth segmentation T, $s_i = \sum_j p_{ij}$ and $t_j = \sum_i p_{ij}$ are the probability that a randomly chosen

---

[3] https://colab.research.google.com/

[4] (`http://brainiac2.mit.edu/isbi_challenge/evaluation`)

pixel belongs to segment i in S and j in T respectively and $\alpha = 0.5$ is the Rand F-score which weights split and merge errors equally.

- **Information Theoretic Scoring (V^{Info}):**

$$V^{Info} = \frac{I(S;T)}{(1-\alpha)H(S) + \alpha H(T)} \tag{3.3}$$

where $I(S;T) = \sum_{ij} p_{ij} log(p_{ij}) - \sum_i s_i log(s_i) - \sum_j t_j log(t_j)$ is a measure of the similarity between S and T and $H(S) = -\sum_i s_i log(s_i)$ is the entropy.

The segmentation evaluation was performed through an automated online system where the segmented images were compared with the relative (hidden) ground-truth (Fakhry, Peng, and Ji, 2016).

We compared the FCNN performances with those achieved by the best competitors in the literature among those that used the ISBI dataset for testing purposes, as to perform a fair comparison. In particular, we considered the FCNNs implemented in (Xiao et al., 2018; Quan, Hildebrand, and Jeong, 2016; Beier et al., 2017).

As introduced in Sec. 3.1, we compared the ADDs computed from the images segmented with the FCNN with those computed from the ground-truth images (ADD was computed as in (Liewald et al., 2014)). As the ground-truth for the testing images of the ISBI dataset was not available, we divided the original training dataset in a subset for re-training from scratch the FCNN (20 images) and a set for computing the ADD (10 images). Both subsets underwent data augmentation (seven linear transformations and eleven non-linear transformations). The Wilcoxon rank-signed test (significance level = 0.05) was used to assess whether statistical differences existed between the ADDs computed from the FCNN-based segmentation and from the ground-truth.

3.6 Results

No significant differences were found when comparing the ADDs computed from the images segmented with the FCNN and the relevant ground truth

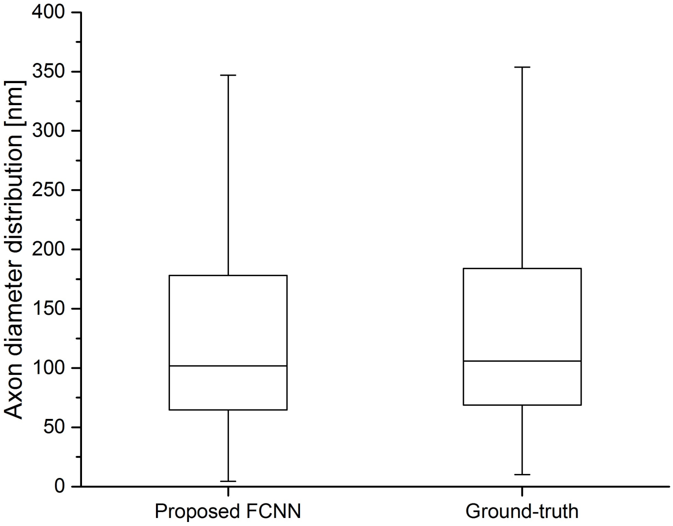

FIGURE 3.2: Comparison between the axon diameter distributions extracted from the segmented and the ground-truth images.

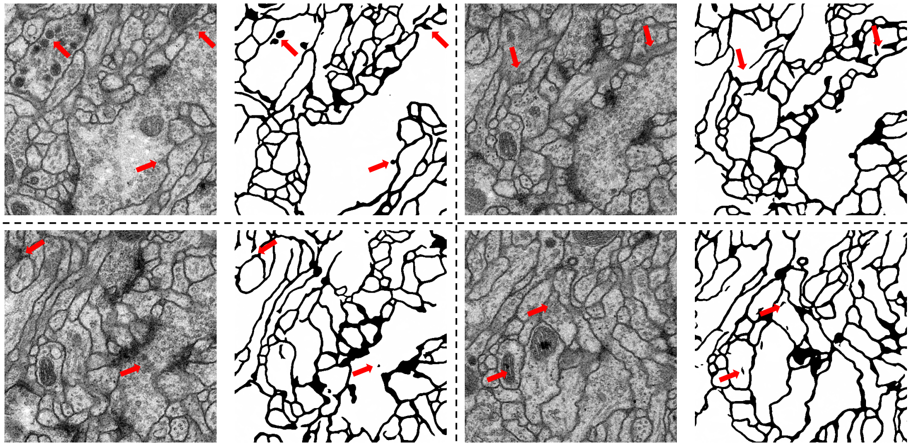

FIGURE 3.3: Sample segmentation results obtained with the proposed FCNN. Raw testing images and output probability maps are compared. Red arrows on input images and output segmentation maps indicate structures that were incorrectly segmented.

TABLE 3.1: V_{Rand}, V_{Info} and training time for the proposed and the competitor approaches. The V_{Rand}, V_{Info} are computed on the testing set using the best FCNN model over the 100 training epochs.

Model	V_{Rand}	V_{Info}	Training time
Ref. Xiao et al., 2018	0.9835	0.9906	36 hours
Ref. Beier et al., 2017	0.9826	0.9894	20 hours
Ref. Quan, Hildebrand, and Jeong, 2016	0.9805	0.9881	-
Proposed	0.9419	0.9768	5 hours

(these results were obtained with a $V_{info} = 0.96$). The ADDs are shown in the boxplots in Fig. 3.2.

In Table 3.1, the V_{Rand} and V_{Info} obtained for the proposed FCNN and for the competing approaches are reported. Training time is reported, too.

The proposed FCNN architecture had a lower training time (5 hours) with respect to the competitors at the cost of a slightly lower performance (V_{Rand} = 0.941987271 and V_{Info} = 0.976824393). The computational time required to segment one image was 0.2 s with a non-optimized code. A direct comparison with the competitors was not possible though, as the relevant testing time was not reported.

Sample testing EM images and segmentation results after Otsu's thresholding, that we performed for visualization purpose only, are shown in Fig. 3.3.

3.7 Discussion

From Fig. 3.2, the achieved ADD was comparable (no statically significant difference were found) with that obtained with time-expensive manual tracing, thus indicating that the achieved segmentation performance was appropriate for our purposes. This was possible even if some errors were present in the segmentation, mainly due to thick axon borders and to small-organelle profiles within big axons (Fig. 3.3). False positive in correspondence of mitochondrial structures were detected, too. Errors were mainly related to intensity drops, noise in the images and limited number of samples against the high data variability.

In Table 3.1, it is possible to notice that the proposed FCNN achieved performances comparable with the competing approaches in terms of V_{Rand} and V_{Info} (the values were $4.1 \cdot 10^{-2}$ and $1.3 \cdot 10^{-2}$ lower, respectively, than those for (Xiao et al., 2018), which achieved the best performances).

The time required for training our FCNN was significantly lower with respect to all the other competitor methods (about four times lower with respect to (Beier et al., 2017) and seven times lower with respect to (Xiao et al., 2018)). Furthermore, even if the testing times are not reported by the competitors, they performed heavy post-processing that sharply increases the segmentation computational cost. On the contrary, our approach, without any post-processing, obtained good results as supported by the absence of significant difference between the ADDs extracted from the ground-truth and the proposed FCNN (Fig. 3.2).

A limitation of this work can be seen in the fact that our experimental protocol dealt with axons of Drosophila larva, instead of human ones. Nonetheless, while neuronal global architecture and axons diameter vary across different species, the axon microstructure (i.e., the round-shaped cross-section) is very similar (Zaimi et al., 2018).

With the goal of integrating this work into a full framework for reliable and robust fluid-dynamics brain-model implementation for CED, the FCNN performance should be tested on datasets of human-brain images. In fact, this work is part of the European project EDEN2020 (www.eden2020.eu), which supports the collections of such datasets, that, to the best of authors' knowledge, are currently not available. This could be attributed to the fact that high-resolution EM is a time consuming procedure. Images with lower resolution could be collected in a faster way (thus achieving a larger datasets and granting higher variability) but these images would probably be more challenging to segment. However, despite this still having to be experimentally tested, we expect that, with a proper training dataset, performance suitable for geometrical-parameter estimation can be still achieved. In fact, there is already evidence in other fields that proper segmentation performance may be achieved also when processing low-resolution images (e.g. (Cai et al., 2017)).

3.8 Conclusions

In this work, a method for accurate FCNN-based axon segmentation and ADD computation was proposed. The method was inspired by recent advancements in deep learning and integrated FCNNs and residual nets allowing good results in terms of axon geometrical-parameter extraction without the need of heavy post-processing (no statistically significant difference was found between the ADDs computed from the ground truth and proposed FCNN).

It is acknowledged that further research is required to ameliorate the proposed algorithm but the results presented in this work are surely a promising step toward CED optimization by means of brain micro-structure analysis.

Acknowledgments

This work has received funding from the European Union's Horizon 2020 research and innovation programme under grant agreement No 688279.

3.9 Introduction

Understanding the effect of the brain microstructure on spatial drug distribution is pivotal to design effective treatment strategies for neurological disorders (Vendel, Rottschäfer, and Lange, 2019).

The recent introduction of an innovative technique called Convection-Enhanced Delivery (CED) in the neurosurgical scenario opened up the possibility to deliver chemotherapeutic agents to brain tumours and, more recently, gene therapy for Parkinson's disease and antiseizure agents for epilepsy (Debinski and Tatter, 2009; Christine et al., 2019; Rogawski, 2009). In CED, the main idea is to use convection to augment the local concentration of a drug by directly infusing in the brain tissue (Crawford, Rosch, and Putnam, 2016). Usually, one or more catheters are stereotactically placed in the region of interest and then anchored to a pump that can inject a drug at certain flow rate, which is usually in the order of $\mu l/min$ (Jahangiri et al., 2016). Using CED, it is possible to achieve a much higher spatial distribution of the drug because the pressure gradient allows infusing over a larger volume with respect to other methods (Crawford, Rosch, and Putnam, 2016).

Despite CED has shown promising results in the field of neurological drug delivery, clinical trials did not succeed in demonstrating benefit in terms of life expectancy for patients (Crawford, Rosch, and Putnam, 2016; Jahangiri et al., 2016; Kunwar et al., 2010). Indeed, for CED to be effective, it is necessary to have a sufficiently high concentration of drug in the regions occupied by the diseased tissue. However, a number of factors such as catheter design, catheter placement and infusion protocol, which are often very difficult to control, influence the drug distribution and concentration profile. Accordingly, clinicians would significantly benefit from making use of numerical models able to predict the drug distribution and concentration in the preoperative phase (Crawford, Rosch, and Putnam, 2016; Jahangiri et al., 2016). A predictive model allows the surgeon to test different scenarios in terms of catheter setup and infusion settings in the preoperative phase to decide the best way to operate on the patient.

Although several models devoted to tackle the above scenario have been developed in the last 20 years (Ehlers and Wagner, 2015; Raghavan and Brady, 2011; Kim et al., 2012; Støverud et al., 2011; Dai et al., 2016), there are still important discrepancies between prediction and reality, thus suggesting the need for more refined and comprehensive approaches (Vendel, Rottschäfer, and Lange, 2019). In particular, the brain extracellular space (ECS) spatial organisation is identified as a pivotal factor for drug transport as highlighted by Nicholson and Hrabětová, 2017. However, there exists only a limited number of studies which have tried to understand the relation between ECS and hydraulic permeability, a fundamental parameter for modelling CED, which is also the subject of an important controversy (Holter et al., 2017; Vidotto et al., 2019a).

Recent advance in imaging and 3D reconstruction of brain structures at the cellular level have laid the first milestone towards a deeper understanding of the ECS spatial organisation role. For example, Holter et al., 2017 used the neuropil reconstruction (grey matter) by Kinney et al., 2013 to compare advective and diffusive transport within the interstitial space.

In this work, we use the dataset obtained using focused ion beam scanning electron microscopy (FIB-SEM) to provide 2D and 3D tissue microstructural information, as provided by Bernardini et al., N.D., to examine the permeability of two white matter (WM) structures, corpus callosum (CC) and fornix (FO). By integrating the information acquired simulating a convective flow between the axons and the principal component analysis (PCA) performed on the axons' centerline, we determine and, in doing so, confirm the ability to predict the strongly anisotropic character of the WM in terms of hydraulic permeability. Moreover, comparing the two WM structures, we reveal the significant difference between different WM areas. The relations between ECS and WM anisotropy and heterogeneity are here systematically discussed for the first time and represent an important contribution not only for CED modelling but also for understanding the interstitial solute transport.

3.10 Results

This study was conducted starting from the dataset provided by Bernardini et al., N.D., who reconstructed the 3D volume of brain areas by means of FIB-SEM. This method offers some advantages with respect to other electron microscopy techniques, the most important being the capability of scanning an entire volume by sequentially ablating layers of the specimen. This feature is especially important when dealing with WM, whose strongly anisotropic geometrical organisation is well known (Duval, Stikov, and Cohen-Adad, 2016). Indeed, it allows avoiding issues related to the registration of consecutive images in order to obtain an accurate 3D reconstruction.

Figure 3.4 briefly outlines the main steps of this work. In Figure 3.4A, two different cuts are shown: the coronal cut exposes the CC whereas the sagittal cut exposes the FO. A sample from each anatomical area was harvested, fixed, stained and imaged with the FIB-SEM (Figure 3.4B) as described in Bernardini et al., N.D.. From each volume, we selected 20 equally spaced slices (10 parallel to the xy plane and 10 parallel to the xz plane Figure 3.4B), where we manually segmented the axons boundary. Indeed, although automatic segmentation methods have shown incredible performances for the morphometry of WM structures, these are usually employed to image the intracellular space rather than the ECS (Abdollahzadeh et al., 2019; Zaimi et al., 2018; Vidotto et al., 2019b). In these scenarios, small errors may not play a major role in the accuracy of the reconstruction of the domain of interest. On the contrary, since in this study we focus on the relation between ECS and permeability, we preferred to perform a manual segmentation thus avoiding unrealistic intersections of close axons, which are extremely important for the exact determination of flow, as suggested also in (Kinney et al., 2013).

Finally, an example section from the CC parallel to the xy plane is shown in Figure 3.4C with a detail of the discretised surface. As described in *Methods*, the resulting mesh, that contains more than 600,000 elements, is the result of a sensitivity analysis. Note that, each slice has an ECS volume fraction of about 30%, which is within the physiological range (Syková and Nicholson, 2008) (Table 3.2).

TABLE 3.2: Average ECS volume fraction and standard deviation for the xy plane and the xz plane of CC and FO.

WM region	xy plane	xz plane
CC	0.31 ± 0.019	0.33 ± 0.022
FO	0.27 ± 0.049	0.28 ± 0.038

3.10.1 Flow and pressure

The velocity and pressure fields were computed by solving the Navier-Stokes equations with ANSYS Fluent (ANSYS, Lebanon, NH). The boundary conditions were chosen according to the literature on CED (Vidotto et al., 2019a): we imposed a velocity of 0.0025 m/s at the inlet and a pressure of 0 Pa at the outlet, modelling the axons as impermeable and rigid bodies (Holter et al., 2017). Note that, since the brain is usually considered an hyperelastic tissue, the last assumption is valid only with very low flow rate because the deformations, caused by the applied pressure, can be considered negligible (Kim et al., 2012; Dai et al., 2016).

Figure 3.5 shows the results of the numerical analysis conducted on the 2D slices extracted from CC and FO. Looking at the velocity profile, CC and FO show similar results with a maximum velocity around 0.07 m/s (Figure 3.5 A and E). Moreover, we can detect some of the features found in the topological analysis on a rat CA1 hippocampal neuropil performed by Kinney et al., 2013, where the authors divided the ECS into tunnels and sheets. The first are formed at the junction of three or more cells and have a 40 - 80 nm diameter, whereas the second can be found between pairs of cells with a width of 10 - 40 nm. Despite the brain samples being taken from WM areas and not neuropil, we can still recognise a similar topological organisation which has an impact on on the velocity profile. Indeed, the velocity increases, especially, in the sheets between axons, as it is possible to recognise in the streamlines depicted in Figure 3.5 B and F.

On the other hand, Figures 3.5 C and G show that the pressure decreases from inlet to outlet as the flux encounters greater local pressure loss due to the tortuous geometry of the ECS. Moreover, comparing the pressure loss across

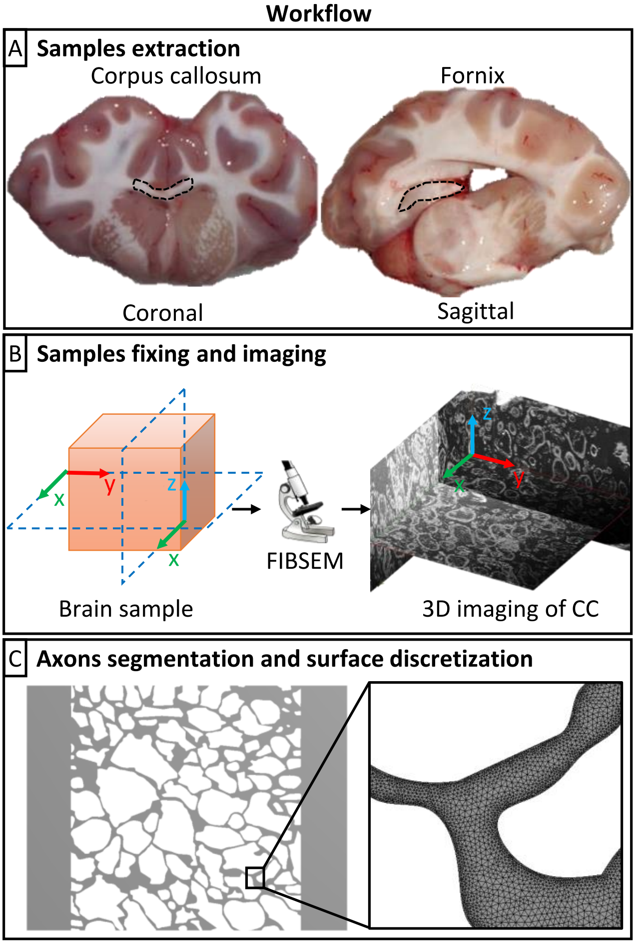

FIGURE 3.4: Workflow outline A) A coronal and a sagittal cut were performed on a sheep brain. These cuts exhibit two WM regions, CC and FO, from which two samples were harvested (as highlighted by the dashed black contour). B) The WM samples were fixed, stained and imaged by means of a FIB-SEM with a resolution of 0.02 $\mu m/px$ as detailed in (Bernardini et al., N.D.) C) The 3D volumes of CC and FO were divided in 20 equally spaced slices (10 parallel to the xy plane and 10 parallel to the xz plane) where the axons boundaries were manually selected. A detail of the triangular discretisation performed on each slice (about 300000 elements) can be appreciated in the inset exploded in the right part of the figure.

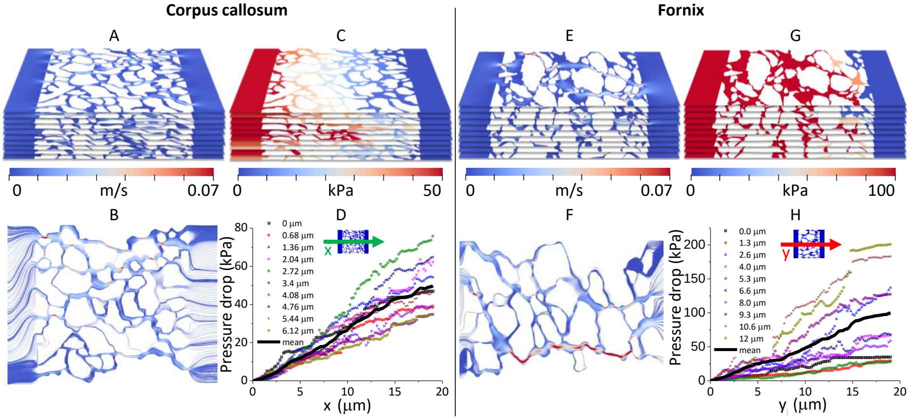

FIGURE 3.5: These results have been obtained applying a velocity of 0.0025 m/s at the inlet and a pressure of 0 Pa at the outlet as boundary conditions. A) Contour of the x component of the velocity in the CC. B) Velocity streamlines computed on a cross-section of the CC at depth equal to 3.4 μm. C) Pressure contours on the xy planes of the CC. D) Pressure drop along the x direction on each slice of the CC. The black line indicates the mean value that increases linearly ($R^2 \approx 0.99$) from 0 to 50 kPa. E) Contour of the y component of the velocity in the FO. F) Velocity streamlines computed on a cross-section of the FO at depth equal to 8 μm. G) Pressure contours on the xy planes of the FO. H) Pressure drop along the y direction on each slice of the FO. The black line indicates the mean value that increases linearly ($R^2 \approx 0.99$) from 0 to 100 kPa.

CC and FO, we notice that in the FO the pressure required to allow a convective flux is about twice that required in the CC. This could be due to the greater presence of axons with a larger equivalent diameter in the FO with respect to the CC. Indeed, this kind of axons are expected to offer higher resistance to the flux with respect to the smaller ones. Despite this difference, in both CC and FO the pressure drop increases linearly ($R^2 \approx 0.99$) along the length of the samples as shown in Figures 3.5 D and H. The black line represents the average pressure drop along the x and y axes for CC and FO, respectively.

Similar results, not displayed here for the sake of brevity, were found also in the other planes.

3.10.2 Parallel and perpendicular directions

As outlined in the introduction, the main aim of this manuscript is to show how the strongly anisotropic geometry of the WM influences a fundamental parameter for drug delivery, namely hydraulic permeability. Using Darcy's law, which assumes a linear relationship between the pressure loss across a porous material and the average velocity through the pores (Jin, Smith, and Verkman, 2016; Hitti, Feghali, and Bernacki, 2016), we computed the permeability tensor $\mathbf{k}$ with respect to the FIB-SEM imaging reference frame xyz. However, since xyz is randomly oriented, these preliminary results need to be rotated in order to be expressed with respect to the WM principal directions. Indeed, the WM can be considered as a transversely isotropic porous medium defined by a principal direction parallel to the axons and a perpendicular plane in which the material's behaviour is direction-independent (Vidotto, Dini, and De Momi, 2018; Kim et al., 2012; Dai et al., 2016). Therefore, we can summarise our objective in the definition of the parallel permeability ($k_{||}$) and the perpendicular permeability ($k_{\perp}$).

To compute these parameters in our brain samples, first we performed a PCA on the axons' centerline (Bernardini et al., N.D.; Abdi and Williams, 2010) and, by averaging the first component of the PCA of each axon, we identify the overall parallel direction Z (Fig. 3.6A). Then, randomly choosing two of the infinite vectors orthogonal to Z, we define the XYZ reference frame, where X and Y represent the directions perpendicular to the axons. Figure 3.6A is an example showing the CC but the same operation was performed also on the FO. Indeed, as can be inferred from Figure 3.6B, CC and FO exhibit a different orientation of the parallel and perpendicular directions with respect to the imaging reference frame xyz.

Then, using the Euler angles, it was possible to express the permeability tensor with respect to the XYZ reference frame thus obtaining $\mathbf{k^{XYZ}}$ and, consequently, k_X, k_Y and k_Z (Fig. 3.6C). Finally, $k_{||}$ coincides with k_Z whereas $k_{\perp}$ is obtained averaging k_X and k_Y. Details of the computation are reported in the *Methods* section.

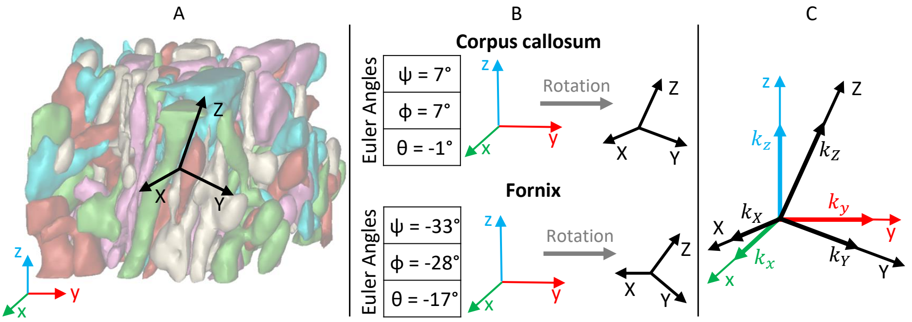

FIGURE 3.6: A) Three-dimensional volume of the CC reconstructed by Bernardini et al., N.D. with respect to the FIBSEM imaging reference frame xyz. On the contrary, since the WM geometrical organisation is strongly anisotropic, the XYZ reference frame (in black) is defined according to the WM principal directions: the Z axis is parallel to the axons whereas X and Y are two vectors chosen randomly to form a right-handed coordinate system. B) The Euler angles ψ, ϕ and θ, which express the intrinsic rotation about the x, y and z axes, respectively, describe the orientation of the XYZ reference frame with respect to the xyz reference frame. C) Both the xyz and the XYZ reference frames are centred in the origin: k_x, k_y and k_z are the x, y and z components of the permeability tensor $\mathbf{k}$. The latter is then expressed with respect to the XYZ reference frame by means of the Euler angles. As a consequence, k_X k_Y and k_Z are given by the sum of the contribution of the k_x, k_y and k_z vectors along the X, Y and Z axes, respectively.

3.10.3 Permeability

For the CC, $k_{\|}$ is comprised between 1,046 and 2,249 nm^2 with a median value of 1,710 nm^2. The results obtained along the same direction but for the FO are considerably lower with a median value of 907 nm^2 and ranging from 429 to 1,777 nm^2.

On the other hand, looking at the perpendicular direction, in the CC $k_{\perp}$ is equal to 794, 525 and 1,049 nm^2 for the median, minimum and maximum values respectively. Even in the perpendicular direction, the FO exhibits permeability values lower than CC: the median of $k_{\perp}$ is about 432 nm^2 and values range between 210 and 716 nm^2. We analysed these results by looking at two aspects: the first is related to the WM anisotropy that we expect to influence the hydraulic permeability, whereas the second aims at understanding if also the anatomical area from which the samples have been harvested plays an important role.

To this end, since the Shapiro-Wilk tests on $k_{||}$ and $k_{\perp}$ rejected normality for both CC and FO ($p < 0.10^{-3}$), we conducted a statistical analysis using the Mann-Whitney rank-sum test for unpaired samples.

The analysis results are summarised in Figure 3.7. In both geometries, the comparison between $k_{||}$ and $k_{\perp}$ shows a statically significant difference ($p = 2.46 \cdot 10^{-4}$ for CC and $p = 0.0028$ for FO). This outcome strongly suggests that the anisotropic geometrical organisation of the WM has an impact on the flow across the tissue which ultimately leads to different values of permeability. It also interesting to note that the ratio between the median value of $k_{||}$ and $k_{\perp}$ is comparable in the two WM samples analysed: 2.15 in the CC and 2.09 in the FO.

Moreover, we inspect the WM by comparing the permeability values in the same direction obtained in the CC and FO samples. Also in this case the Mann-Whitney rank-sum test was used. As shown in Figure 3.7, for both $k_{||}$ and $k_{\perp}$, there is statistically significant difference between the two samples ($p = 0.0022$ for $k_{||}$ and $p = 0.0028$ for $k_{\perp}$). This result clearly represents a measure of the heterogeneity of the WM in different regions of the brain.

3.11 Discussion

Most of the research efforts of the last 20 years to address the need for tool to predict the drug distribution profile in the brain, were conducted by implementing more and more complex mathematical models (Ehlers and Wagner, 2015; Støverud et al., 2011; Kim et al., 2012; Raghavan and Brady, 2011; Dai et al., 2016). However, despite previous cited investigations represent extremely valuable contributions, they still do not guarantee a sufficient level of accuracy because of the large uncertainty on most of the constitutive parameters. Indeed, as pointed out by Nicholson and Hrabětová, 2017, the ECS is still a largely unknown territory made of narrow intercellular channels which form very tortuous paths.

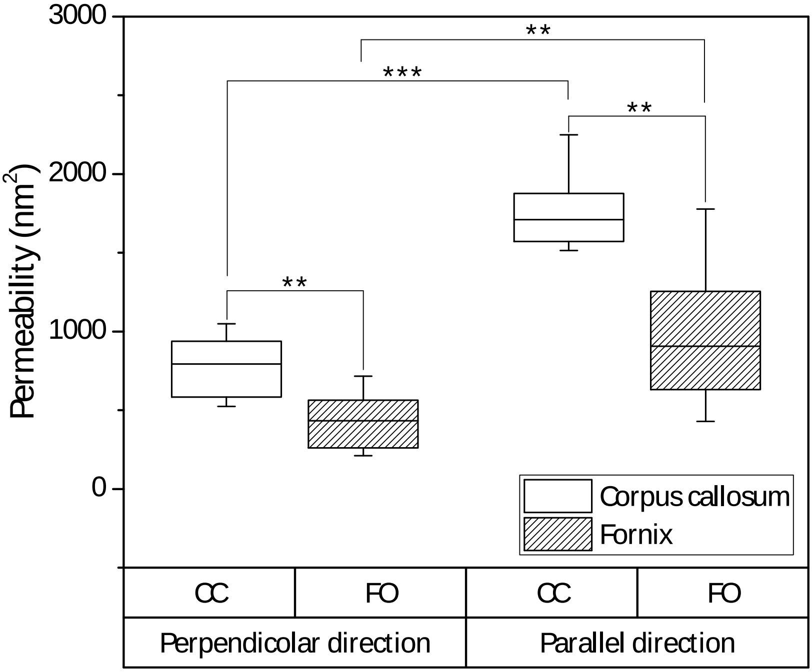

FIGURE 3.7: The boxplot shows a comparison between permeability evaluated on CC and FO taking into account the WM anisotropy and the anatomical area from which they were harvested. The statistical analysis, conducted with the Mann-Whitney rank-sum test for unpaired samples demonstrates that there is an strong statistical difference between $k_{||}$ and $k_{\perp}$ in the CC ($p = 2.46 \cdot 10^{-4}$) and between $k_{||}$ and $k_{\perp}$ in the FO ($p = 0.0028$). Moreover, we find evidences of a statistically significant difference also comparing the $k_{||}$ in CC and FO ($p = 0.0022$) and the $k_{\perp}$ in CC and FO ($p = 0.0028$).

It is only recently that new microscopy imaging techniques have started to unveil the real structure of the ECS thus giving the possibility to run accurate numerical simulations (Holter et al., 2017; Kinney et al., 2013). In this manuscript, we exploit the 3D reconstruction of two WM structures from Bernardini et al., N.D., namely CC and FO, to reach three objectives: quantify the hydraulic permeability, highlight its anisotropic behaviour and show the zonal heterogeneity of its value within WM.

Quantifying the brain hydraulic permeability has always represented a very challenging problem that has been addressed following two main approaches, experimental and numerical. Just a few works have followed the experimental approach, with Franceschini et al., 2006; Tavner et al., 2016 who performed their experiments on human and lamb brain tissue respectively, whereas Netti et al., 2000 used cerebral neoplastic tissue.

TABLE 3.3: Comparison of permeability values from the literature. E and N stand for experimental and numerical approach respectively. A viscosity of $1mPa \cdot s$ was assumed when the permeability was converted from hydraulic conductance (Vidotto et al., 2019a).

Tissue Type	Permeability (nm^2)	Approach	Ref
Sheep CC $k_\perp$	794	N	This study
Sheep FO $k_\perp$	432	N	This study
Sheep CC $k_{\|\|}$	$1,710$	N	This study
Sheep FO $k_{\|\|}$	907	N	This study
Human/lamb brain	24.7	E	(Franceschini et al., 2006) (Tavner et al., 2016)
U87 human glioblastoma	487	E	(Netti et al., 2000)
$k_\perp$ from WM model	$122 - 133$	N	(Vidotto et al., 2019a)
WM human	$7,500$	N	(Basser, 1992)

The results, summarised in Table 3.3 shows that our permeability values are much higher than the one found by Franceschini et al., 2006; Tavner et al., 2016. However, in the comparison, we need to consider a fundamental difference: our research focuses specifically on WM areas whereas Franceschini et al. and Tavner et al. considered a generic brain tissue sample (with either white and grey matter and without considering the directionality in the tissue). Accordingly, their value can be only considered representative of an isotropic and homogeneous sample of the brain. Despite this issue prevents a convincing comparison, the fact that the ratio between their result and ours is roughly one order of magnitude recalls the ratio that it is usally found in the literature between grey matter (isotropic tissue) and WM (anisotropic tissue) (Basser, 1992; Linninger et al., 2008a; Støverud et al., 2011).

On the other hand, our outcomes are in the same order of magnitude of the research conducted by Netti et al., 2000. In this work, the authors first performed a series of confined compression tests on excised tissue of human glioblastoma (U87) and then they fitted the experimental data with a poroviscoelastic model. Note that, as suggested by Tavner et al., 2016, there is still an important debate on which model is the most appropriate for brain tissue. In this case, we can only speculate that the similarity between our findings is probably due to the fact that the porous structure of the U87 cell line is somehow similar to the WM, thus offering a comparable resistance to the flow.

A second approach is represented by numerical studies. Basser, 1992 developed a geometrical model based on important simplifying assumptions. The resulting permeability in the WM is probably overestimated and does not include any anisotropic property. On the contrary, Vidotto et al., 2019a implemented an idealised geometrical model of the WM in the perpendicular direction starting from the axon diameter distribution from (Liewald et al., 2014). Looking at Table 3.3, we can notice that our results in the perpendicular direction are in good agreement with their work.

From this overview, it is clear that a proper comparison with the state of the art is not possible because our work represents the first systematic and comprehensive analysis of the WM permeability considering the directionality of the axons in two WM areas. Indeed, in Figure 3.7, we show that there is a statistically significant difference between permeability in the parallel and perpendicular direction in both CC and FO. To the best of our knowledge, this research demonstrates, for the first time, the anisotropic properties of the WM starting from the reconstructed microstructure of the axonal fibres. This represents a step change with respect to magnetic resonance imaging based method, such as diffusion tensor imaging (DTI) or neurite orientation dispersion and density imaging (NODDI) (Zhang, Yang, and Jiang, 2012). Indeed, despite DTI and NODDI are fundamental tools used in the standard clinical practice, they usually have a resolution in the order of millimetres whereas the average ECS width is in tens of nanometres (Syková and Nicholson, 2008). Therefore, they can only provide macroscopic and homogenised information about the WM microstructure and, in turn, about the permeability.

Furthermore, we provide a quantitative estimate of the ratio between $k_{||}$ and $k_{\perp}$ that, in both CC and FO, is about 2. Obviously, we cannot claim that this ratio is constant across the brain but it suggests that a ratio equal to 10 or more, which is found in several CED modelling works (Kim et al., 2012; Dai et al., 2016), may be overestimated.

Also, our findings provide a clear picture of the WM heterogeneity within a single animal (Fig. 3.7). Considering both $k_{||}$ and $k_{\perp}$, there is, indeed, a statically significant difference between CC and FO. This proves that, not only the brain cannot be easily divided in grey and white matter but neither dividing the WM according to the parallel and perpendicular direction to the axons is enough. Therefore, also this aspect deserves a further in-depth analysis.

As a conclusion, we want to underline that the importance of our findings are not limited to drug delivery but may have consequences also for the controversial discussion on interstitial solute transport in the ECS (Holter et al., 2017; Asgari, De Zélicourt, and Kurtcuoglu, 2016) and for the validation of model of the micro-structure starting from the DTI analysis (Zhang, Yang, and Jiang, 2012).

3.12 Materials and Methods

3.12.1 Finite-Elements Simulations

The brain is modelled as a porous medium in which fluxes of molecules, drugs or cerebrospinal fluid take place in the interstitial space between the axons. The latter represent the solid phase of the white matter that, for very low flow rate, can be considered as a rigid material (Vidotto et al., 2019a; Kim et al., 2012; Dai et al., 2016). Accordingly, the flow is modelled by the Stokes equations Hitti, Feghali, and Bernacki, 2016:

$$\mu \Delta \mathbf{v} - \nabla p = 0 \tag{3.4}$$

$$\nabla \cdot \mathbf{v} = 0 \tag{3.5}$$

where **v** is the fluid velocity, p the pressure and μ the viscosity ($10^{-3}\ Pa \cdot s$). As boundary conditions, we imposed a velocity equal to $0.0025\ m/s$ at the inlet and $0\ Pa$ pressure at the outlet with a no slip condition on the axon walls ($\mathbf{v} = 0$) as suggested in other studies (Vidotto et al., 2019a). The resulting partial differential equations were solved in the finite element method (FEM) software ANSYS (ANSYS, Lebanon, NH) with semi-implicit method for pressure linked equations (SIMPLE). The meshes were generated using ANSYS meshing tool. Generating a mesh and running a simulation took about 60 minutes on an Intel i7-6800K processor. For both samples, we analysed 10 equally spaced slices parallel to the FIBSEM xy plane and 10 slices parallel to the xz plane (Figure 3.4B).

3.12.2 Mesh sensitivity analysis

The ECS of the WM shows a highly tortuous and intricate ramification of channels that makes the discretisation process very challenging. To ensure that the results are independent from the meshing parameters, we performed a mesh sensitivity analysis varying the elements size on the edges and the maximum face size. The mesh was refined 7 times going from 67,000 triangular elements for the baseline to 760,000 triangular elements for the finest mesh. We stopped refining the mesh when the difference between two consecutive mesh refinements in term of both average velocity and pressure drop was below 1%. Accordingly, the final mesh used to compute the flux in all the geometries has the following parameters: element size on the edges equal to $0.015\ \mu m$ and maximum face size of the triangles equal to $0.045\ \mu m$ for a total elements number around 600,000 (Figure 3.4C).

3.12.3 Permeability

The hydraulic permeability of a porous media can be computed using Darcy's law which describes the linear relation between pressure drop and velocity (Hitti, Feghali, and Bernacki, 2016; Vidotto et al., 2019a):

$$\tilde{\mathbf{v}} = \frac{\mathbf{k}}{\mu} \nabla \mathbf{p} \tag{3.6}$$

where $\mathbf{k}$ is the hydraulic permeability tensor, $\nabla\mathbf{p}$ is the gradient pressure in the direction of the flux and $\tilde{\mathbf{v}}$ is the velocity through the pores averaged on the fluid volume according to the following equation:

$$\tilde{\mathbf{v}} = \frac{1}{V}\int_{V_f} \mathbf{v} dV \tag{3.7}$$

where V and V_f are the total and fluid volume respectively (Yang, Lu, and Kim, 2014; Vidotto et al., 2019a).

Using Eq. 3.6 and Eq. 3.7, we computed the permeability values in the FIBSEM imaging reference frame (xyz) thus obtaining, for each sample, 10 values of k_{xx}, k_{yy} and k_{zz}, namely the diagonal elements of $\mathbf{k}$ (Figure 3.5). Then, to describe the WM permeabilty with respect to a more informative set of coordinates, we defined the XYZ reference frame.

To do that, we first conducted a PCA on the axons' centerline thus obtaining, for each one of them, a vector indicating the principal direction ($\mathbf{Z_i^{PCA}}$). Then, we performed a weighted average between the $\mathbf{Z_i^{PCA}}$ vectors to find the overall principal direction ($\mathbf{Z}$), using the following equation:

$$\mathbf{Z} = \frac{\sum_{i=1}^{N} L_i \cdot \mathbf{Z_i^{PCA}}}{\sum_{i=1}^{N} L_i} \tag{3.8}$$

Where N is the total number of axons and L_i is the linear length of the i^{th} axon defined as the euclidean distance from head to tail. In this way, we gave more importance to the longer axons, namely the one occupying a larger portion of the volume.

Assuming that the WM can be modelled as a transversely isotropic porous medium (Kim et al., 2012; Dai et al., 2016; Zhan, Baena, and Dini, 2019), we randomly chose the X and Y vectors to form the right-handed reference frame XYZ where Z and XY represent the directions parallel and orthogonal to the axons, respectively. The orientation of the XYZ reference frame with respect to the xyz reference frame can be described by means of the Euler angles ψ, ϕ and θ expressing the intrinsic rotation about the x, y and z axes. Then, we converted the Euler angles in the corresponding rotation matrix (R_{XYZ}^{xyz}) and we expressed the previously computed permeability tensor $\mathbf{k}$ with respect to the XYZ reference frame:

$$\mathbf{k^{XYZ}} = (R_{XYZ}^{xyz})^{-1} \cdot \begin{bmatrix} k_{xx} & 0 & 0 \\ 0 & k_{yy} & 0 \\ 0 & 0 & k_{zz} \end{bmatrix} \tag{3.9}$$

Finally, summing the X, Y and Z components of $\mathbf{k^{XYZ}}$, we computed k_X, k_Y and k_Z. Since k_X and k_Y lie on the same plane, we calculated $k_\perp$ as the mean value between them whereas $k_\|$ coincides with k_Z. Note that, all the operations listed above were conducted for both CC and FO independently.

Chapter 4

Infusion mechanisms in brain white matter and its dependence of microstructure: an experimental study of hydraulic permeability

In this chapter, we measure the permeability of white matter of fresh ovine brain tissue considering the localised heterogeneities in the medium using an infusion based experimental set up, *iPerfusion*. We measure the flow across different parts of the white matter in response to applied pressures for a sample of specific dimensions and calculate the permeability from directly measured parameters. Furthermore, we directly probe the effect of anisotropy of the tissue on permeability by considering the directionality of tissue on the obtained values. Additionally, we investigate whether white matter hydraulic permeability changes with post-mortem time. To our knowledge, this is the first report of experimental measurements of the localised white matter permeability, showing the effect of axon directionality.

This work has been submitted as: Jamal*, A., Mongelli*, MT., Vidotto, M., Madekurozwa, M., Bernardini, A., Overby, DR., De Momi, E., Rodriguez y Baena, F., Sherwood, JM., & Dini, D. (2020). "Infusion mechanisms in brain white matter and its dependence of microstructure: an experimental study of hydraulic permeability", *IEEE Transaction of Biomedical Engineering*.

*Jamal and Mongelli contributed equally to this manuscript. Jamal wrote the manuscript with support from Vidotto, Sherwood and Dini. Mongelli carried out the experiments. Vidotto, conceived and planned the experiments, designed the study and supervised the findings of this work. All authors provided critical feedback and helped shape the research, analysis and manuscript.

4.1 Introduction

Glioblastoma multiforme (GBM), a grade IV glioma, is the most aggressive and frequently diagnosed form of primary central nervous system (CNS) tumour in adults, with an average age of 64. Studies have reported an incidence of 5 per 100,000 persons and GBM leads to 250,000 deaths per year worldwide (Bush, Chang, and Berger, 2017; Alphandéry, 2018). Conventional techniques for GBM treatment, such as radiation and chemotherapy, have either severe side effects (e.g. localised tissue damage) or suffer from limitations in passing through the blood-brain barrier (BBB) and distribution of therapeutic agents throughout the tissue by passive diffusion (Harder et al., 2018; Weidle, Niewöhner, and Tiefenthaler, 2015; Yuan, 1998). Convection-Enhanced drug Delivery (CED) (Mehta et al., 2015; Lonser et al., 2015), an intra-tumoural infusion method for localised drug delivery, has emerged as a viable delivery technique and a promising solution to overcome some of the mentioned obstacles. In contrast to diffusion-based drug delivery techniques, which rely on concentration gradients to drive the flow, CED is based on infusion under a positive pressure gradient into the CNS. By utilising advective transport, CED enables relatively lower concentrations of the therapeutic agent than diffusion-based delivery methods. CED is not without limitations and its efficiency is affected by a number of factors, including target heterogeneity, white matter (WM) edema and transport parameters. Furthermore, lack of histological information of brain tissue leads to issues in determining the ratio of the drug distribution volume to the infusion volume, $R_{d/i}$ $(V_d : V_i)$ (Mehta et al., 2015; Lonser et al., 2015), which is conventionally used to assess the efficacy of CED.

For a given pressure gradient, flow through a porous tissue can be characterised by Darcy's law and the hydraulic permeability, k, which represents a geometry and viscosity corrected conductance (reciprocal of resistance to flow). However, in heterogeneous and anisotropic tissues, resistance to fluid flow is both location and direction dependent and consequently it dictates the ratio $R_{d/i}$ (Raghavan et al., 2006). Therefore, determining the hydraulic permeability of multiphase tissues is key for the development and successful implementation of intra-tumour infusion-based drug delivery therapies that rely on advective transport mechanisms (Chen and Sarntinoranont, 2007; Miranpuri et al., 2013; Raghavan and Odland, 2017). It also plays a fundamental role in determining transport of interstitial molecules (Ray, Iliff, and Heys, 2019; Syková and Nicholson, 2008), which is strongly linked to many physiological processes of the brain, including dynamics of pathological molecules that transit the extracellular matrix (ECM) (Mestre et al., 2020; Vargová and Syková, 2008; Agnati, Bjelke, and Fuxe, 1992).

In contrast to rigid porous materials, wherein k is constant, hydraulic permeability in biological materials has been reported to vary with tissue deformation that occurs due to the pressure gradient during intra-tumoural infusion (McGuire, Zaharoff, and Yuan, 2006). Hydraulic permeability also has a large dependence on pore structure topology and tissue geometry (Datta, 2006). For brain tissue, there is limited knowledge of these parameters, and a lack of reliable methodologies for their accurate determination, which makes it difficult to understand infusion mechanisms and determine the hydraulic permeability in a predictive manner.

For cerebral tissue, although theoretical models have been developed to determine hydraulic permeability, less attention has been paid to experimental studies. Furthermore, the constitutive parameters used in theoretical models vary by up to three orders of magnitude (Vidotto et al., 2019a; Tavner et al., 2016; Ehlers and Wagner, 2015; Støverud et al., 2011; Raghavan and Brady, 2011; Linninger et al., 2008a). Such a significant difference across the literature and lack of experimental evidence to complement these models makes it difficult to justify the use of specific values for predictive purposes, e.g. when they need to be used as inputs for large scale CED simulations. Furthermore, a deeper understanding of the effect of tissue microstructural features is needed to predict the local response of the system to external infusion and physiological processes; what is the effect of fibril bundle orientation on hydraulic permeability? This ought to be characterised and reproduced with the most accurate available methods.

There are a number of available techniques for estimating hydraulic permeability experimentally. These techniques include infusion, i.e. localised drug delivery to a tissue from a point source (catheter's tip) (Milosevic et al., 2008; Zhang et al., 2000; Boucher et al., 1998), perfusion, i.e. drug delivery from a source with cross sectional surface comparable to the tissue dimensions (Zhang et al., 2000; Heneghan and Riches, 2008; Reynaud and Quinn, 2006) and compression (Vunjak-Novakovic et al., 1999; Gu and Yao, 2003). Due to heterogeneity of local tissue microstructure, differences in where the sample comes from and sample size between these techniques makes it difficult to compare results and may have led to the large range of reported values.

In the case of brain tissue, only a few studies have experimentally determined hydraulic permeability, but their results are affected by the sample and experimental protocol adopted. Franceschini et al., 2006 performed an *ex vivo* uniaxial deformation experiment on human brain tissue excised within 12h of death and indirectly determined permeability from the compressibility parameters by fitting the data to Terzaghi's theory. Tavner et al., 2016, used a perfusion experiment to determine the hydraulic conductivity (which can be directly linked to permeability) of lamb and sheep brains using Darcy's law. However, both of these studies adopted large samples (30 mm/5-8 mm initial diameter/height) to study the macroscopic tissue response and did not consider the microscale localised heterogeneities in the tissue. Brain is composed of cerebrospinal fluid, grey matter and WM, and is anisotropic due to the directionality of axons in WM. Also, the perfusion based experimental set up used by Tavner et al., 2016 is not compatible with the CED, which instead requires an infusion-based approach. Furthermore, the effect of post-mortem time on hydraulic permeability has not been investigated previously. In order to improve understanding of drug transport within brain matter, more information about differences between grey matter and WM, and anisotropy in the tissue are required.

WM anisotropy, due to directionality of axons in the matrix (Pieri et al., 2019; Winklewski et al., 2018; Walhovd, Johansen-Berg, and Karadottir, 2014), makes WM hydraulic permeability direction-dependent. This detail is often overlooked, and only a few theoretical studies have reported the effect of anisotropy of brain WM on the hydraulic permeability (Zhan, Baena, and Dini, 2019). To the best of our knowledge no experimental study has considered the anisotropy of WM at the millimetre and sub-millimetre scales or has investigated the effect of directionality of axons on hydraulic permeability.

The present study is aimed at experimentally determining brain tissue hydraulic permeability and its dependence on tissue microstructure, with focus on axon orientation. We use fresh ovine brain and perform experiments to determine the localised hydraulic permeability of WM using an infusion-based experimental set up, *iPerfusion* (Sherwood et al., 2016). We measure the flow across a specific part of WM in response to applied pressures and calculate the permeability from directly measured parameters for a sample of specific dimensions. Furthermore, we explore if the hydraulic permeability of WM changes with post-mortem time. We also investigate the effect of anisotropy of WM on the hydraulic permeability and, to the best of our knowledge, we provide the first experimental investigation reporting the effect of directionality of axons on the hydraulic permeability of WM.

4.2 Materials and Methods

4.2.1 Sample Preparation

Fresh ovine brains were arranged from a local slaughterhouse, and separate slices of 7-8 mm in thickness were made by cutting along coronal and sagittal directions. These cuts expose the cerebral WM from two perpendicular directions as shown in Fig. 4.1a,b. The matrix of cerebral WM is mainly composed of two constituents, the axons and extracellular matrix. In coronal cut slices, the axons are parallel to the surface area direction whereas in sagittal cuts they are perpendicular to the surface area direction, as represented by black dots and lines in the schematic representation shown in Fig. 4.1a. Using sharp blades, elongated specimens were obtained from a specific part of WM, corona radiata, and were carefully inserted in transparent plastic tubes of 5 mm inner diameter and 7 mm length. Special attention was paid to the size of the sample while cutting, in order to avoid excessive deformation during insertion into the tube. In the samples from coronal cut slices, the axons were parallel to the long axis of the tube ($S_{||}$), whereas in samples from sagittal cut slices ($S_{\perp}$), the axons were perpendicular to the long axis of the tube.

During the slicing of the brain, phosphate-buffered saline (PBS) was sprayed on the tissue in order to keep it hydrated. A plastic petri dish with

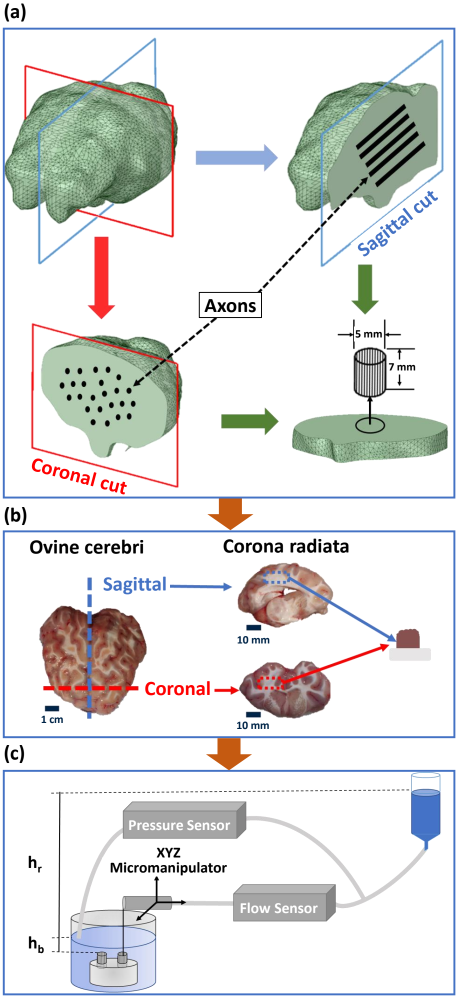

FIGURE 4.1: (a) Schematic representation of slicing the ovine brain along coronal and sagittal cuts showing the directionality of axons in WM and making of a tube shaped sample from the slice, (b) representative picture of ovine brain and the coronal and sagittal cut slices, where the corona radiata part of WM used for making the sample is highlighted by dashed rectangles and (c) schematic representation of the experimental set up including the plastic petri dish showing samples suspended in a glass bath filled with PBS.

custom made holes was used to hold the samples suspended in a glass bath filled with PBS at room temperature as shown in Fig. 4.1c to avoid dehydration of the tissue during the experiments.

To calculate hydraulic permeability from directly measured parameters, we used *iPerfusion* (Fig. 4.1c), developed to determine flow-pressure relationship in soft tissues as described elsewhere (Sherwood et al., 2016). The system uses an actuated reservoir to control the pressure drop across the tissue, while recording the flow rate through the tissue with a thermal flow sensor (Sensirion SLG150), with an accuracy of approximately $5nl/min$. The pressure is measured with a differential pressure transducer (Omegadyne PX409), with an accuracy of 0.04 $mmHg$. A needle (BD MicrolanceTM; stainless steel; 30G × 1⁄2"; 0.3 × 13 mm) was connected to a micromanipulator for insertion into the WM sample.

4.2.2 Experimental protocol and data acquisition

Prior to each acquisition, the pressure and flow sensors were calibrated. The needle was then inserted in the sample so that tip was in the middle of the sample, i.e. for a 7 mm long sample needle was inserted 3.5 mm. The sample was completely immersed in PBS, which was also the infusate, at room temperature. An initial pressure of 7 $mmHg$ was applied and was held until a stable condition for the flow rate was reached. This acclimatisation took 25-30 minutes and allowed the brain sample to adapt to the experimental environment.

An automated protocol of discrete applied pressure steps was then carried out, consisting of 10, 12.5, 15, 17.5, 20, 22.5 and 25 $mmHg$. For each step, the slope of the flow rate was estimated by linear regression over a moving window of 300 s and continuously monitored. Steady state was defined as when the slope was continuously less than 5 $nl/min/min$ for 60 s, and the subsequent step was then applied. The last 4 minutes of stable data step was extracted, a Savitzky-Golay filter with a 60 s half-width was applied to reduce noise, and the average values of the filtered signals were used to represent that steady pressure and flow values.

To determine tissue hydraulic permeability from the experimental data, flow-pressure analysis on the flow rate and pressure traces was performed using the model:

$$Q = kP\left(\frac{A}{L\mu}\right) = k_r P\left(\frac{P}{P_r}\right)^{\beta}\left(\frac{A}{L\mu}\right) \tag{4.1}$$

where Q is flow rate, P is the applied pressure drop across the tissue, A and L are the cross-sectional area and length of sample respectively and μ is the viscosity of the infused fluid. The pressure-dependence of hydraulic permeability is modelled using $k = k_r\left(\frac{P}{P_r}\right)^{\beta}$, where k_r is the hydraulic permeability at reference pressure P_r and the exponent β characterises the dependence of k on pressure. In this study, we chose P_r = 10 $mmHg$ as representative of physiological CSF pressure in adults (Dunn, 2002).

It should be noted that the full tissue length was used here to evaluate permeability; the assumption made here, whose validity has been checked and confirmed via poro-elastic simulations of the infusion process performed using the finite element method similar to those performed in (Zhan, Baena, and Dini, 2019) but for the samples under investigation here, is that the infused fluid exudes from both end of the tubes containing the samples.

Figure 4.2 shows representative flow rate and pressure traces with respect to time (a,b), and steady state flow rate (c) and hydraulic permeability for each applied pressure (d) for sample $S_{||}$ (blue) and $S_{\perp}$ (red) cases. Figures 4.2 (e,f) schematically represent the flow orientation with respect to the axon bundles.

Experiments were repeated on samples of corona radiata from different lamb brains. In total 71 brain samples with post-mortem time ranging from 3 to 24h were used to collect the experimental data.

It was not always possible to count each step as in some samples higher pressure steps did not achieve the steady state condition and were therefore excluded from data analysis. Only those samples were included for which at least three consecutive pressure steps (as shown in Fig. 4.2(a)) achieved the steady state condition and no anomalies were found in the instantaneous response to consecutive pressure rises. After quality control, 50 samples were analysed for the results presented in this work.

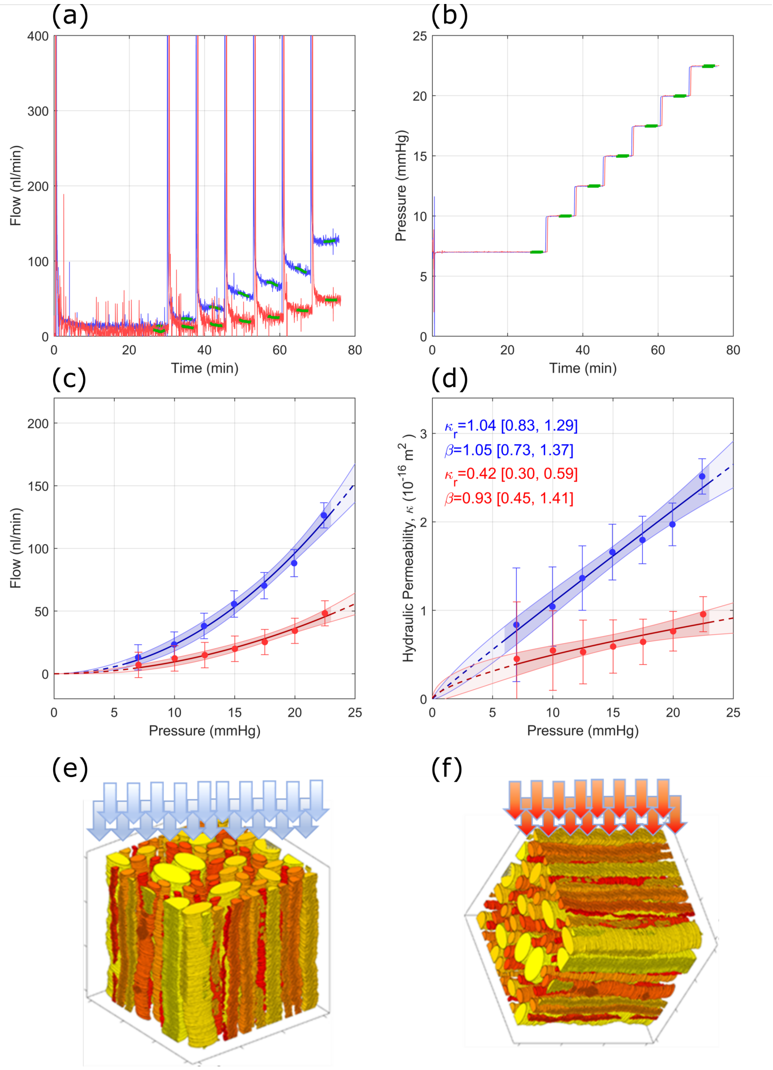

FIGURE 4.2: (a, b) Flow rate and pressure traces of representative $S_{\parallel}$ (blue) and $S_{\perp}$ (red) samples. Green lines show filtered signal. (c) Flow-pressure and (d) hydraulic permeability pressure relationships. Error bars show two standard deviations and shaded regions indicate 95% confidence bounds. The k_r and β values are the geometric mean with 95% confidence interval at all pressure steps. (e,f) Reconstruction of flow orientation relative to axons (Gu and Yao, 2003) for $S_{\parallel}$ and $S_{\perp}$, respectively.

4.3 Results and Discussion

4.3.1 Effect of axons directionality on hydraulic permeability

For statistical analysis, the average k_r of each sample was used (i.e. the average of all pressure steps for that sample). Shapiro-Wilk tests on k_r rejected normality for both $S_{\parallel}$ and $S_{\perp}$ samples ($p < 10^{-3}$), but did not reject lognormality ($p = 0.48$ and $p = 0.17$ respectively), hence analysis was carried out on the log of k_r. An overview of the hydraulic permeability data for $S_{\parallel}$ and $S_{\perp}$ samples is shown in Fig. 4.3.

For $S_{\parallel}$ samples, the average hydraulic permeability was $k_r = 2.0[1.3, 3.0] \cdot 10^{-16}\ m^2$ (geometric mean, [95% confidence interval]), while $S_{\perp}$ samples yielded $k_r = 0.7[0.6, 1.0] \cdot 10^{-16}\ m^2$. The hydraulic permeability was thus 65 [44, 78]% lower in $S_{\perp}$ than $S_{\parallel}$ samples (independent 2-tailed t-test, $p = 0.0002$). This trend is in line with what can be predicted by modelling the flow behaviour due to anisotropy through a composite material consisting of impermeable coarse fibres embedded in a fine matrix as proposed e.g. by Ethier, 1991. However, considering that, as reported by Syková and Nicholson, 2008, the volume fraction of fibres in the tissue is 70-80%, a direct quantitative comparison with Ethier's model, which is most accurate for small fibres volume fraction (up to 30%), would prove inaccurate.

These results confirm that the flow across the tissue is strongly dependent on the local mechanical microenvironment. The WM matrix is composed of aligned myelinated axons and relatively soft extracellular matrix (Alexander et al., 2019). In the case of $S_{\parallel}$, the cross sectional area of the tissue exposed to infusate pressure is composed of both axons and the relatively soft ECM, whereas in case of $S_{\perp}$, the exposed cross-sectional area is predominantly composed of axons (Pieri et al., 2019). It is harder to deform axons (stiffness of a single axon reported to be e.g. E = 9.5 kPa (Ouyang, Nauman, and Shi, 2013)) than ECM (E in the order of a few hundred pascals (Wells, 2008)). Therefore, in case of infusion, depending on the directionality in the tissue, the infusate faces different mechanical environments. Previously it has been reported that in WM, interstitial flow is more rapid in perivascular space and along the axons (Abbott, 2004; Geer and Grossman, 1997). Also, interstitial flow is impacted by convection driven flow. In CED, catheter delivers a volume of infusate to the targeted part of the tissue; this also increases interstitial flow in the surrounding parenchyma because of the pressure differential (Stine and Munson, 2019). This suggests that if diffusion driven interstitial flow is more rapid in perivascular space and along the axons then convection driven flow will have similar behaviour. Our results also advocate this environment dependency of flow in the tissue. In the case of $S_{\parallel}$, when the axons are aligned to the injection direction the hydraulic permeability is higher, whereas in case of $S_{\perp}$, the axons are perpendicular to the fluid, and the hydraulic permeability is lower. These results clearly demonstrate that infusion across the WM tissue, and hence its hydraulic permeability, is strongly influenced by its intrinsic anisotropy. Therefore, the directionality of axons in the tissue should be considered when interpreting underlying infusion mechanisms within WM.

Our hydraulic permeability values of the ovine brain WM are the first experimentally determined values that consider localisation and tissue anisotropy. Franceschini et al., 2006 and Tavner et al., 2016 experimentally studied the permeability of brain tissue without considering the directionality in the tissue. Furthermore, their reported value of permeability is obtained using large samples of WM; hence, they can only represent homogenised isotropic macroscopic values of permeability. These issues make it inappropriate to compare our results with other experimental results in the literature. It is, however, worth noting that the values obtained in our experiments seem to confirm the disparity in permeability predicted when considering microstructural effects and different orientations of infusion, as reported in previous theoretical and numerical studies (Vidotto et al., 2019a).

The results reported in Fig. 4.3 clearly demonstrate the difference in hydraulic permeability between $S_{\parallel}$ and $S_{\perp}$ and thus the dependence of this parameter, and in turn of CED procedures, on the directionality of axons in WM. This strongly encourages to consider the anisotropy of WM tissue when modeling the localised pressure-flow behavior in infusion phenomenon and when assessing interstitial transport in brain tissue due to physiological conditions or CED procedures.

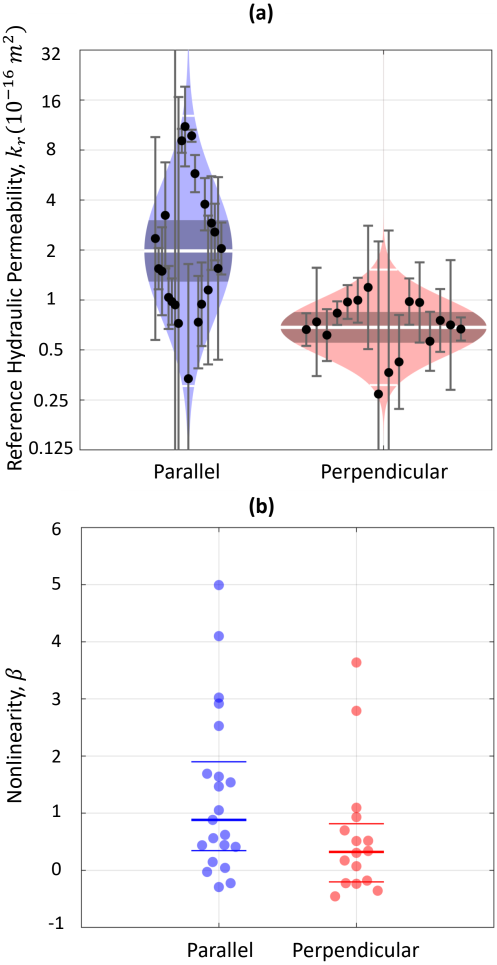

FIGURE 4.3: Hydraulic permeability of $S_{\parallel}$ and $S_{\perp}$ samples and their pressure dependence. (a) Cello plot representing each k_r value by dot with the error bars showing 95% confidence intervals, best estimate of the distribution by shaded regions, geometric mean by the central horizontal white line, two-sigma within which 95% data are expected to lie by horizontal out thin white lines and 95% confidence intervals on the mean value by dark central bands, (b) the nonlinearity, β, for $S_{\parallel}$ and $S_{\perp}$ samples, dots represent each data point, central dark line represents the median and out two lines represent the IQR.

4.3.2 Pressure dependence of hydraulic permeability

Our data also revealed a pressure-dependence of the hydraulic permeability. Fig. 4.3b shows the non-linearity parameter, β, for both $S_{\parallel}$ and $S_{\perp}$ samples. The Shapiro-Wilk test rejected both normality ($p < 0.03$) and log-normality ($p < 10^{-5}$) for β, hence a non-parametric analysis is utilised. For $S_{\parallel}$ samples, the β was 0.88 (0.34, 1.90) (median (25^{th} percentile, 75^{th} percentile)), which is significantly different from zero ($p = 0.0002$, two-sided Wilcoxon rank sum test), implying that hydraulic permeability increases with increasing pressure. $S_{\perp}$ samples, yielded β = 0.32 (-0.20, 0.81), which is borderline different from zero, ($p = 0.04$). The median β was therefore 64% lower for $S_{\perp}$ than $S_{\parallel}$, although this outcome was borderline statistically significant ($p = 0.07$).

The non-linearity in the observed pressure-flow relationships could be caused by several sources, including strain-dependence of hydraulic permeability due to the local tissue response to deformation, but also other material (both solid response to pressure gradients and complex fluid flow behaviour) and geometrical non-linearities, which include the boundary conditions at the infusion site, the cavity formed at the tip of the catheter. Based on macroscale experiments, both, the stiffening behavior under tension (Franceschini et al., 2006) and the softening behavior (Miller and Chinzei, 2002) in brain tissue due to geometrical non-linearities have been reported in the literature. Several poroelastic or biphasic models of brain tissue have been developed to explain such experimental results. Considering a simplified spherical geometry, Smith and García, 2009 modeled the enlargement of the infusion sphere relative to its initial radius with increase in applied pressure, which results in geometrical non-linearity. Considering the biomaterial as a poroelastic medium, McGuire, Zaharoff, and Yuan, 2006 performed numerical simulations and showed that strain dependent permeability is anisotropically affected by infusion-induced tissue deformation. It should be noted that the models presented in these studies represent the brain tissue as fundamentally homogeneous and isotropic and were developed to explain previously reported experimental results, which are based on compression of large samples rather than infusion. These approaches therefore only provide the large-scale bulk response of the tissue and cannot be used to describe the effect of microstructurally-induced anisotropy.

It must be noted that another potential source of non-linearity could be the existence of flow along the needle/tissue interface. This form of *leakage* cannot be completely ruled out in the absence of detailed localized flow measurements; this could be responsible for some of the larger values of β reported in this study. However, the fact that the non-linearity parameter is larger in the specimens characterized by parallel axon fibers (see Fig. 4.3(b)), which shows that the non-linear response depends on the orientation of the fibers whilst leakage would equally affect all samples. This, together with the evidence provided by the studies reported above, provide us with reasons to believe that the non-linear pressure dependence reported in our study is likely to be related to the subtleties of infusion induced microscale deformation of the WM tissue. Further studies, employing direct microscopic measurements of tracked nano- and micro-particles, will be devoted to exploring the main source of the non-linearity of the pressure-flow relationship and to verify the absence of needle side leakage.

4.3.3 Effect of post-mortem time on hydraulic permeability

The effect of post-mortem time on the mechanical behaviour of brain tissue has been reported in the literature (Nicolle et al., 2005), though not much attention has been paid to the effect of post-mortem time on hydraulic permeability. For example, mechanical stiffness of WM has been reported to increase with post-mortem time, with specific changes recorded after 6h post-mortem (Garo et al., 2007). Here, we analysed the hydraulic permeability at post-mortem times up to 11h. No statistical correlation between post-mortem time and hydraulic permeability was observed: for $S_{\|}$, $\rho = -0.003$ ($p = 0.99$) and for $S_{\perp}$, $\rho = -0.09$ ($p = 0.7$) using Spearman's ranked correlation test.

It should be noted here that whilst the results obtained during this study were consistent for experiments performed within 11h post-mortem, experiments performed after 11h post-mortem either failed by showing significant anomalies in the instantaneous response to pressure steps or registered sudden abrupt changes in flow, which can be reconducted to tissue rupture during testing. As a result of this none of these experiments passed the quality control measures to be included in the data analysis.

4.4 Conclusions

The localised hydraulic permeability of brain WM, despite being a key parameter for the development of infusion-based technologies, has so far not been systematically studied experimentally. In this work we investigated for the first time the effect of local microstructural features on hydraulic permeability of cerebral WM in a systematic manner using an infusion based experimental set up. We accounted for the directionality of axons in WM and showed the dependence of hydraulic permeability on the anisotropy in WM tissue. We also investigated whether it is affected by post-mortem time.

Our results demonstrate that the mean value of hydraulic permeability is significantly higher when the axons in WM are parallel to the flow direction than when axons are perpendicular to the flow direction. We also observed a pressure dependent increase in hydraulic permeability. Although there was no correlation between hydraulic permeability and post-mortem time within 11h, the tissue degradation at later times significantly affected our ability to measure hydraulic permeability after 11h.

Our experimental results provide quantitative values of hydraulic permeability as a function of the direction of the WM fiber bundles from directly measured parameters. These can be used to enhance the development of technologies such as CED and as a prime source of information to build detailed mechanical models of brain tissue. Additionally, this investigation provides further evidence of the need to include tissue anisotropy as one of the key parameters for the optimization of infusion-based drug delivery techniques.

Acknowledgments

This work was supported by EDEN2020, a project funded by the European Union's H2020 Research and Innovation Programme under the grant agreement No. 688279.

Chapter 5

Advanced imaging methods to improve the predictive capabilities of CED models

In this chapter, we present an innovative predictive CED model based on the integration of two imaging modalities. The first is diffusion tensor imaging which provides information on the principal directions followed by the axonal fascicles. The second is the neurite orientation dispersion and density imaging from which it is possible to extract the extracellular space volume fraction, a fundamental information about the white matter microstructure. By tailoring this parameter with a simplified geometrical model of the white matter, we can assign anisotropic permeability values to each voxel. To show the significance of our approach, we compare it with a state of the art model based only on diffusion tensor imaging. The results, analysed in terms of distribution shape, concentration profile and infusion linear penetration length, show significant differences with respect to previous models only based on DTI. We believe that the proposed approach is a decisive step further in CED modelling because it introduces a more comprehensive way to describe the permeability tensor which has its foundation on the studies conducted in the previous chapters.

This work is under second review as: Vidotto, M., Pederzani, M., Castellano, A., Pieri, V., Falini, A., Dini, D., & De Momi, E. (2020). "Advanced imaging methods to improve the predictive capabilities of CED models", *Annals of Biomedical Engineering*.

5.1 Introduction

The blood-brain barrier (BBB) is an highly selective semipermeable vascular system composed by endothelial cells, astrocyte end-feet, and pericytes that serves as a diffusion barrier (Ballabh, Braun, and Nedergaard, 2004). Despite the BBB is essential for the normal function of the central nervous system, it is also a dramatically effective barrier that prevents most drugs from going from the blood stream to the brain tissue (Ballabh, Braun, and Nedergaard, 2004). For this reason, the BBB has been clearly identified as the main cause of the failure of chemotherapeutic treatments that aim at targeting the brain tissue (Bobo et al., 1994; Arifin et al., 2009; Crawford, Rosch, and Putnam, 2016; Jahangiri et al., 2016).

To overcome this obstacle, an innovative and promising technique, namely convection-enhanced delivery (CED), has been introduced by Bobo et al., 1994, consisting in injecting a therapeutic agent under positive pressure directly into the brain parenchyma by means of one or more catheters. CED was originally designed for treating aggressive tumors such as glioblastoma multiforme (GBM) which has a dramatically low survival rate, with only about 40% of the patients living more than a year after diagnosis (Philips et al., 2018). CED could offer a viable alternative to more conventional treatments, which consist in surgical resection followed by simultaneous radiation therapy and chemotherapy (Mehta et al., 2015). Indeed, despite these treatment approaches being highly aggressive, patients' outcome remains dismal and around 80% of them experience tumoral recurrence or progression in the following years (Crawford, Rosch, and Putnam, 2016; Davis, 2016). Moreover, CED has been recently used for delivering therapeutic substances for other brain diseases such as gene therapy for Parkinson's disease and antiseizure agents for epilepsy (Christine et al., 2019; Rogawski, 2009).

Regardless of the pathology, a pivotal factor for CED efficacy is the ability to reach all the diseased tissue with enough concentration of therapeutic agent, and, on the other hand, to leave the healthy tissue unaltered as much as possible to avoid side effects (Crawford, Rosch, and Putnam, 2016; Debinski and Tatter, 2009; Jahangiri et al., 2016). To optimise the treatment and to obtain better clinical outcomes, a valuable support is given by numerical models (Vendel, Rottschäfer, and Lange, 2019). In fact, by modelling the brain structures and the drug characteristics, they can predict how the drug will distribute in the brain for a given initial catheter setup. In this way, in the preoperative phase, the surgeon can examine different clinical settings (e.g. catheter placement, infusion flow rate) and plan the best way to proceed (Crawford, Rosch, and Putnam, 2016; Jahangiri et al., 2016).

Nevertheless, since brain is an anisotropic and heterogeneous porous tissue composed of grey matter (GM), white matter (WM), cerebrospinal fluid (CSF) and blood vessels (BV), modelling CED is extremely challenging (Vendel, Rottschäfer, and Lange, 2019; Goriely et al., 2015). In the last years, several researchers have proposed numerical models based on different hypotheses and assumptions (Ehlers and Wagner, 2015; Kim et al., 2012; Linninger et al., 2008a; Raghavan and Brady, 2011; Sarntinoranont et al., 2006; Støverud et al., 2011; Zhan, Baena, and Dini, 2019). However, their predictions do not always match the experimental observations, thus suggesting that there is still a long way to go to guarantee an accurate targeting of the zones of interest. This can be due to several reasons, but a key factor is related to how the microstructure of the brain tissue is modelled, both at the injection site and in the targeted area (Vidotto et al., 2019a).

All the investigations previously mentioned related to CED models development used diffusion tensor imaging (DTI) to depict non-invasively the tissue microstructure which in turn affects the penetration of the drug molecules. Indeed, DTI is a non-invasive imaging modality that measures the effects on the magnetic resonance signal intensity of water molecules diffusion over time. The resulting diffusivity tensor is isotropic in the case of GM, mainly composed by cell bodies, and anisotropic in the case of WM, whose microstructure is dominated by axonal fibres (O'Donnel, L; Westin, 2011). DTI represents a powerful tool because it allows inferring some aspects of the brain microstructure, thus giving important information that can be used to define specific modelling parameters. Despite DTI being extremely useful, it has an important limitation. It does not provide any information about the extracellular space volume fraction (VF_{ECS}) of the brain tissue. Critical modelling parameters, such as hydraulic permeability, are directly related to the VF_{ECS}

(Vidotto et al., 2019a); therefore, this missing information represents an important drawback affecting the currently available models.

In this work, we aim at overcoming the limitations of the DTI-based approach and improving the model predictive capability by discussing a methodology that enables to consider the information related to the VF_{ECS} and we demonstrate its use in a single case-study of a healthy subject. In contrast to previous models, we not only consider DTI-derived information, but we also incorporate a more comprehensive quantification of the brain tissue microstructural complexity derived from a more sophisticated multicompartmental diffusion model, namely the neurite orientation dispersion and density Imaging (NODDI) (Zhang et al., 2012). Indeed, NODDI relies on more complex diffusion data fitted by a tissue model that distinguishes three compartments with different microstructural characteristics: intracellular, extracellular and CSF compartments. Each environment affects the diffusion of the molecules differently, thus giving rise to separate signals. By estimating the relative contribution of the three distinct compartments to the total diffusion signal in each voxel, it is possible to infer the VF_{ECS} in every part of the brain. We first derive a relationship between VF_{ECS} and WM hydraulic permeability conducting a numerical analysis on a simplified geometrical model.

We then demonstrate the relevance of the work by comparing our model with another state-of-the-art model by conducting the same drug delivery simulations and comparing the outputs in terms of infusion volume and shape. We show that the predictions given by our model differ significantly from those given by the models that use only DTI and using a fixed value of permeability. We finally discuss the important implications that the new CED modelling framework has in terms of its potential future use in pre-clinical trials.

5.2 Materials and Methods

5.2.1 Imaging dataset

The brain is a porous medium, where the solid part is composed of neurons and glial cells, and the voids represent the extracellular space (Nicholson, Kamali-Zare, and Tao, 2011). Accordingly, information relative to the volume fraction occupied by each region are important to describe brain properties. With NODDI it is possible to extract, for each voxel, the volume fraction occupied by the intraneurite (VF_{INC}) and isotropic (VF_{Water}) compartments. Each environment affects the diffusion of the molecules with different contributions giving rise to separate signals (Zhang et al., 2012). In this work, we used an imaging dataset acquired on a healthy adult subject on a 3T Ingenia CX scanner (Philips Healthcare, Best, The Netherlands), with a 32-channel head coil. The study was approved by the OSR Institutional Ethics Committee, and signed informed consent was provided by the subject before magnetic resonance imaging (MRI).

The MRI protocol included:

- a two-shell Diffusion MR Imaging (dMRI) sequence, based on axial Single-Shot Spin-Echo echo planar imaging (EPI). Diffusion gradients were applied along 35 and 60 non-collinear directions, and images were acquired at multiple b-values (0, 711, and 3000 s/mm^2), with the following parameters: TR/TE 5977/78 ms; flip angle, 90°; 60 slices; thickness, 2/0 mm gap; acquisition matrix, 128 × 126; voxel size, 2 × 2 × 2 mm; SENSitivity-Encoding (SENSE) reduction factor, R=2; Multiband factor=2. Twelve images without diffusion weighting (b=0 s/mm^2) were obtained, one of which was acquired with reversed phase-encoding to estimate susceptibility-induced distortions. This diffusion imaging dataset was exploited to extract both tensorial and NODDI metrics, to be combined in the model.
- a sagittal 3DT1-weighted sequence, acquired with the following parameters: repetition time/echo time [TR/TE] 12/5.9 ms; flip angle, 8°; 236 slices; thickness, 0.8/0 mm gap; acquisition matrix, 320 × 299; voxel size, 0.8 × 0.8 × 0.8 mm; SENSE factor, R=2; acquisition time, 5 min 19 s. This anatomical sequence was exploited to achieve the preoperative planning of the simulated gadolinium (GD) solution infusions along nine different catheter orientations.

dMRI volumes were corrected for eddy-current distortions, movement and susceptibility-induced artifacts by applying the *eddy* and *top-up* tools of

FMRIB Software Library, respectively (FSL, University of Oxford, `https://fsl.fmrib.ox.ac.uk/fsl/`).

DTI analysis was performed on high angular resolution diffusion-weighted Imaging (HARDI) volumes (60 diffusion directions, b-value= 3000 s/mm^2) extracted from the multi b-value dMRI dataset using the *fslsplit* and *fslmerge* FSL-tools. The *dtifit* FSL-tool allowed estimating the diffusion tensor and generating tensorial maps, such as Fractional Anisotropy (FA) which measures the fraction of the diffusion that is anisotropic (O'Donnel, L; Westin, 2011).

The NODDI model was fitted to all the volumes of the two-shell dMRI datasets using the MATLAB NODDI toolbox (`http://mig.cs.ucl.ac.uk/Tutorial.NODDImatlab`), that computed the VF_{INC} and VF_{Water} diffusion compartments of each voxel. Those outputs were then reparameterized in order to derive the extraneurite diffusion compartment (VF_{ENC}), so that the sum of the three compartments equalled 1 in each voxel, as described in Caverzasi et al., 2016. Hence, the VF_{ECS} that we integrated in our model was finally derived as VF_{ENC}+VF_{Water}, which corresponds to the sum of the compartments where a drug can flow (Vandamme et al., 2017).

5.2.2 Brain tissue modelling

The brain is an extremely complex system whose tissue mainly consists of cells immersed in the CSF. Despite most of the relevant literature agrees to describe the brain as a porous medium, there is not a common answer on which specific model is the most appropriate to use. Indeed, one of the most controversial aspect is the modelling of the solid part that can be described as elastic or rigid. For example, Støverud et al., 2011 and Ehlers and Wagner, 2015 used a linear elastic material and an hyperelastic material, respectively, whereas other authors adopted rigid models (Dai et al., 2016; Kim et al., 2012; Kim, Mareci, and Sarntinoranont, 2010). On the one hand, elastic models offer a more accurate description with respect to rigid models by considering the infusion-induced tissue deformation. However, complex models require a larger number of parameters, that could be hard to identify, and a high computational cost. On the other hand, rigid models demonstrated to be reliable when the deformation can be neglected and with a much lower computational cost with respect to elastic models. Since in this study we are simulating procedures that require very low flow rate, we can safely neglect the infusion-induced deformation and model the axons as a rigid material (Dai et al., 2016; Kim et al., 2012; Kim, Mareci, and Sarntinoranont, 2010; Vidotto et al., 2019a). Accordingly, the continuity equation is (Vidotto et al., 2019a):

$$\nabla \cdot v = 0 \tag{5.1}$$

where v is the average extracellular fluid velocity and ∇ is the gradient operator. Moreover, fluid flow in a porous medium is described by Darcy's law (Kim et al., 2012):

$$v = -\frac{\mathbf{K}}{\mu} \cdot \nabla p \tag{5.2}$$

where p is the fluid pressure, and $\mathbf{K}$ is the hydraulic permeability tensor. Mass transport in the brain tissue is driven by convection, diffusion and loss due to absorption or washout:

$$\frac{\partial c}{\partial t} = -\nabla \cdot (vc) + \nabla \cdot (\mathbf{D} \cdot \nabla c) - S \tag{5.3}$$

where c is the GD concentration, S is the loss term (0.01 min^{-1}) and $\mathbf{D}$ is the diffusivity tensor (Nhan et al., 2014).

The brain model was divided in three areas following the thresholding suggested by Kim et al., 2012, as summarized in Table 5.1. Each area has different properties that define the permeability and diffusivity tensors as it will be explained in the next sections.

5.2.3 Diffusion tensor

GM regions are characterized by isotropic diffusion. Accordingly, $\mathbf{D_{GM}}$ is defined as:

$$\mathbf{D_{GM}} = D_0 \cdot \mathbf{I} \tag{5.4}$$

TABLE 5.1: Thresholding applied to divide the brain model between GM, WM and CSF.

Tissue region	Threshold range
Gray matter	$0 < \mathrm{FA} < 0.23$
White matter	$VF_{Water} > 0.99$
Cerebro-spinal fluid	0.25

where D_0 is the GD molecular diffusivity, equal to $1.54 \cdot 10^{-7}$ *kg/ms*, and $\mathbf{I}$ is the (3x3) identity matrix.

On the contrary, in WM, diffusion is anisotropic. The principal direction of the diffusion tensor $\mathbf{D_{WM}}$ was assumed as the maximum transport direction along the axons, as measured by DTI. Since water diffusion tensor $\mathbf{D}$ is symmetric and positive definite, it is possible to define three orthogonal eigenvectors ($\overrightarrow{e_1}$, $\overrightarrow{e_2}$, $\overrightarrow{e_3}$) with the corresponding eigenvalues (λ_1, λ_2, λ_3). To account for the molecular transport of GD, eigenvalues obtained from $\mathbf{D}$ at each voxel must be scaled according to the GD molecular diffusivity, as described in Linninger et al., 2008a, following these steps.

Step 1

$$\mathbf{D}E = E\mathbf{\Lambda} \quad \text{where} \quad \mathbf{\Lambda} = \begin{bmatrix} \lambda_1 & 0 & 0 \\ 0 & \lambda_2 & 0 \\ 0 & 0 & \lambda_3 \end{bmatrix} \quad \text{and} \quad E = [\overrightarrow{e_1}, \overrightarrow{e_2}, \overrightarrow{e_3}] \tag{5.5}$$

Step 2

$$\mathbf{D_{WM}} = \frac{D_0}{\overline{\lambda}} E \begin{bmatrix} \lambda_1 & 0 & 0 \\ 0 & \lambda_2 & 0 \\ 0 & 0 & \lambda_3 \end{bmatrix} E^T \quad \text{where} \quad \overline{\lambda} = \frac{1}{3}\sum_{i=1}^{3} \lambda_i \tag{5.6}$$

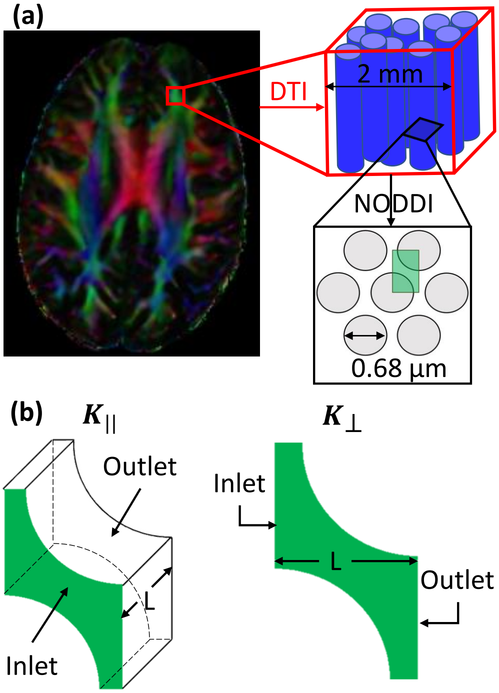

FIGURE 5.1: (a) This picture offers a schematic representation of the leading idea behind this study which combines both DTI and NODDI imaging modalities. DTI provides information about the WM fibres directionality: on the left, an axial section of FA map of a healthy subject, displayed as colour-orientation map. Latero-lateral-oriented fibres are coded in red, cranio-caudal fibres in blue, and antero-posterior fibres in green. The neural fibres orientation (red box) is then used to define the permeability tensor eigenvectors. On the other hand, NODDI gives an insight into the axons composing the fascicles microstructure (black box) thus allowing the definition of the permeability tensor eigenvalues. Accordingly, the WM is modelled as a triangular arrangement of fibres. Each grey circle represents the section of an axon, whereas the green box is the representative volume element (RVE) analysed (Vidotto et al., 2019a). (b) Model geometries used to compute $k_{||}$ and $k_{\perp}$. The green shapes represent the extracellular space of each geometry, namely, the space where the fluid can flow. On the left, 3D geometry used to simulate a flow parallel to the fibres with L = 0.15 μm. On the right, the bi-dimensional geometry used to simulate a flow perpendicular to the direction of the fibres with L that varied according to different values of VF_{ECS}.

5.2.4 Permeability tensor

Tensor $\mathbf{K}$ was characterized differently in GM and WM areas. Since in GM, $\mathbf{K}$ can be considered isotropic, $\mathbf{K_{GM}}$ was defined by the following equation:

$$\mathbf{K_{GM}} = K_0 \cdot \mathbf{I} \tag{5.7}$$

where K_0 is equal to $4.22 \cdot 10^{-18}\ m^2$ (Kim et al., 2012).

On the other hand, in WM areas, the permeability tensor $\mathbf{K_{WM}}$ is transversely isotropic with the main transport direction that coincides with the one identified for $\mathbf{D_{WM}}$.

$$\mathbf{K_{WM}} = E \begin{bmatrix} k_{||} & 0 & 0 \\ 0 & k_{\perp} & 0 \\ 0 & 0 & k_{\perp} \end{bmatrix} \tag{5.8}$$

where $k_{||}$ and $k_{\perp}$ describe the hydraulic permeability in directions parallel and perpendicular with WM fibers, respectively. In previous studies (Kim et al., 2012; Kim, Mareci, and Sarntinoranont, 2010), these parameters had a fixed values in all the brain ($k_{||} = 6.75 \cdot 10^{-15}\ m^2$ and $k_{\perp} = 4.22 \cdot 10^{-16}\ m^2$). On the contrary, in the proposed model, $k_{||}$ and $k_{\perp}$ change spatially as a function of VF_{ECS} as detailed in the next section.

5.2.5 Geometrical model

To study how $k_{||}$ and $k_{\perp}$ are related to VF_{ECS}, we conducted a numerical analysis on a simplified model geometry resembling the WM structure. Adopting an approach similar to the one developed in Vidotto et al., 2019a, the axons were simulated as cylinders with rigid walls and the extracellular space corresponding to the space where the fluid could flow. Even in this case, as explained in the *Brain tissue modelling* section, it is possible to safely consider the axons as rigid if the flow rate is very low. The axons, with constant radius $r = 0.34\ \mu m$ (Liewald et al., 2014), were organized following a triangular arrangement (Fig. 5.1a). Then, varying the distance between the axons, it was possible to obtain a set of geometries with VF_{ECS} ranging from 0.15 to 0.80.

Note that we performed more simulations in the interval between 0.15 and 0.40 because it is the physiological range indicated in Syková and Nicholson, 2008. Moreover, it is necessary to specify that describing the axonal bundles with arrays of constant-radius cylinders is an important assumption that will be argued in the *Discussion* section comparing our results with other studies (Franceschini et al., 2006; Vidotto et al., 2019a).

For each geometry, a pressure difference of 5 Pa was applied between inlet and outlet with no sleep condition at the walls (Fig. 5.1b). This pressure was chosen to maintain a very low flow rate and to satisfy the assumptions that allow Darcy's law to be used to model flow in the tissue. The average velocity within the medium, along the direction over which the gradient of pressure was applied, was computed solving the Navier-Stokes equations by means of the finite element method (FEM) solver ANSYS (ANSYS, Lebanon, NH) with semi-implicit methods for pressure linked equations. Then, both $k_{\|}$ and $k_{\perp}$ were computed using Darcy's law (Eq. 5.2). Finally, the numerical results describing the relation between VF_{ECS} and permeability were fitted using the analytical equations developed by Tamayol and Bahrami, 2009 for $k_{\|}$ and Kuwabara, 1959 for $k_{\perp}$. We selected these equations as they were shown to be the most accurate models in the comparative analysis on permeability of fiber bundles performed by Karaki et al., 2017. The resulting equations, whose coefficients were obtained using a generalized reduced gradient nonlinear solver, are reported below:

$$\begin{gathered} k_{\|} = \frac{r^2}{7.77(1 - VF_{ECS})}(-1.47 - 0.94ln(1 - VF_{ECS}) + \\ 2(1 - VF_{ECS}) - 0.5(1 - VF_{ECS})^2 - 0.039(1 - VF_{ECS})^4 \end{gathered} \tag{5.9}$$

$$\begin{gathered} k_{\perp} = \frac{r^2}{2.97(1 - VF_{ECS})}(-1.56 - 1.04ln(1 - VF_{ECS}) + \\ 2.05(1 - VF_{ECS}) - 0.5(1 - VF_{ECS})^2 - 0.004(1 - VF_{ECS})^4) \end{gathered} \tag{5.10}$$

5.2.6 CED simulation set-up

The proposed method, in which the permeability tensor is a function of the VF_{ECS}, was compared with the approach used in Kim et al., 2012; Kim, Mareci, and Sarntinoranont, 2010; Dai et al., 2016. Their CED models, based on DTI imaging acquired on rat brains, assumed that, in the permeability tensor, $k_{||}$ and $k_{\perp}$ can be considered constant across all the WM areas. However, many studies (Ehlers and Wagner, 2015; Støverud et al., 2011; Vidotto et al., 2019a) have underlined the fact that permeability is still a very controversial parameter with a wide range of values available in the literature. For brevity, we name our model the DTI-NODDI model and we will refer to the more conventional models, such as those developed by Kim et al., 2012; Kim, Mareci, and Sarntinoranont, 2010; Dai et al., 2016, as the DTI model.

Both models simulate an injection of a GD solution in a WM area by means of a 1 mm diameter catheter (Fig. 5.2a). As boundary conditions for the flow,

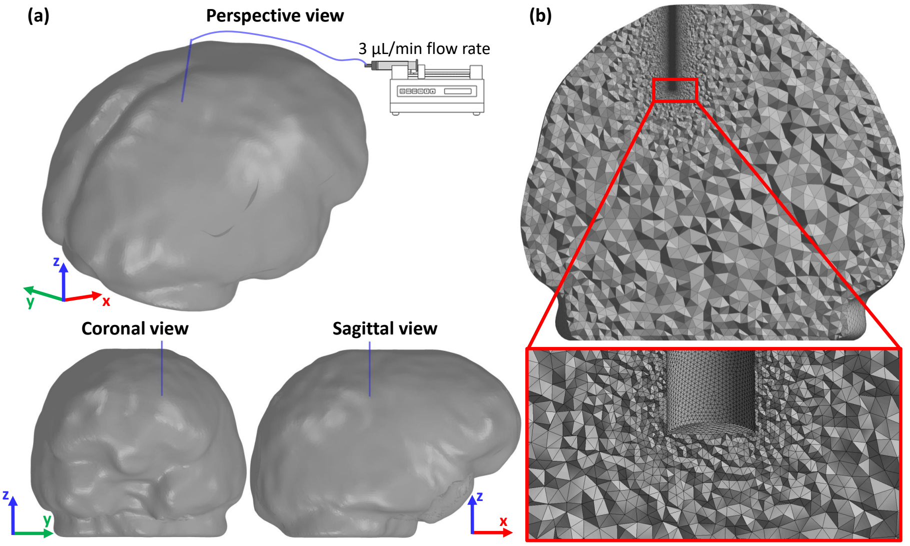

FIGURE 5.2: (a) Perspective view, coronal view and sagittal view of the brain model reconstructed from the healthy control dMRI dataset, with the infusion catheter inserted in a WM region. The model simulates a constant infusion rate of 3 $\mu L/min$. (b) Coronal section plane with a detail of the final mesh adopted for all the simulation after sensitivity analysis (Appendix).

a velocity was set at the inlet directed as the catheter, knowing that the infusion rate was 3 $\mu L/min$ (Barua et al., 2014), and a null pressure at the outlet. Moreover, GD concentration at the inlet was fixed to $c_0 = 0.5\ mol/L$, and no flux was allowed across the external surface of the brain. The entire volume was discretized with about $3.5 \cdot 10^6$ tetrahedral elements after performing a mesh sensitivity analysis (Appendix). Note that a finer mesh was used in proximity of the catheter (Fig. 5.2b). The total infusion time, equal to 180 seconds, was chosen empirically as a convenient time frame to maintain the infused volume confined in a WM area. The simulations were repeated for nine different orientations of the catheter (Fig. 5.3).

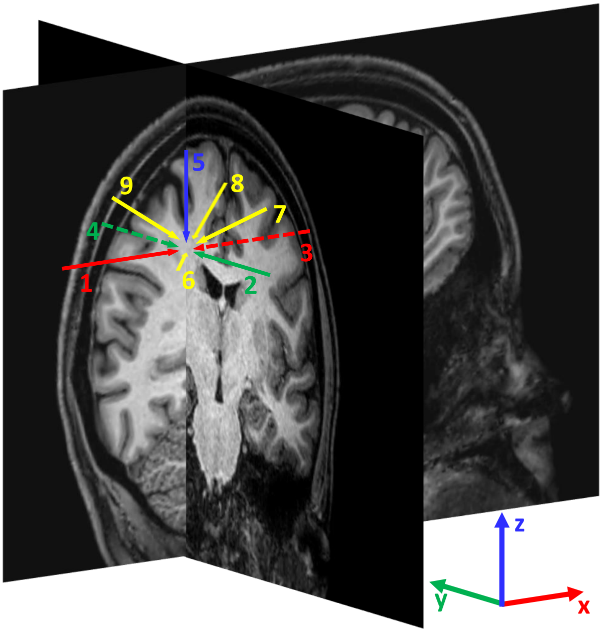

FIGURE 5.3: Scheme of the nine catheter orientations used to simulate the injection of the drug. To define the orientations, the brain coronal and sagittal planes intersecting the injection point are shown on 3D-T1 weighted sequence. Catheters 1 and 3 lie on the sagittal plane and in parallel with the x axis; catheters 2 and 4 lie on the coronal plane in parallel with the y axis; catheter 5 lie on the intersection between the sagittal and coronal planes; catheters 6, 7, 8, and 9 lie on the bisector of the solid angle defined by the semi-axes [-x, -y, z], [x, -y, z], [x, y, z] and [-x, y, z] respectively.

5.2.7 Metrics

Quantitative analyses were performed to examine the difference between the DTI-NODDI model and the DTI model in terms of drug concentration and distribution.

Concentration

An analysis of the drug distribution was carried out to investigate differences in the prediction of the tissue concentration. The root mean square difference (RMSD) represents a good parameter to evaluate how much the results predicted by the models differ in terms of concentration (Raghavan and Brady, 2011). It is defined as:

$$RMSD = \frac{1}{c_0}\sqrt{\frac{1}{V_{total}}\sum_{i=1}^{n} V_i(c_{DTI} - c_{DTI-NODDI})^2} \tag{5.11}$$

where V_{total} is the total volume occupied by the models, V_i is the volume of each element belonging to V_{total} and c_{DTI} and $c_{DTI-NODDI}$ are the local concentrations in the two models. Note that, similarly to Raghavan and Brady, 2011, only the elements where the drug concentration is higher than 2.5% of the infused concentration (c_{min}), were considered.

Main distribution direction

To compare how the drug distributes inside the brain tissue in terms of main distribution direction, a principal component analysis (PCA) was performed (Abdi and Williams, 2010). The PCA was conducted on the coordinates of each element where the presence of drug was detected. Even in this case, we considered only the voxels with a concentration higher than c_{min}. Performing a PCA on these data returns the principal direction along which the drug spreading has occurred.

From the PCA output, two additional analyses were conducted. In the first, we computed the angular difference between the infusion volumes principal directions in the two models at 180 seconds (θ).

In the second, we compared the linear penetration length (L_{max}) of the infusion volumes computed along the principal direction defined by the PCA.

5.3 Results

5.3.1 Permeability tensor characterization

The results of the numerical study to characterize the permeability tensor are graphically shown in Figure 5.4. The numerical permeability values were fitted finding the coefficients of the analytical equations developed in Tamayol and Bahrami, 2009 and Kuwabara, 1959 for $k_{||}$ and $k_{\perp}$, respectively. Both parallel (Eq. 5.9) and perpendicular (Eq. 5.10) permeabilities have a similar trend which grows logarithmically as VF_{ECS} increases.

5.3.2 GD concentration distribution

Figure 5.5 shows an example of the predicted GD concentration after infusion in a WM region for both models on different section planes. From a qualitative point of view both differences in shape and in concentration distribution can be noticed from the contour plots. In particular, a marked difference in the shape of the areas is evident comparing the GD distribution outlines obtained with the two models (Fig. 5.5 bottom row). The outlines were defined finding the more external elements with a GD concentration higher than c_{min}. Indeed, the one predicted by the DTI model is generally more elongated than the one predicted by the model that also integrates NODDI. This observation is confirmed by the fact that in all the simulations the overlapping volume between DTI and DTI-NODDI models is about 57% ± 1.4% which means that brain areas interested by the infusion differ by about 43%.

Furthermore, we can observe that the difference is not limited to the distribution shape but there is also a marked different pattern of concentration profile. This is particularly evident in the second column of Fig. 5.5 which displays the GD concentration on a plane perpendicular to the catheter and with an offset of 1 mm with respect to the infusion point. Here, the maximum GD concentration of the model that integrates also NODDI is about two times

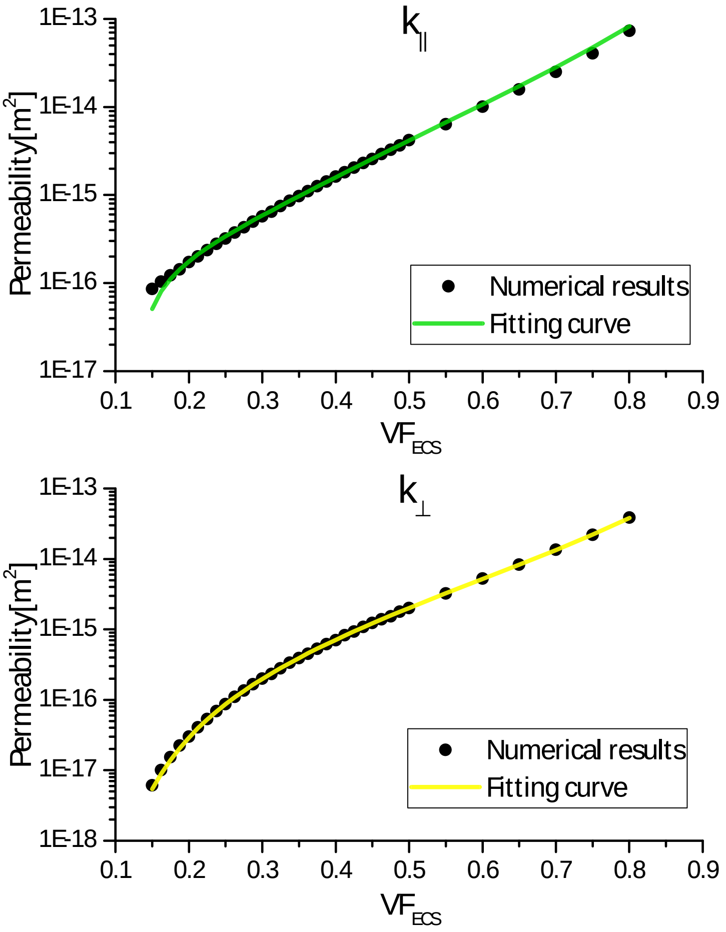

FIGURE 5.4: The parallel and perpendicular permeability returned by Eq. 5.9 and Eq. 5.10 after fitting the numerical results are plotted versus the VF_{ECS} in the top and bottom part of the figure, respectively.

the one of the model based only on DTI. Despite this being just a qualitative example, the difference between the models in terms of concentration will find confirmation in the quantitative analysis illustrated in the next section.

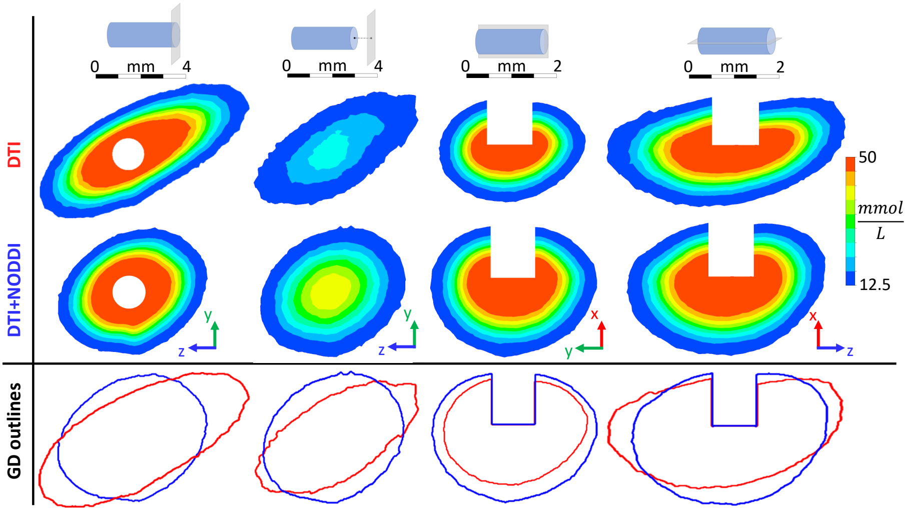

FIGURE 5.5: Predicted GD concentration after infusion in a WM region of the brain. Top: schematic drawing representing the catheter and the section plane corresponding to the contours below. Middle: GD concentration contours obtained with the DTI and the DTI-NODDI models at 180 seconds. Bottom: Comparison between the GD distribution outlines defined as the more external elements with a GD concentration higher than c_{min}.

5.3.3 Prediction of GD concentration

The analysis on drug concentration is summarized in Figure 5.6 which shows the average RMSD between the simulations performed with different orientations of the catheter. It is immediately possible to notice that the RMSD increases in time, going from a minimum about 12% to a maximum about 23%. Moreover, we can notice that the standard deviation is approximately constant across time even with different orientations of the catheter.

5.3.4 Prediction of GD distribution main direction and infusion penetration length

From the PCA, we obtained the main directions along which the drug has diffused for the DTI and DTI-NODDI models for each catheter orientation. The angular difference between these directions is defined by the angle θ. The

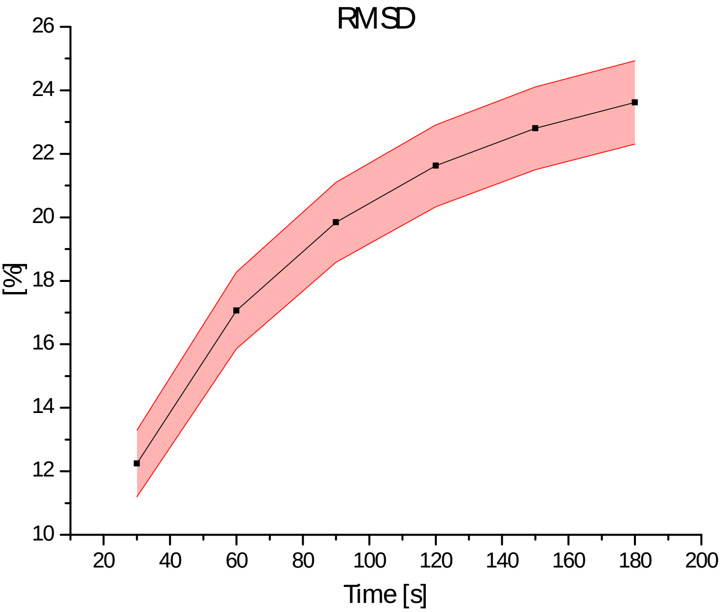

FIGURE 5.6: Variation of the RMSD between the two models in time (shown in terms of percentages). The figure shows the RMSD averaged between all the simulations at each time step (squared symbol). Since the data distribution at each time step is normal, the light red band indicates the standard deviation.

maximum difference in terms of θ is around 7.92 degrees, whereas the minimum one is around 0.95. However, the average is about 4.85 degrees with a standard deviation equal to 2.54 degrees. Since the data are normally distributed, a one-sided one-sample t-test was used to study the results. A p equal to $2.87 \cdot 10^{-4}$ demonstrates that θ is significantly different from zero.

Another interesting parameter to explore is the maximum linear penetration length (L_{max}) reached by the injected volumes, to analyse how deep in the tissue the drug can distribute. This parameter was defined calculating the maximal length (at 180 seconds) of the infusion volumes along the direction obtained with the PCA. The L_{max} values for the DTI and DTI-models for each catheter orientation were then compared using a two-sided paired t-test. The boxplot showed in Figure 5.7 brings evidence of a statistically significant difference between the two models ($p = 5 \cdot 10^{-9}$).

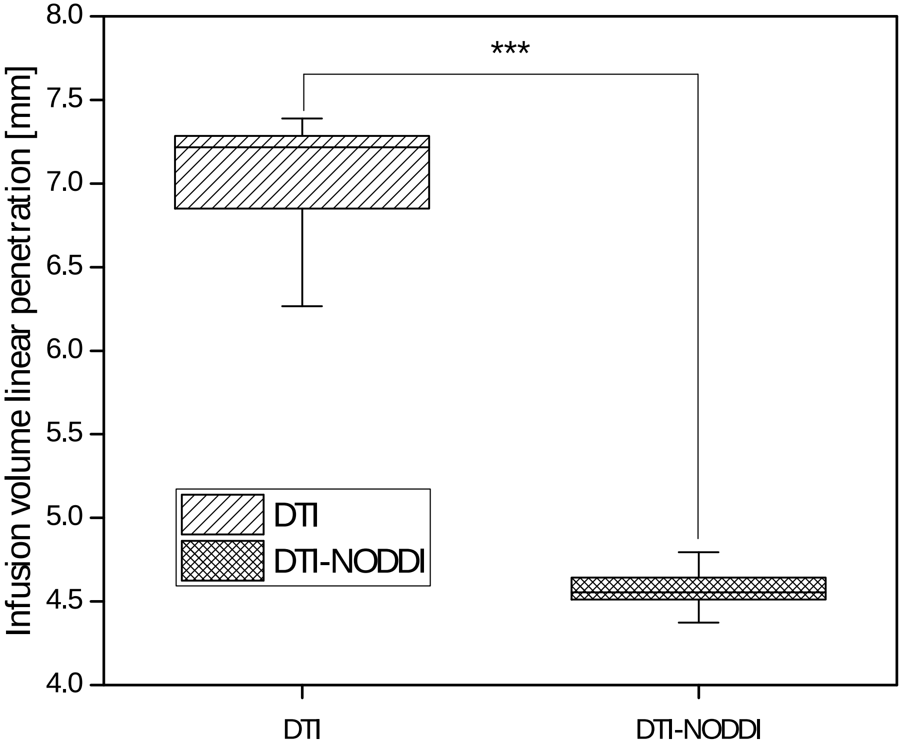

FIGURE 5.7: Boxplot comparing the infusion volume linear penetration length in the models. A two-sided paired t-test was performed to show the statistically significant difference between the models ($p = 5 \cdot 10^{-9}$).

5.4 Discussion

The proposed work comes from a relatively simple observation that was pointed out also in other studies (Nicholson and Hrabětová, 2017): when injecting a drug in the brain, the final outcome in terms of drug spreading depends on the microstructural organization of the neural tissue. This is due to the fact that a drug moves in the interstitial space between glial cells, neuron cell bodies and axons, whose tortuous paths influence the main directions the infusate can take (Vidotto, Dini, and De Momi, 2018). Accordingly, the common approach adopted by many researchers is to use DTI to model this aspect. However, DTI does not consider the VF_{ECS} which is directly related to the brain hydraulic permeability (Vidotto et al., 2019a).

To tackle this issue, we have developed a simplified geometrical model of the WM with the aim of defining a direct relation between the VF_{ECS} provided by the NODDI analysis and the hydraulic permeability. The model assumes that it is possible to describe the axons arrangement as an array of parallel and rigid cylinders with the same radius. Despite this is far from being a realistic description, it succeeded in providing an analytical expression which is in very good agreement with more comprehensive studies such as (Vidotto et al., 2019a; Franceschini et al., 2006) (Fig. 5.4). Therefore, we can confirm the soundness of our method and combine the NODDI and DTI analysis to characterize the anisotropic permeability tensor $\mathbf{K_{WM}}$.

To test the importance of including the input from NODDI in a CED predictive model, we compared our methodology with other important contributions from the state of the art (Dai et al., 2016; Kim et al., 2012; Kim, Mareci, and Sarntinoranont, 2010), where the values of WM permeability $k_{\|}$ and $k_{\perp}$, were considered constant across the brain tissue. To this end, we performed several analyses that were exhibited in the previous *Results* section.

At first, we conducted a qualitative analysis on the GD concentration contours (Fig. 5.5). By looking at different planes parallel and perpendicular with respect to the direction of the catheter, it is evident an important discrepancy both in terms of distribution shape and concentration. Moreover, the difference concerning the overall infused volume is about 43% meaning that there is a non-negligible impact on the brain area involved. This is particularly important in CED interventions for highly malignant brain tumors as GBM. Since this is a dramatically aggressive tumor with a very high recurrence rate, it is crucial that the drug reaches both the most motile and the innermost cellular component of the mass, to possibly contain the spreading of the tumor. Furthermore, note that despite Figure 5.5 provides an example for one simulation, these results are consistent also for all the other simulations independently from the catheter infusion directions shown in Figure 5.3.

As explained in the introduction, reaching all the cells affected by a certain disease is not enough, indeed, for the treatment to be effective, it is necessary to have a concentration of drug sufficiently high. Therefore, we analyzed the models in terms of RMSD which provides a quantitative feedback in terms of concentration difference (Fig. 5.6). Even in this case, the catheter orientation does not play a crucial role and the RMSD increases as a function of time reaching a maximum of 23%. Such an important discrepancy implies a potentially inaccurate prediction of the outcome of the delivered therapy. Moreover, we need to take into account that, usually, CED interventions last much more than 3 minutes or could even be chronically implanted in patient's brain, thus suggesting that the difference in concentration could raise even more.

Finally, we investigated the main direction that the drug takes when injected. Despite the angle θ between the two models is statistically different from zero, the difference about 4.85 degrees is not impressive. This is probably due to the fact that, in both models, the eigenvectors characterizing $\mathbf{K_{WM}}$ come from the same DTI dataset. On the other hand, comparing the infusion volume linear penetration length, we can notice a statistically significant difference which is about 3 mm (Fig. 5.7). This difference might seem small as an absolute number but as a percentage, it shows that the DTI model predicts a linear penetration length increase of more than 50%. Since in brain surgery errors in the order of millimetres are not negligible, this analysis also supports the importance of using the right numerical model.

The proposed approach has two limitations which will be tackled in future developments. The first concerns the relation between the VF_{ECS} and the hydraulic permeability. In fact, it was derived only for the WM, where the fibres tend to be highly aligned forming bundles, because GBM tends to infiltrate and derange WM tracts. However, to have a more complete model, a relation also for the GM should be derived. Moreover, a more complex geometrical model for the WM could be used. The second limitation is given by the fact that our model needs to be validated with proper in-vivo or ex-vivo tests.

5.5 Conclusion

Concluding, we presented an innovative model for predicting the drug distribution in brain tissues for CED application. The main element of novelty comes from the idea to characterize the permeability tensor combining both

DTI and NODDI images from the same subject, used as representative case-scenario. In fact, DTI allows distinguishing WM and GM regions and determining the orientation of the neural fibres within each voxel whereas NODDI provides information relative to the VF_{ECS}. By tailoring this fundamental information about the microstructure with a simplified geometrical model of the WM, we were able to assign anisotropic permeability values depending on the fibres' directionality to each voxel. The results analysed in terms of distribution shape, concentration and infusion linear penetration length show significant differences with respect to previous models only based on DTI. Specifically, the DTI model tends to overestimate the drug distribution with respect to our model. This phenomenon was detected also by Kim et al., 2012 by comparing their prediction with in vivo experiments on rat brain.

The proposed approach makes an important step further in CED modelling introducing a more comprehensive way to describe the permeability tensor. We believe that further studies, in which the brain microstructure plays a key role, could lead to a deeper understanding of the relation between modelling parameters and non-invasive imaging modality like NODDI. Indeed, despite detailed analyses of the neural tissue at the microscale are necessary and provides invaluable results, it is only by integrating this kind of studies with clinically feasible imaging modalities that we will be able to provide the surgeons with more effective predictive tools.

Appendix

The grid sensitivity analysis is an important step to find a good trade-off between reducing the discretization error and the computational cost of the simulation. Accordingly, we examined several grids for each numerical model developed in this research.

First, we performed a sensitivity analysis on the geometrical models described in section Geometrical model whose objective was computing $k_{\parallel}$ and $S_{\perp}$ as a function of the VF_{ECS}. For both geometries, we compared 11 grids with an increasing number of nodes achieved varying the edges discretization

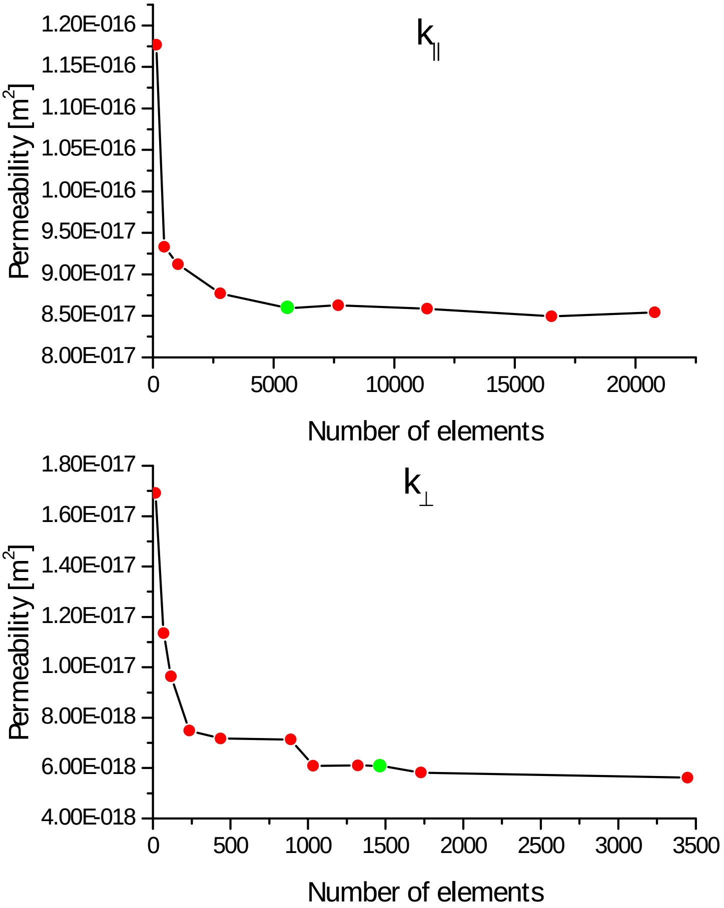

FIGURE 5.8: Sensitivity analysis performed on the grid of the geometrical models for both $k_{\parallel}$ and $k_{\perp}$ with VF_{ECS} equal to 0.15. The green marker indicates the number of elements for the mesh chosen for running all the simulations.

and the maximum face size. Since we performed the analysis on the geometries with VF_{ECS} equal to 0.15 that are the most difficult to discretize due to the proximity of the axons, we assume that the same discretization parameter would fit also the geometries with higher VF_{ECS}. The results of the sensitivity analysis are shown in Figure 5.8, the green marker indicates the number of elements for the mesh chosen for running all the simulations.

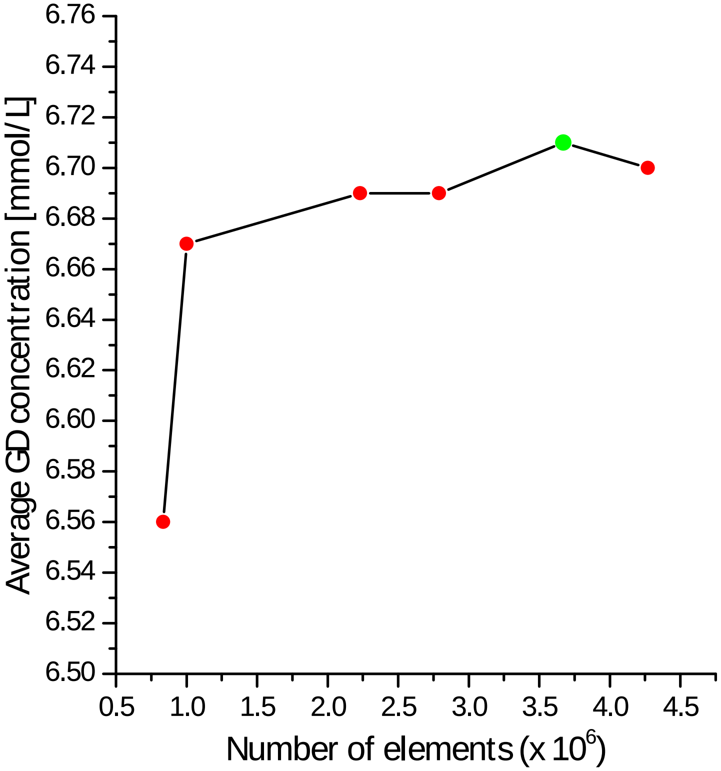

FIGURE 5.9: Sensitivity analysis performed on the grid of the geometrical models for both $k_{||}$ and $k_{\perp}$ with VF_{ECS} equal to 0.15. The green marker indicates the number of elements for the mesh chosen for running all the simulations.

Similarly to what has been already described, we performed a sensitivity analysis also on the CED model varying, in particular, the discretization of the catheter edges in proximity of the inlet and the maximum dimension of the tetrahedral elements in the brain. As it is possible to notice from Figure 5.9, these simulations are intrinsically expensive because of the large number of elements. For this reason, for the sensitivity analysis only, we performed steady state simulations testing 6 different grids. We compare the simulations computing the average GD concentration in the elements comprised in a sphere (radius equal to 3 mm) centred in the centre of the catheter inlet. The sphere radius was chosen empirically to include a representative portion of the brain interest by the GD injection.

Acknowledgments

This work was supported by EDEN2020, a project funded by the European Union's H2020 Research and Innovation Programme under the grant agreement No. 688279.

Chapter 6

Conclusions

This PhD thesis investigated the role played by brain tissue microstructure in relation to transport of drugs in Convection-Enhanced Delivery (CED) interventions. The final aim was the development of a predictive numerical model to help the surgeon to accurately plan the surgery.

Recently, CED has been introduced as a promising surgical technique to bypass the BBB and inject a chemotherapeutic agent directly in the brain tissue (Jahangiri et al., 2016). Despite this technique was expected to be effective especially against recurrent tumors, the clinical trials failed to meet the desired results in terms of life expectancy for the patients (Kunwar et al., 2010). Clearly, it is not easy to pinpoint a unique cause for this failure but many factors can contribute to the final outcome of this therapy. One of them, is the incapability to reach all the cancerous areas with a sufficiently high concentration of drug. Indeed, since the brain is an anisotropic and heterogeneous porous medium, for the clinicians it is often difficult to set the infusion in the best way possible.

For this reason, researchers have worked on predictive numerical models that can offer the surgeons a simulation environment to test different infusion settings. Despite these models, summarized in Table 1.1, have offered an extremely valuable contribution to this research field, their predictive capability is still not sufficiently accurate. Indeed, few of them have found a way towards a market application. Therefore, Vendel, Rottschäfer, and Lange, 2019 pointed out the paramount importance of having refined mathematical models on the spatial drug distribution within the brain. Moreover, Nicholson and Hrabětová, 2017 and Holter et al., 2017 underlined the pivotal role of the brain microstructure in driving convection and diffusion of drug in the neural tissue. This aspect, in particular, has been explored by limited researches and the relation between tissue microstructure and important fluid dynamics parameters is still controversial.

To this end, in the first part of Chapter 2, we used a model built considering the main geometrical characteristics of the white matter (WM) and we extracted two important information, a first estimate of the hydraulic permeability in three areas and the size of the representative volume element (RVE) to analyse to have reliable results. This geometrical model was also exploited in the second part of Chapter 2, with a different methodological approach, to study the WM tortuosity, a very important parameter for drug diffusion that surely deserves further research. In Chapter 3, we designed an ideal scenario that starts from the segmentation of the real WM microstructure from EM images and finish with the computation of the hydraulic permeability on a RVE whose size was defined in Chapter 2. Despite we had to perform the segmentation manually instead of automatically, in the second part of Chapter 3, we demonstrated and quantified the anisotropic and heterogeneous behaviour of the WM. These results were validated in Chapter 4 by means of an experimental campaign on ovine WM samples. Finally, in Chapter 5, the information about the WM permeability, acquired in the previous studies, were integrated in a comprehensive CED predictive model.

6.1 Thesis contributions

This PhD research focuses on the analysis of the brain microstructure as a way to estimate important constitutive parameters of the brain. The later are fundamental for the development of accurate CED predictive model that can help the clinicians to plan the surgical intervention. Note that, despite studying the brain microstructure is not possible for every patient, the Neurite Orientation Dispersion and Density Imaging (NODDI) analysis used in Chapter 5 allows bridging the gap between our studies and a clinically feasible imaging modality.

To understand the role of the microstructure in driving the convective and diffusive flux of drug molecules, the first step was identifying the brain sample size to analyse to get reliable results. To do that, in the first part of Chapter 2, we build a geometrical model of the WM considering the main structural information available in the literature. Using a computational fluid dynamics approach, we computed the pressure and velocity fields and subsequently, the WM permeability. Despite this geometrical model makes use of some simplifying assumptions, it is based on a sounding methodology which ensures reliable results. In particular, the model includes ECS volume fraction and ECS width as main input parameters that were compared with the experimental data. Moreover, we verified that the spatial organization of our axons, modelled as cylinders, was in complete agreement with the complete spatial randomness found in the real axons. Note that ensuring the homogeneity of the porous media along all the length scales considered is fundamental to estimate the RVE size. For all the structures analysed (corpus callosum, superior and inferior fascicles), we identified a RVE characterized by a length scale of about 15-17 μm. The corresponding values of permeability range in the orders of 10^{-16} m^2 which is in very good agreement with our findings in Chapter 3 and Chapter 4. This result is particularly important because of the large uncertainty in the estimate of this parameter that, despite its importance, in the literature can vary up to three orders of magnitude (Vidotto et al., 2019a)[1]. Moreover, it paves the way to the use of non-invasive *in vivo* imaging techniques instead of the expensive *ex vivo* EM imaging. This point will be further discuss in the Future Perspective section.

In the second part of Chapter 2, we used a three-dimensional version of the geometrical model developed in the first part of the chapter to inspect another parameter named tortuosity. In the specific application of CED, tortuosity is less important than permeability because it concerns the diffusive part of the flux which is secondary with respect to the convective one. Nonetheless, it is a fundamental parameter that measures the hindrance offered by the ECS to the diffusion of drug molecules. To this end, we implemented a Monte Carlo based simulation: the main idea was to release a certain number of molecules

---

[1] Vidotto, Marco et al. (2019a). "A computational fluid dynamics approach to determine white matter permeability". In: *Biomechanics and modeling in mechanobiology*, pp. 1–12.

in the center of the volume and then to measure their diffusion in time. Fitting the simulation data with an *ad hoc* function, it was then possible to compute a value of tortuosity parallel and perpendicular with respect to the direction of the axons. Parallel tortuosity was constantly equal to 1. This result, meaning no hindrance, proves the soundness of the method being in complete agreement with what was expected theoretically. On the other hand, perpendicular tortuosity increases as the ECS volume fraction and the ECS width decrease. This is due to the fact that, the more the axons are close one to each other and the more for the molecules it is difficult to move between them. The findings highlighted in this chapter helps to shed light on this parameter and its relation with the ECS microstructure (Vidotto, Dini, and De Momi, 2018)[2].

In Chapter 3, we designed an ideal workflow to study the WM microstructure that starts with the EM images analysis and finishes with the extraction of relevant parameters. Accordingly, we developed a fully convolutional neural network (FCNN) to segment the axons' boundaries starting from EM images. The algorithm, tested on a publicly available dataset, shows performances comparable with the state of the art but with a much lower training time. Moreover, despite some errors in the segmentation are present, the achieved ADD is in strong agreement with that obtained with time-expensive manual tracing (no statically significant difference). Therefore, in the event that the ADD is used to build a geometrical model as in Chapter 2, the achieved segmentation performances are appropriate for the purpose (Vidotto et al., 2019b)[3]. On the other hand, if the objective is to perform a direct study on the microstructure without using any model, our algorithm did not demonstrate enough robustness thus suggesting the need for more sample images to tackle the high data variability.

For this reason, in the second part of Chapter 3, it was necessary to perform a manual segmentation on the ovine brain WM EM images that we acquired in collaboration with Imperial College of London and Università Statale of

---

[2] Vidotto, Marco et al. (2018). "Effective diffusion and tortuosity in brain white matter". In: *2018 40th Annual International Conference of the IEEE Engineering in Medicine and Biology Society (EMBC)*. IEEE, pp. 4901–4904.

[3] Vidotto, Marco et al. (2019b). "FCNN-based axon segmentation for convection-enhanced delivery optimization". In: *International journal of computer assisted radiology and surgery*. 14.3, pp. 493–499.

Milan. Since the images were quite noisy and blurred, a manual tracing was the only way to distinguish, precisely, between the intra-cellular space and the ECS. We analysed 20 slices for each one of the two volumes available, corpus callosum and fornix, belonging to the same animal. On each slice, we computed the velocity and pressure fields using a CFD approach and, subsequently, the hydraulic permeability using Darcy's law. Note that, the later was computed on the EM imaging planes which are randomly oriented. To obtain a more meaningful result, we exploited the certerline of each axon (Bernardini et al., N.D.) to conduct a principal component analysis. This analysis allowed defining the axons principal direction and, assuming that the WM can be described as transversely isotropic porous medium, the direction perpendicular to them. Finally, we projected the permeability values, previously computed on the imaging planes, onto the parallel and perpendicular directions. For both corpus callosum and fornix, the results show a statistically significant difference between permeability in the parallel and perpendicular directions. This contribution is particularly important because it demonstrates and quantifies the anisotropic properties of the WM starting from the real microstructure of the fibers. Moreover, we found a statistically significant difference also between the parallel permeability values and the perpendicular permeability values computed in the corpus callosum and in the fornix. This last analysis suggests that the brain is an heterogeneous porous medium even if we look at WM areas only (Vidotto, De Momi, and Dini, N.D.)[4]. Therefore, it is clear that a simple division between WM and GM is not enough and a further in-depth analysis is needed. We partially address this issue in Chapter 5 where we try to build a CED model with a voxel by voxel estimate of the permeability tensor.

In Chapter 4, we conducted an experimental campaign in collaboration with Imperial College London. The objective of this work was to verify that

---

[4] Vidotto, Marco et al. (N.D.). "White matter microstructure role for hydraulic permeability: a new electron microscopy images based approach". To be submitted to *Proceedings of the National Academy of Sciences*.

the hydraulic permeability values obtained in Chapter 2 and 3 were consistent with an experimental validation. Moreover, we were interested in understanding the effect of local microstructural features on hydraulic permeability. To address this issue, at first we excised cylindrical samples (7-8 mm thickness by 5 mm diameter) from slices of fresh ovine brain (within 24 hours post-mortem) and we inserted them in a phosphate-buffered saline. Then, we exploited an infusion based experimental set up (*iPerfusion*) to derive the flow-pressure relationship in WM samples. The results show that samples having the axons parallel to the flow direction have a mean hydraulic permeability value which is significantly higher than when axons are perpendicular to the direction of the flow. These results clearly demonstrate that the intrinsic anisotropy of the WM strongly influences the resistance to the flow across the tissue. Moreover, the average values of permeability are in good agreement with the results obtained in Chapter 2 and Chapter 3. Also, we analysed the pressure dependence of hydraulic permeability thus revealing a non-linear relationship which is significant in the parallel samples and mildly significant in case of perpendicular samples. This is probably due to the local tissue deformation that, dealing with soft tissue, is almost impossible to avoid. Finally, we show that there is no statistical correlation between hydraulic permeability and post-mortem time up to 11 hours (Jamal et al., N.D.)[5].

Finally, in Chapter 5, we move from the microstructural analysis on the WM axons to a comprehensive drug delivery model at the macroscale. In this model, our objective was to integrate the information acquired in the previous chapters with a clinically acceptable imaging technique. Indeed, despite EM imaging is extremely useful, it is very difficult to perform, it requires a great amount of time, it can be managed only by expert operators and, most importantly, it cannot be done on living patients. To tackle this issue, we introduced a new imaging technique, namely NODDI, in drug delivery modelling that combines the capability to infer microstructural features with the possibility to acquire the images in a standard time frame. We exploited one of the parameter that can be extracted from NODDI, the ECS volume fraction, to

---

[5] Jamal, Asad et al. (N.D.). "Infusion mechanisms in brain white matter and its dependence of microstructure: an experimental study of hydraulic permeability". Under review in *IEEE Transaction of Biomedical Engineering*.

characterize the permeability tensor. Modelling the axons as straight parallel cylinders and varying the distance between them, it was possible to find a relation between the ECS volume fraction and permeability in the parallel and perpendicular directions. Then, we combined this information with DTI, another imaging technique from which it is possible to understand the principal direction of the axons and, accordingly, the direction perpendicular to them. Using both DTI and NODDI in the same model represents a step change with respect to the state of the art models where only DTI is included. To demonstrate the relevance of our work, we compared our model (*DTI-NODDI model*) with a state-of-the-art model (*DTI model*). In both models, we injected a GD solution for 3 minutes in a WM areas with different orientation of the catheters. The results show a marked difference between the models GD distribution in terms of concentration profiles and infusion volume shapes. Indeed, we display that the concentration difference (expressed as RMSD) increases until 23% in only 180 seconds and there is a statistically significant difference in terms of infusion volume penetration length and distribution principal direction. Concluding, the novelty introduced by our model to characterize the permeability tensor combining both DTI and NODDI, has proved itself to be decisive. We believe that the proposed approach represents an important step further in CED modelling introducing a more comprehensive way to describe the permeability tensor and its relationship with the microstructure (Vidotto et al., N.D.)[6].

The overall results highlight the benefit of achieving an in-depth knowledge of the brain microstructure. Indeed, studying the geometrical organization of the axons, it is possible to determine parameters that, despite their crucial role, are still affected by important uncertainties. Different approaches can offer distinct contribution and insights into the factors that drives the drug transport in the brain tissue. Moreover, integrating the information gained studying the microstructure in a drug delivery model could lead to a more comprehensive predictive capability that in turn could benefit the clinicians and the patients.

---

[6] Vidotto, Marco et al. (N.D.). “Advanced imaging methods to improve the predictive capabilities of CED models”. Under second review in *Annals of Biomedical Engineering*.

6.2 Future perspective

In the near future, modern medicine will most likely look at a more and more personalized medicine which relies on advanced technological tools to help the healthcare personnel to ameliorate their performances. Neurosurgery is no exception and the fact that the brain is such a complex environment, makes it an ideal framework where technology can play an important role.

In this scenario, the proposed work represents a portion of a wider research field that aims at understanding the mechanisms related to drug distribution in the brain in their entirety and in a perspective that goes beyond the objective of this thesis (Vendel, Rottschäfer, and Lange, 2019). In this research, we focus our attention on CED, an innovative surgical technique that, despite being promising, has not succeeded in increasing the patients life expectancy when dealing with aggressive tumors such as GBM (Jahangiri et al., 2016).

In order to enhance CED performances, we believe that providing the surgeons with a computational tool able to predict the drug distribution in the brain could represent a step change in the treatment outcomes. Indeed, in this way, in the pre-operative phase the surgeon would be allowed testing different catheters and infusion parameters and then decide the best way to proceed. However, a predictive model to be effective should have two important characteristics: it should be very accurate in predicting the drug distribution and it should be feasible in a clinical scenario meaning that the time necessary for the imaging and for running the simulations must be in line with the healthcare system standards.

In this sense, we put considerable efforts into making the model more accurate by deepening our understanding of the relation between the brain microstructure and important constitutive parameters such as hydraulic permeability and tortuosity. To do that, in Chapter 2, we built a geometrical model of the WM based on the ADD and, with different approaches, we estimated the WM permeability and tortuosity in the direction perpendicular to the main direction of the axonal fibers. Note that in our case, the ADD data came from EM images that, despite being very accurate, require a great amount of time to be acquired and processed (Liewald et al., 2014). A viable alternative is given by MRI methods based on double diffusion encoding though which it is possible to estimate and map the ADD within an imaging volume (Benjamini et al., 2016). Unfortunately, also the MRI approach has two important limitations: it relies on strong prior assumptions on the axon spatial organization and the acquisition time is about 40 hours which is obviously not feasible for a standard clinical analysis. Nevertheless, it is surely an interesting path to further explore in the future.

In Chapter 2, we highlighted also the fact that the lack of information about how the axons develop longitudinally precludes the possibility to compute permeability and tortuosity in the parallel direction. It is our opinion that more researches should aim at unveiling this aspect of the axons morphology at the microscale level. Our contribution in Chapter 3 represents a first attempt in this direction. In Chapter 3, we developed a FCNN to automatically segment the axons from two-dimensional EM images and in the second part, we computed the anisotropic permeability tensor starting from the same kind of images. Despite we obtained important results, it is evident the need for larger data sets of annotated images to be used either to train FCNNs either to compute the hydraulic permeability on more WM and GM areas.

In Chapter 4, we performed an experimental campaign on two WM structures to validate our numerical results. Even in this case, it would be interesting to extend our analysis to more WM and GM areas. Moreover, it would be interesting to deepen the pressure-permeability relationship which is surely an important aspect not only for CED modeling but also for brain trauma induced pathologies.

Finally, in Chapter 5, we built a comprehensive CED predictive model integrating the information about the brain microstructure with a patient specific MRI sequence that is feasible in a standard clinical scenario. Despite we demonstrated the relevance of our approach with respect to the state of art, we still need to validate our model with proper *ex-vivo* or *in-vivo* tests. Moreover, we conducted our study on a healthy subject but the presence of brain pathologies would surely influence the hydrodynamics parameters. To face this issue, we are currently collaborating with Imperial College London and Università Statale Milano to analyse cancerous tissue samples through EM imaging. Understanding how the microstructure is altered by the disease can help inferring its effect on the relevant modelling parameters.

Bibliography

Abbott, N Joan (2004). “Evidence for bulk flow of brain interstitial fluid: significance for physiology and pathology”. In: *Neurochemistry international* 45.4, pp. 545–552.

Abdi, Hervé and Lynne J Williams (2010). “Principal component analysis”. In: *Wiley interdisciplinary reviews: computational statistics* 2.4, pp. 433–459.

Abdollahzadeh, Ali et al. (2019). “Automated 3D axonal morphometry of white matter”. In: *Scientific reports* 9.1, pp. 1–16.

Abolfathi, Naik et al. (2009). “A micromechanical procedure for modelling the anisotropic mechanical properties of brain white matter”. In: *Computer Methods in Biomechanics and Biomedical Engineering* 12.3, pp. 249–262.

Agnati, Luigi F, Börje Bjelke, and Kjell Fuxe (1992). “Volume transmission in the brain”. In: *American Scientist* 80.4, pp. 362–373.

Alexander, Andrew L et al. (2007). “Diffusion tensor imaging of the brain”. In: *Neurotherapeutics* 4.3, pp. 316–329.

Alexander, Daniel C et al. (2019). “Imaging brain microstructure with diffusion MRI: practicality and applications”. In: *NMR in Biomedicine* 32.4, e3841.

Alphandéry, Edouard (2018). “Glioblastoma treatments: an account of recent industrial developments”. In: *Frontiers in pharmacology* 9, p. 879.

Andres, Björn et al. (2008). “Segmentation of SBFSEM volume data of neural tissue by hierarchical classification”. In: *Joint Pattern Recognition Symposium*. Springer, pp. 142–152.

ANSYS (2017). *ANSYS Fluent Theory Guide*. ANSYS.

Arganda-Carreras, Ignacio et al. (2015). “Crowdsourcing the creation of image segmentation algorithms for connectomics”. In: *Frontiers in Neuroanatomy* 9, p. 142.

Arifin, Davis Yohanes et al. (2009). "Role of convective flow in carmustine delivery to a brain tumor". In: *Pharmaceutical research* 26.10, pp. 2289–2302.

Asgari, Mahdi, Diane De Zélicourt, and Vartan Kurtcuoglu (2016). "Glymphatic solute transport does not require bulk flow". In: *Scientific reports* 6, p. 38635.

Ballabh, Praveen, Alex Braun, and Maiken Nedergaard (2004). "The blood–brain barrier: an overview: structure, regulation, and clinical implications". In: *Neurobiology of disease* 16.1, pp. 1–13.

Barua, N. U. et al. (2013). "Robot-guided convection-enhanced delivery of carboplatin for advanced brainstem glioma". In: *Acta Neurochirurgica* 155.8, pp. 1459–1465. ISSN: 00016268.

Barua, Neil U et al. (2014). "A novel implantable catheter system with transcutaneous port for intermittent convection-enhanced delivery of carboplatin for recurrent glioblastoma." In: *Drug delivery* 7544.July 2017, pp. 1–7. ISSN: 1521-0464.

Barua, Neil U et al. (2016). "A novel implantable catheter system with transcutaneous port for intermittent convection-enhanced delivery of carboplatin for recurrent glioblastoma". In: *Drug Delivery* 23.1, pp. 167–173.

Basser, J. Peter (1992). "Interstitial Pressure , Volume, and Flow during Infusion into Brain Tissue". In: *Microvasc Res* 165.2, pp. 143–165.

Basser, Peter J and Carlo Pierpaoli (1996). "Microstructural and physiological features of tissues elucidated by quantitative-diffusion-tensor MRI". In: *Journal of magnetic resonance, Series B* 111.3, pp. 209–219.

Beier, Thorsten et al. (2017). "Multicut brings automated neurite segmentation closer to human performance". In: *Nature Methods* 14.2, p. 101.

Benjamini, Dan et al. (2016). "White matter microstructure from nonparametric axon diameter distribution mapping". In: *NeuroImage* 135, pp. 333–344.

Bernardini, A et al. (N.D.). "Imaging and reconstruction of the cytoarchitecture of axonal fibres: enabling biomedical engineering studies involving brain microstructure". To be submitted to *Nature Biomedical Engineering*.

Bobo, R Hunt et al. (1994). "Convection-enhanced delivery of macromolecules in the brain". In: *Proceedings of the National Academy of Sciences* 91.6, pp. 2076–2080.

Boucher, Y et al. (1998). "Intratumoral infusion of fluid: estimation of hydraulic conductivity and implications for the delivery of therapeutic agents". In: *British journal of cancer* 78.11, pp. 1442–1448.

Buckner, Jan C et al. (2007). "Central nervous system tumors". In: *Mayo Clinic Proceedings*. Vol. 82. 10. Elsevier, pp. 1271–1286.

Bush, Nancy Ann Oberheim, Susan M Chang, and Mitchel S Berger (2017). "Current and future strategies for treatment of glioma". In: *Neurosurgical review* 40.1, pp. 1–14.

Cai, Dingding et al. (2017). "Convolutional low-resolution fine-grained classification". In: *Pattern Recognition Letters*.

Caverzasi, Eduardo et al. (2016). "Neurite orientation dispersion and density imaging color maps to characterize brain diffusion in neurologic disorders". In: *Journal of Neuroimaging* 26.5, pp. 494–498.

Chen, Kevin C and Charles Nicholson (2000). "Changes in brain cell shape create residual extracellular space volume and explain tortuosity behavior during osmotic challenge". In: *Proceedings of the National Academy of Sciences* 97.15, pp. 8306–8311.

Chen, Xiaoming and TD Papathanasiou (2007). "Micro-scale modeling of axial flow through unidirectional disordered fiber arrays". In: *Composites Science and Technology* 67.7-8, pp. 1286–1293.

Chen, Xiaoming and Thanasis D Papathanasiou (2008). "The transverse permeability of disordered fiber arrays: a statistical correlation in terms of the mean nearest interfiber spacing". In: *Transport in Porous Media* 71.2, pp. 233–251.

Chen, Xiaoming and Malisa Sarntinoranont (2007). "Biphasic finite element model of solute transport for direct infusion into nervous tissue". In: *Annals of Biomedical Engineering* 35.12, pp. 2145–2158. ISSN: 00906964.

Christine, Chadwick W et al. (2019). "Magnetic resonance imaging–guided phase 1 trial of putaminal AADC gene therapy for Parkinson's disease". In: *Annals of neurology* 85.5, pp. 704–714.

Ciresan, Dan et al. (2012). "Deep neural networks segment neuronal membranes in electron microscopy images". In: *Advances in Neural Information Processing Systems*, pp. 2843–2851.

Crawford, Lindsey, Justin Rosch, and David Putnam (2016). "Concepts, technologies, and practices for drug delivery past the blood-brain barrier to the central nervous system". In: *Journal of Controlled Release* 240, pp. 251–266. ISSN: 18734995.

Dai, Wei et al. (2016). "Voxelized model of brain infusion that accounts for small feature fissures: comparison with magnetic resonance tracer studies". In: *Journal of biomechanical engineering* 138.5.

Darcy, Henry (1994). "Darcy's Law". In: *Ground Water* 32.1, pp. 23–30. ISSN: 19432909.

Datta, AK (2006). "Hydraulic permeability of food tissues". In: *International Journal of Food Properties* 9.4, pp. 767–780.

Davis, Mary Elizabeth (2016). "Glioblastoma: overview of disease and treatment". In: *Clinical journal of oncology nursing* 20.5, S2.

Debinski, Waldemar and Stephen B Tatter (2009). "Convection-enhanced delivery for the treatment of brain tumors". In: *Expert review of neurotherapeutics* 9.10, pp. 1519–1527.

Dias, M. R. et al. (2012). "Permeability analysis of scaffolds for bone tissue engineering". In: *Journal of Biomechanics* 45.6, pp. 938–944. ISSN: 00219290.

Diggle, Peter J (2003). "Statistical analysis of spatial point patterns." In: *New York* 171.2, p. 159. ISSN: 0956540X.

Ding, Dale et al. (2010). "Convection-enhanced delivery of free gadolinium with the recombinant immunotoxin MR1-1". In: *Journal of neuro-oncology* 98.1, pp. 1–7.

Dixon, Philip M. (2002). "Ripley's K Function". In: *Wiley StatsRef: Statistics Reference Online* 3, pp. 1796–1803. ISSN: 0470057335.

Drugan, W J and J R Willis (1996). "A Micromechanics-Based Nonlocal Constitutive Equation and Estimates of Representative Volume Element Size for Elastic Composites". In: *Journal of the Mechanics and Physics of Solids*.

Du, X and M Ostoja-Starzewski (2006). "On the size of representative volume element for Darcy law in random media". In: *Proceedings of the Royal Society A: Mathematical, Physical and Engineering Sciences* 462.2074, pp. 2949–2963. ISSN: 1364-5021.

Dullien, Francis AL (2012). *Porous media: fluid transport and pore structure*. Academic press.

Dunn, Laurence T (2002). "Raised intracranial pressure". In: *Journal of Neurology, Neurosurgery & Psychiatry* 73.suppl 1, pp. i23–i27.

Duval, Tanguy, Nikola Stikov, and Julien Cohen-Adad (2016). "Modeling white matter microstructure". In: *Functional neurology* 31.4, p. 217.

Ehlers, Wolfgang and Arndt Wagner (2015). "Multi-component modelling of human brain tissue: a contribution to the constitutive and computational description of deformation, flow and diffusion processes with application to the invasive drug-delivery problem". In: *Computer Methods in Biomechanics and Biomedical Engineering* 18.8, pp. 861–879.

Eshghinejadfard, Amir et al. (2016). "Calculation of the permeability in porous media using the lattice Boltzmann method". In: *International Journal of Heat and Fluid Flow* 1329.0, pp. 0–1. ISSN: 0142727X.

Etame, Arnold B et al. (2012). "Focused ultrasound disruption of the blood-brain barrier: a new frontier for therapeutic delivery in molecular neurooncology". In: *Neurosurgical focus* 32.1, E3.

Ethier, C Ross (1991). "Flow through mixed fibrous porous materials". In: *AIChE journal* 37.8, pp. 1227–1236.

Fakhry, Ahmed, Hanchuan Peng, and Shuiwang Ji (2016). "Deep models for brain em image segmentation: Novel insights and improved performance". In: *Bioinformatics* 32.15, pp. 2352–2358. ISSN: 14602059.

Feng, Y. T., K. Han, and D. R J Owen (2003). "Filling domains with disks: An advancing front approach". In: *International Journal for Numerical Methods in Engineering* 56.5, pp. 699–713. ISSN: 00295981.

Forte, AE et al. (2014). "A Novel Composite Phantom for Brain Tissue". In: *Annual International IEEE EMBS Conference*.

Forte, Antonio E. et al. (2016). "A composite hydrogel for brain tissue phantoms". In: *Materials and Design* 112, pp. 227–238. ISSN: 18734197.

Franceschini, G. et al. (2006). "Brain tissue deforms similarly to filled elastomers and follows consolidation theory". In: *Journal of the Mechanics and Physics of Solids* 54.12, pp. 2592 –2620. ISSN: 0022-5096.

García, José J, Ana Belly Molano, and Joshua H Smith (2013). "Description and validation of a finite element model of backflow during infusion into a brain tissue phantom". In: *Journal of Computational and Nonlinear Dynamics* 8.1.

Garo, A et al. (2007). "Towards a reliable characterisation of the mechanical behaviour of brain tissue: the effects of post-mortem time and sample preparation". In: *Biorheology* 44.1, pp. 51–58.

Gebart, B Rikard (1992). "Permeability of unidirectional reinforcements for RTM". In: *Journal of composite materials* 26.8, pp. 1100–1133.

Geer, Carol P and Stuart A Grossman (1997). "Interstitial fluid flow along white matter tracts: a potentially important mechanism for the dissemination of primary brain tumors". In: *Journal of neuro-oncology* 32.3, pp. 193–201.

Gopi, ES (2007). *Algorithm collections for digital signal processing applications using Matlab*. Springer Science & Business Media.

Goriely, Alain et al. (2015). "Mechanics of the brain: perspectives, challenges, and opportunities". In: *Biomechanics and Modeling in Mechanobiology* 14.5, pp. 931–965. ISSN: 16177940.

Gu, Wei Yong and Hai Yao (2003). "Effects of hydration and fixed charge density on fluid transport in charged hydrated soft tissues". In: *Annals of biomedical engineering* 31.10, pp. 1162–1170.

Hanif, Farina et al. (2017). "Glioblastoma Multiforme: A Review of its Epidemiology and Pathogenesis through Clinical Presentation and Treatment". In: *Asian Pacific Journal of Cancer Prevention* 18.1, p. 3.

Hansson, Kristin, Mehrdad Jafari-Mamaghani, and Patrik Krieger (2013). "RipleyGUI: software for analyzing spatial patterns in 3D cell distributions." In: *Frontiers in neuroinformatics* 7.April, p. 5. ISSN: 1662-5196.

Haralick, Robert M. and Linda G. Shapiro (1992). *Computer and Robot Vision*. 1st. Boston, MA, USA: Addison-Wesley Longman Publishing Co., Inc. ISBN: 0201569434.

Harder, Bryan G et al. (2018). "Developments in blood-brain barrier penetrance and drug repurposing for improved treatment of glioblastoma". In: *Frontiers in oncology* 8, p. 462.

He, Kaiming et al. (2016). "Deep residual learning for image recognition". In: *IEEE Conference on Computer Vision and Pattern Recognition*, pp. 770–778.

Heneghan, Paul and Philip E Riches (2008). "Determination of the strain-dependent hydraulic permeability of the compressed bovine nucleus pulposus". In: *Journal of Biomechanics* 41.4, pp. 903–906.

Hitti, K., S. Feghali, and M. Bernacki (2016). "Permeability computation on a Representative Volume Element (RVE) of unidirectional disordered fiber arrays". In: *Journal of Computational Mathematics* 34.3, pp. 246–264. ISSN: 02549409.

Holter, Karl Erik et al. (2017). "Interstitial solute transport in 3D reconstructed neuropil occurs by diffusion rather than bulk flow". In: *Proceedings of the National Academy of Sciences* 114.37, pp. 9894–9899. ISSN: 0027-8424.

Hrabe, Jan, Sabina Hrabětová, and Karel Segeth (2004). "A Model of Effective Diffusion and Tortuosity in the Extracellular Space of the Brain". In: *Biophysical Journal* 87.3, pp. 1606–1617. ISSN: 00063495.

Hrabětová, Sabina and Charles Nicholson (2004). "Contribution of dead-space microdomains to tortuosity of brain extracellular space". In: *Neurochemistry international* 45.4, pp. 467–477.

Hynynen, Kullervo et al. (2006). "Focal disruption of the blood–brain barrier due to 260-kHz ultrasound bursts: a method for molecular imaging and targeted drug delivery". In: *Journal of neurosurgery* 105.3, pp. 445–454.

Iacob, Gabriel and Eduard B Dinca (2009). "Current data and strategy in glioblastoma multiforme". In: *Journal of Medicine and Life* 2.4, p. 386.

Jafari-Mamaghani, Mehrdad (2010). "Spatial point pattern analysis of neurons using Ripley's K-function in 3D". In: *Frontiers in Neuroinformatics* 4.May, pp. 1–10. ISSN: 16625196.

Jahangiri, Arman et al. (2016). "Convection-enhanced delivery in glioblastoma: a review of preclinical and clinical studies." In: *Journal of neurosurgery* 126.January, pp. 1–10. ISSN: 1933-0693.

Jamal, Asad et al. (N.D.). "Infusion mechanisms in brain white matter and its dependence of microstructure: an experimental study of hydraulic permeability". Under review in *IEEE Transaction of Biomedical Engineering*.

Jin, Byung-Ju, Alex J Smith, and Alan S Verkman (2016). "Spatial model of convective solute transport in brain extracellular space does not support a "glymphatic" mechanism". In: *The Journal of general physiology* 148.6, pp. 489–501.

Jovčevska, Ivana, Nina Kočevar, and Radovan Komel (2013). "Glioma and glioblastoma-how much do we (not) know?" In: *Molecular and Clinical Oncology* 1.6, pp. 935–941.

Jurrus, Elizabeth et al. (2010). "Detection of neuron membranes in electron microscopy images using a serial neural network architecture". In: *Medical Image Analysis* 14.6, pp. 770–783.

Kanu, Okezie O et al. (2009). "Glioblastoma multiforme: a review of therapeutic targets". In: *Expert Opinion on Therapeutic Targets* 13.6, pp. 701–718.

Karaki, Mohamad et al. (2017). "A comparative analytical, numerical and experimental analysis of the microscopic permeability of fiber bundles in composite materials". In: *Int. J. Compos. Mater* 7.3, pp. 82–102.

Kaynig, Verena, Thomas Fuchs, and Joachim M Buhmann (2010). "Neuron geometry extraction by perceptual grouping in SSTEM images". In: *IEEE Conference on Computer Vision and Pattern Recognition*. IEEE, pp. 2902–2909.

Kerr, Rex A et al. (2008). "Fast Monte Carlo simulation methods for biological reaction-diffusion systems in solution and on surfaces". In: *SIAM journal on scientific computing* 30.6, pp. 3126–3149.

Kim, Hwan Kim, Thomas H. Mareci, and Malisa Sarntinoranont (2010). "A voxelized model of direct infusion into the corpus callosum and hippocampus of the rat brain: model development and parameter analysis". In: *Med Biol Eng Comput* 27.6, pp. 41–51.

Kim, Jung Hwan et al. (2012). "Voxelized computational model for convection-enhanced delivery in the rat ventral hippocampus: Comparison with in vivo MR experimental studies". In: *Annals of Biomedical Engineering* 40.9, pp. 2043–2058. ISSN: 00906964.

Kingma, Diederik and Jimmy Ba (2014). "Adam: A method for stochastic optimization". In: *arXiv preprint arXiv:1412.6980*.

Kinney, Justin P. et al. (2013). "Extracellular sheets and tunnels modulate glutamate diffusion in hippocampal neuropil". In: *Journal of Comparative Neurology* 521.2, pp. 448–464. ISSN: 00219967.

Knott, Graham and Christel Genoud (2013). "Is EM dead?" In: *J Cell Sci* 126.20, pp. 4545–4552.

Kolyukhin, Dmitry and Magne Espedal (2010). "Numerical calculation of effective permeability by double randomization Monte Carlo method". In: *International Journal of Numerical Analysis and Modeling* 7.4, pp. 607–618. ISSN: 17055105.

KrolI, Robert A, Edward A Neuwelt, and Edward A Neuwelt (1998). "Outwitting the blood-brain barrier for therapeutic purposes: osmotic opening and other means". In: *Neurosurgery* 42.5, pp. 1083–1099.

Kroll, Robert A et al. (1996). "Increasing volume of distribution to the brain with interstitial infusion: dose, rather than convection, might be the most important factor." In: *Neurosurgery* 38.4, pp. 746–52.

Kunwar, Sandeep et al. (2010). "Phase III randomized trial of CED of IL13-PE38QQR vs Gliadel wafers for recurrent glioblastoma". In: *Neuro-oncology* 12.8, pp. 871–881.

Kuwabara, Sinzi (1959). "The forces experienced by randomly distributed parallel circular cylinders or spheres in a viscous flow at small Reynolds numbers". In: *Journal of the physical society of Japan* 14.4, pp. 527–532.

Lai, W Michael and Van C Mow (1980). "Drag-induced compression of articular cartilage during a permeation experiment". In: *Biorheology* 17.1-2, pp. 111–123.

Lam, Miu Fei, Meghan G Thomas, and Christopher RP Lind (2011). "Neurosurgical convection-enhanced delivery of treatments for Parkinson's disease". In: *Journal of Clinical Neuroscience* 18.9, pp. 1163–1167.

Lang, Gabriel and Eric Marcon (2010). "Testing randomness of spatial point patterns with the Ripley statistic". In: *ArXiv e-prints*. ISSN: 1292-8100. arXiv: `1006.1567`.

Laptev, Dmitry et al. (2012). "Anisotropic sstem image segmentation using dense correspondence across sections". In: *International Conference on Medical Image Computing and Computer-Assisted Intervention*. Springer, pp. 323–330.

Lei, Yiming et al. (2015). "The brain interstitial system: Anatomy, modeling, in vivo measurement, and applications". In: *Progress in Neurobiology*. ISSN: 18735118.

Liewald, Daniel et al. (2014). "Distribution of axon diameters in cortical white matter: an electron-microscopic study on three human brains and a macaque". In: *Biological Cybernetics* 108.5, pp. 541–557. ISSN: 14320770.

Linninger, Andreas A. et al. (2008a). "Computational methods for predicting drug transport in anisotropic and heterogeneous brain tissue". In: *Journal of Biomechanics* 41.10, pp. 2176–2187. ISSN: 00219290.

Linninger, Andreas A. et al. (2008b). "Prediction of convection-enhanced drug delivery to the human brain". In: *Journal of Theoretical Biology* 250.1, pp. 125–138. ISSN: 00225193.

Litjens, Geert et al. (2017). "A survey on deep learning in medical image analysis". In: *arXiv preprint arXiv:1702.05747*.

Liu, Ting et al. (2012). "Watershed merge tree classification for electron microscopy image segmentation". In: *IEEE International Conference on Pattern Recognition*. IEEE, pp. 133–137.

Lonser, Russell R et al. (2015). "Convection-enhanced delivery to the central nervous system". In: *Journal of neurosurgery* 122.3, pp. 697–706.

Lueshen, Eric et al. (2014). "Computer simulations and in vivo convection-enhanced delivery of fluorescent nanoparticles demonstrate variable distribution geometry". In: *Computers & chemical engineering* 71, pp. 672–676.

Marcon, Eric, Stéphane Traissac, and Gabriel Lang (2013). "A Statistical Test for Ripley's K Function Rejection of Poisson Null Hypothesis". In: *ISRN Ecology* 2013, pp. 1–9. ISSN: 2090-4622.

McGuire, Sarah, David Zaharoff, and Fan Yuan (2006). "Nonlinear dependence of hydraulic conductivity on tissue deformation during intratumoral infusion". In: *Annals of biomedical engineering* 34.7, pp. 1173–1181.

Medical Research Council (2009). *MRC research for lifelong health*. Tech. rep. Medical Research Council.

Mehta, Ankit I. et al. (2015). "Current status of intratumoral therapy for glioblastoma". In: *Journal of neuro-oncology* 125.1, pp. 1–7. ISSN: 15737373.

Meredith, M Elizabeth, Therese S Salameh, and William A Banks (2015). "Intranasal delivery of proteins and peptides in the treatment of neurodegenerative diseases". In: *The AAPS journal* 17.4, pp. 780–787.

Messaritaki, Eirini et al. (2018). "Improving the predictions of computational models of convection-enhanced drug delivery by accounting for diffusion non-Gaussianity". In: *Frontiers in neurology* 9, p. 1092.

Mestre, Humberto et al. (2020). "Cerebrospinal fluid influx drives acute ischemic tissue swelling". In: *Science* 367.6483.

Miller, Karol and Kiyoyuki Chinzei (2002). "Mechanical properties of brain tissue in tension". In: *Journal of biomechanics* 35.4, pp. 483–490.

Milosevic, Michael et al. (2008). “Interstitial permeability and elasticity in human cervix cancer”. In: *Microvascular research* 75.3, pp. 381–390.

Miranpuri, Gurwattan et al. (2013). “Convection Enhanced Delivery: A Comparison of infusion characteristics in ex vivo and in vivo non-human primate brain tissue”. In: *Annals of neurosciences* 20.3, p. 108.

Mishchenko, Yuriy (2009). “Automation of 3D reconstruction of neural tissue from large volume of conventional serial section transmission electron micrographs”. In: *Journal of Neuroscience Methods* 176.2, pp. 276–289. ISSN: 01650270.

Moccia, Sara et al. (2018). “Blood vessel segmentation algorithms–Review of methods, datasets and evaluation metrics”. In: *Computer Methods and Programs in Biomedicine* 158, pp. 71–91.

Montazeri, H. and B. Blocken (2013). “CFD simulation of wind-induced pressure coefficients on buildings with and without balconies: Validation and sensitivity analysis”. In: *Building and Environment* 60, pp. 137 –149. ISSN: 0360-1323.

More, Heather L et al. (2011). “A semi-automated method for identifying and measuring myelinated nerve fibers in scanning electron microscope images”. In: *Journal of Neuroscience Methods* 201.1, pp. 149–158.

Morrison, P F et al. (1994). “High-flow microinfusion: tissue penetration and pharmacodynamics.” In: *The American journal of physiology* 266.1 Pt 2, R292–R305. ISSN: 0002-9513.

Morrison, P F et al. (1999). “Focal delivery during direct infusion to brain: role of flow rate, catheter diameter, and tissue mechanics.” In: *The American journal of physiology* 277.4 Pt 2, R1218–R1229. ISSN: 0002-9513.

Nedanov, Pavel B. and Suresh G. Advani (2002). “Numerical computation of the fiber preform permeability tensor by the homogenization method”. In: *Polymer Composites* 23.5, pp. 758–770. ISSN: 02728397.

Netti, Paolo A et al. (2000). “Role of Extracellular Matrix Assembly in Interstitial Transport in Solid Tumors Role of Extracellular Matrix Assembly in Interstitial Transport in Solid Tumors 1”. In: *Cancer research*, pp. 2497–2503.

Nhan, Tam et al. (2014). “Modeling localized delivery of Doxorubicin to the brain following focused ultrasound enhanced blood-brain barrier permeability”. In: *Physics in Medicine & Biology* 59.20, p. 5987.

Nicholson, Charles and Sabina Hrabětová (2017). "Brain extracellular space: The final frontier of neuroscience". In: *Biophysical journal*.

Nicholson, Charles, Padideh Kamali-Zare, and Lian Tao (2011). "Brain extracellular space as a diffusion barrier". In: *Computing and Visualization in Science* 14.7, pp. 309–325. ISSN: 14329360. arXiv: `NIHMS150003`.

Nicolle, S et al. (2005). "Shear linear behavior of brain tissue over a large frequency range". In: *Biorheology* 42.3, pp. 209–223.

Nield, DA and A Bejan (2013). *Convection in Porous Media*. Springer Science & Business Media.

O'Donnel, L; Westin, CK (2011). "NIH Public Access". In: *Neurosurg Clin Am* 22.2, pp. 1–23.

Ohgaki, Hiroko and Paul Kleihues (2013). "The definition of primary and secondary glioblastoma". In: *Clinical cancer research* 19.4, pp. 764–772.

Ohgaki, Hiroko et al. (2004). "Genetic pathways to glioblastoma: a population-based study". In: *Cancer research* 64.19, pp. 6892–6899.

Ohno, Nobuhiko et al. (2007). "Extracellular space in mouse cerebellar cortex revealed by in vivo cryotechnique". In: *Journal of Comparative Neurology* 505.3, pp. 292–301. ISSN: 1096-9861.

Olesen, J. et al. (2012). "The economic cost of brain disorders in Europe". In: *European Journal of Neurology* 19.1, pp. 155–162. ISSN: 1468-1331.

Ostrom, Quinn T et al. (2014). "The epidemiology of glioma in adults: a "state of the science" review". In: *Neuro-oncology* 16.7, pp. 896–913.

Ouyang, Hui, Eric Nauman, and Riyi Shi (2013). "Contribution of cytoskeletal elements to the axonal mechanical properties". In: *Journal of biological engineering* 7.1, p. 21.

Patil, Rajesh C and AS Bhalchandra (2012). "Brain tumour extraction from MRI images using MATLAB". In: *International Journal of Electronics, Communication and Soft Computing Science & Engineering (IJECSCSE)* 2.1, p. 1.

Peate, Ian (2017). "Anatomy and physiology, 4. The brain". In: *British Journal of Healthcare Assistants* 11.11, pp. 538–541.

Philips, Alasdair et al. (2018). "Brain tumours: rise in glioblastoma multiforme incidence in England 1995–2015 suggests an adverse environmental or lifestyle factor". In: *Journal of environmental and public health* 2018.

Pieri, Valentina et al. (2019). “In vivo diffusion tensor magnetic resonance tractography of the sheep brain: an atlas of the ovine white matter fiber bundles”. In: *Frontiers in veterinary science* 6, p. 345.

Pinela, J et al. (2005). “Permeability-Porosity Relationship Assessment by 2D Numerical Simulations”. In: *Proceedings of the International Symposium On Transport Phenomena*.

Quan, Tran Minh, David GC Hildebrand, and Won-Ki Jeong (2016). “Fusionnet: A deep fully residual convolutional neural network for image segmentation in connectomics”. In: *arXiv preprint arXiv:1612.05360*.

Raghavan, Raghu and Martin Brady (2011). “Predictive models for pressure-driven fluid infusions into brain parenchyma.” In: *Physics in medicine and biology* 56.19, pp. 6179–204. ISSN: 1361-6560.

Raghavan, Raghu, Martin L Brady, and John H Sampson (2016). “Delivering therapy to target: improving the odds for successful drug development”. In: *Therapeutic delivery* 7.7, pp. 457–481.

Raghavan, Raghu and Rick M Odland (2017). “Theory of porous catheters and their applications in intraparenchymal infusions”. In: *Biomedical physics & engineering express* 3.2, p. 025008.

Raghavan, Raghu et al. (2006). “Convection-enhanced delivery of therapeutics for brain disease, and its optimization.” In: *Neurosurgical focus* 20.4, E12. ISSN: 1092-0684.

Rapoport, Stanley I (2001). “Advances in osmotic opening of the blood-brain barrier to enhance CNS chemotherapy”. In: *Expert opinion on investigational drugs* 10.10, pp. 1809–1818.

Ray, Lori, Jeffrey J Iliff, and Jeffrey J Heys (2019). “Analysis of convective and diffusive transport in the brain interstitium”. In: *Fluids and Barriers of the CNS* 16.1, p. 6.

Reina-Torres, Ester et al. (2016). “Measurement of Outflow Facility Using iPerfusion”. In: *Plos One* 11.3, e0150694.

Reynaud, Boris and Thomas M Quinn (2006). “Anisotropic hydraulic permeability in compressed articular cartilage”. In: *Journal of biomechanics* 39.1, pp. 131–137.

Ripley, B.D. (1976). “The Second-Order Analysis of Stationary Point Processes”. In: *Journal of Applied Probability* 13.2, pp. 255–266.

Rogawski, Michael A (2009). "Convection-enhanced delivery in the treatment of epilepsy". In: *Neurotherapeutics* 6.2, pp. 344–351.

Ronneberger, Olaf, Philipp Fischer, and Thomas Brox (2015). "U-net: Convolutional networks for biomedical image segmentation". In: *International Conference on Medical Image Computing and Computer-Assisted Intervention*. Springer, pp. 234–241.

Rosenbluth, Kathryn Hammond et al. (2011). "Analysis of a simulation algorithm for direct brain drug delivery". In: *NeuroImage* 59.3, pp. 2423–2429. ISSN: 10538119.

Sampson, John H et al. (2007). "Clinical utility of a patient-specific algorithm for simulating intracerebral drug infusions". In: *Neuro-oncology* 9.3, pp. 343–353.

Sarntinoranont, Malisa et al. (2006). "Computational model of interstitial transport in the spinal cord using diffusion tensor imaging". In: *Annals of Biomedical Engineering* 34.8, pp. 1304–1321. ISSN: 00906964.

Schutter, Erik De (2009). *Computational modeling methods for neuroscientists*. The MIT Press.

Sherwood, Joseph M et al. (2016). "Measurement of outflow facility using iPerfusion". In: *PLoS One* 11.3.

Smith, Joshua H. and José Jaime García (2009). "A nonlinear biphasic model of flow-controlled infusion in brain: Fluid transport and tissue deformation analyses". In: *Journal of Biomechanics* 42.13, pp. 2017–2025. ISSN: 00219290.

Smith, Joshua H. and José Jaime García (2010). "A nonlinear biphasic model of flow-controlled infusions in brain: Mass transport analyses". In: *Journal of Biomechanics* 44.3, pp. 524–531. ISSN: 00219290.

Smith, Joshua H, Kathleen A Starkweather, and José Jaime García (2011). "Implications of transvascular fluid exchange in nonlinear, biphasic analyses of flow-controlled infusion in brain". In: *Bulletin of mathematical biology* 74.4, pp. 881–907.

Stiles, Joel R, Thomas M Bartol, et al. (2001). "Monte Carlo methods for simulating realistic synaptic microphysiology using MCell". In: *Computational neuroscience: realistic modeling for experimentalists*, pp. 87–127.

Stiles, Joel R et al. (1996). "Miniature endplate current rise times less than 100 microseconds from improved dual recordings can be modeled with passive acetylcholine diffusion from a synaptic vesicle". In: *Proceedings of the National Academy of Sciences* 93.12, pp. 5747–5752.

Stine, Caleb R and Jennifer Megan Munson (2019). "Convection enhanced delivery: connection to and impact of interstitial fluid flow". In: *Frontiers in Oncology* 9, p. 966.

Støverud, Karen H. et al. (2011). "Modeling Concentration Distribution and Deformation During Convection-Enhanced Drug Delivery into Brain Tissue". In: *Transport in Porous Media* 92.1, pp. 119–143. ISSN: 01693913.

Stupp, Roger et al. (2009). "Effects of radiotherapy with concomitant and adjuvant temozolomide versus radiotherapy alone on survival in glioblastoma in a randomised phase III study: 5-year analysis of the EORTC-NCIC trial". In: *The lancet oncology* 10.5, pp. 459–466.

Swabb, E A, J Wei, and P M Gullino (1974). "Diffusion and convection in normal and neoplastic tissues." In: *Cancer research* 34.10, pp. 2814–22. ISSN: 0008-5472.

Syková, Eva and Charles Nicholson (2008). "Diffusion in brain extracellular space." In: *Physiological reviews* 88.4, pp. 1277–1340. ISSN: 0031-9333.

Takano, Naoki et al. (2002). "Microstructure-based evaluation of the influence of woven architecture on permeability by asymptotic homogenization theory". In: *Composites Science and Technology* 62.10-11, pp. 1347–1356. ISSN: 02663538.

Tamayol, A and M Bahrami (2009). "Analytical determination of viscous permeability of fibrous porous media". In: *International Journal of Heat and Mass Transfer* 52.9-10, pp. 2407–2414.

Tao, A, L Tao, and C Nicholson (2005). "Cell cavities increase tortuosity in brain extracellular space". In: *Journal of Theoretical Biology* 234.4, pp. 525–536.

Tao, L. and C. Nicholson (2004). "Maximum geometrical hindrance to diffusion in brain extracellular space surrounding uniformly spaced convex cells". In: *Journal of Theoretical Biology* 229.1, pp. 59–68. ISSN: 00225193.

Tavner, ACR et al. (2016). "On the appropriateness of modelling brain parenchyma as a biphasic continuum". In: *Journal of the mechanical behavior of biomedical materials* 61, pp. 511–518.

Thakkar, Jigisha P et al. (2014). "Epidemiologic and molecular prognostic review of glioblastoma". In: *Cancer Epidemiology and Prevention Biomarkers* 23.10, pp. 1985–1996.

Titze, Benjamin and Christel Genoud (2016). "Volume scanning electron microscopy for imaging biological ultrastructure". In: *Biology of the Cell* 108, pp. 307–323.

Todd, Nick et al. (2019). "The neurovascular response is attenuated by focused ultrasound-mediated disruption of the blood-brain barrier". In: *NeuroImage* 201, p. 116010.

Truscello, S. et al. (2012). "Prediction of permeability of regular scaffolds for skeletal tissue engineering: A combined computational and experimental study". In: *Acta Biomaterialia* 8.4, pp. 1648–1658. ISSN: 17427061.

Tschopp, Fabian et al. (2016). "Efficient convolutional neural networks for pixelwise classification on heterogeneous hardware systems". In: *IEEE International Symposium on Biomedical Imaging*. IEEE, pp. 1225–1228.

Turaga, Srinivas C et al. (2010). "Convolutional networks can learn to generate affinity graphs for image segmentation". In: *Neural Computation* 22.2, pp. 511–538.

Türkkan, Gökçen ERYILMAZ and Serdar Korkmaz (2015). "Determination of Hydraulic Conductivity Using Analytical and Numerical Methods Applied to Well and Aquifer Tests". In: *Teknik Dergi* 26.1, pp. 6969–6992.

Vandamme, Matthieu et al. (2017). *Poromechanics VI: Proceedings of the Sixth Biot Conference on Poromechanics*.

Varenika, Vanja et al. (2008). "Detection of infusate leakage in the brain using real-time imaging of convection-enhanced delivery". In: *Journal of Neurosurgery* 109.5, pp. 874–880.

Vargová, Lỳdia and Eva Syková (2008). "Extracellular space diffusion and extrasynaptic transmission". In: *Physiol Res* 57.Suppl 3, S89–S99.

Vargová, Lỳdia et al. (2003). "Diffusion parameters of the extracellular space in human gliomas". In: *Glia* 42.1, pp. 77–88.

Vendel, Esmée, Vivi Rottschäfer, and Elizabeth CM de Lange (2019). "The need for mathematical modelling of spatial drug distribution within the brain". In: *Fluids and Barriers of the CNS* 16.1, p. 12.

Vidotto, Marco, Elena De Momi, and Daniele Dini (N.D.). "White matter microstructure role for hydraulic permeability: a new electron microscopy images based approach". To be submitted to *Proceedings of the National Academy of Sciences*.

Vidotto, Marco, Daniele Dini, and Elena De Momi (2018). "Effective diffusion and tortuosity in brain white matter". In: *2018 40th Annual International Conference of the IEEE Engineering in Medicine and Biology Society (EMBC)*. IEEE, pp. 4901–4904.

Vidotto, Marco et al. (2018). "White matter hydraulic permeability from electron microscopy images". In: *8th World Congress of Biomechanics, July 8 - 12, 2018, Dublin, Ireland*.

Vidotto, Marco et al. (2019a). "A computational fluid dynamics approach to determine white matter permeability". In: *Biomechanics and modeling in mechanobiology*, pp. 1–12.

Vidotto, Marco et al. (2019b). "FCNN-based axon segmentation for convection-enhanced delivery optimization". In: *International journal of computer assisted radiology and surgery* 14.3, pp. 493–499.

Vidotto, Marco et al. (N.D.). "Advanced imaging methods to improve the predictive capabilities of CED models". Under second review in *Annals of Biomedical Engineering*.

Vogelbaum, Michael A and Manish K Aghi (2015). "Convection-enhanced delivery for the treatment of glioblastoma". In: *Neuro-oncology* 17.suppl_2, pp. ii3–ii8.

Vunjak-Novakovic, G et al. (1999). "Bioreactor cultivation conditions modulate the composition and mechanical properties of tissue-engineered cartilage". In: *Journal of Orthopaedic Research* 17.1, pp. 130–138.

Walhovd, Kristine B, Heidi Johansen-Berg, and Ragnhildur Thora Karadottir (2014). "Unraveling the secrets of white matter–bridging the gap between cellular, animal and human imaging studies". In: *Neuroscience* 276, pp. 2–13.

Weidle, Ulrich H, Jens Niewöhner, and Georg Tiefenthaler (2015). "The blood–brain barrier challenge for the treatment of brain cancer, secondary brain metastases, and neurological diseases". In: *Cancer Genomics-Proteomics* 12.4, pp. 167–177.

Weiser, Jennifer R and W Mark Saltzman (2014). "Controlled release for local delivery of drugs: barriers and models". In: *Journal of Controlled Release* 190, pp. 664–673.

Wells, Rebecca G (2008). "The role of matrix stiffness in regulating cell behavior". In: *Hepatology* 47.4, pp. 1394–1400.

Westphal, M et al. (2006). "Gliadel® wafer in initial surgery for malignant glioma: long-term follow-up of a multicenter controlled trial". In: *Acta neurochirurgica* 148.3, pp. 269–275.

White, Edward et al. (2011). "An evaluation of the relationships between catheter design and tissue mechanics in achieving high-flow convection-enhanced delivery". In: *Journal of Neuroscience Methods* 199.1, pp. 87–97.

Williams, Tom et al. (2014). "Is robot telepathy acceptable? Investigating effects of nonverbal robot-robot communication on human-robot interaction". In: *Robot and Human Interactive Communication, 2014 RO-MAN: The 23rd IEEE International Symposium on*. IEEE, pp. 886–891.

Winklewski, Pawel J et al. (2018). "Understanding the physiopathology behind axial and radial diffusivity changes—what do we know?" In: *Frontiers in neurology* 9, p. 92.

Xiao, Chi et al. (2018). "Deep contextual residual network for electron microscopy image segmentation in connectomics". In: *International Symposium on Biomedical Imaging*. IEEE, pp. 378–381.

Xu, Peng and Boming Yu (2008). "Developing a new form of permeability and Kozeny-Carman constant for homogeneous porous media by means of fractal geometry". In: *Advances in Water Resources* 31.1, pp. 74–81. ISSN: 03091708.

Yang, Xiaohu, Tian Jian Lu, and Tongbeum Kim (2014). "An analytical model for permeability of isotropic porous media". In: *Physics Letters, Section A: General, Atomic and Solid State Physics* 378.30-31, pp. 2308–2311. ISSN: 03759601.

Yazdchi, K., S. Srivastava, and S. Luding (2011). "Microstructural effects on the permeability of periodic fibrous porous media". In: *International Journal of Multiphase Flow* 37.8, pp. 956–966. ISSN: 03019322.

Yuan, Fan (1998). "Transvascular drug delivery in solid tumors". In: *Seminars in radiation oncology*. Vol. 8. 3. Elsevier, pp. 164–175.

Zaimi, Aldo et al. (2018). "AxonDeepSeg: automatic axon and myelin segmentation from microscopy data using convolutional neural networks". In: *Scientific reports* 8.1, p. 3816.

Zeng, Xuesen et al. (2015). "Numerical prediction of in-plane permeability for multilayer woven fabrics with manufacture-induced deformation". In: *Composites Part A: Applied Science and Manufacturing* 77, pp. 266–274. ISSN: 1359835X.

Zhan, Wenbo, Moath Alamer, and Xiao Yun Xu (2018). "Computational modelling of drug delivery to solid tumour: Understanding the interplay between chemotherapeutics and biological system for optimised delivery systems". In: *Advanced drug delivery reviews* 132, pp. 81–103.

Zhan, Wenbo, Ferdinando Rodriguez y Baena, and Daniele Dini (2019). "Effect of tissue permeability and drug diffusion anisotropy on convection-enhanced delivery". In: *Drug delivery* 26.1, pp. 773–781.

Zhan, Wenbo and Chi-Hwa Wang (2018). "Convection enhanced delivery of chemotherapeutic drugs into brain tumour". In: *Journal of Controlled Release* 271, pp. 74–87.

Zhan, Wenbo et al. (2017). "Mathematical modelling of convection enhanced delivery of carmustine and paclitaxel for brain tumour therapy". In: *Pharmaceutical research* 34.4, pp. 860–873.

Zhang, Hui et al. (2012). "NODDI: Practical in vivo neurite orientation dispersion and density imaging of the human brain". In: *NeuroImage* 61.4, pp. 1000–1016. ISSN: 10538119.

Zhang, Lujun, Mingqiang Yang, and Mingyan Jiang (2012). "Mathematical modeling for convection-enhanced drug delivery". In: *Procedia Engineering* 29, pp. 268–274. ISSN: 18777058.

Zhang, Xiao-Yu et al. (2000). "Interstitial hydraulic conductivity in a fibrosarcoma". In: *American Journal of Physiology-Heart and Circulatory Physiology* 279.6, H2726–H2734.

List of Publications on International Peer-Reviewed Journals

Jamal, Asad et al. (N.D.). "Infusion mechanisms in brain white matter and its dependence of microstructure: an experimental study of hydraulic permeability". Under review in *IEEE Transaction of Biomedical Engineering*.

Vidotto, Marco, Elena De Momi, and Daniele Dini (N.D.). "White matter microstructure role for hydraulic permeability: a new electron microscopy images based approach". To be submitted to *Proceedings of the National Academy of Sciences*.

Vidotto, Marco et al. (2019a). "A computational fluid dynamics approach to determine white matter permeability". In: *Biomechanics and modeling in mechanobiology*, pp. 1–12.

Vidotto, Marco et al. (2019b). "FCNN-based axon segmentation for convection-enhanced delivery optimization". In: *International journal of computer assisted radiology and surgery* 14.3, pp. 493–499.

Vidotto, Marco et al. (N.D.). "Advanced imaging methods to improve the predictive capabilities of CED models". Under second review in *Annals of Biomedical Engineering*.

List of Publications on Conference Proceedings

Vidotto, Marco, Daniele Dini, and Elena De Momi (2018). "Effective diffusion and tortuosity in brain white matter". In: *2018 40th Annual International Conference of the IEEE Engineering in Medicine and Biology Society (EMBC)*. IEEE, pp. 4901–4904.

Vidotto, Marco et al. (2018). "White matter hydraulic permeability from electron microscopy images". In: *8th World Congress of Biomechanics, July 8 - 12, 2018, Dublin, Ireland*.

Vidotto, Marco et al. (2019). "Axonal undulation role for tortuosity in white matter". In: *25th Congress of the European Society of Biomechanics, July 7 - 10, 2019, Vienna, Austria*.